ABSTRACT

Title of Thesis: A COMPARATIVE FRAMEWORK FOR MANEUVERABILITY AND GUST TOLERANCE OF AERIAL MICROSYSTEMS

Renee Campbell, Masters of Science, 2012

Dissertation directed by: Professor J. Sean Humbert
Department of Aerospace Engineering

Aerial microsystems have the potential of navigating low-altitude, cluttered environments such as urban corridors and building interiors. Reliable systems require both agility and tolerance to gusts. While many platform designs are under development, no framework currently exists to quantitatively assess these inherent bare airframe characteristics which are independent of closed loop controllers. This research develops a method to quantify the maneuverability and gust tolerance of vehicles using reachability and disturbance sensitivity sets. The method is applied to a stable flybar helicopter and an unstable flybarless helicopter, whose state space models were formed through system identification. Model-based static $\mathcal{H}_\infty$ controllers were also implemented on the vehicles and tested in the lab using fan-generated gusts. It is shown that the flybar restricts the bare airframe's ability to maneuver in translational velocity directions. As such, the flybarless helicopter proved more maneuverable and gust tolerant than the flybar helicopter. This approach was specifically applied here to compare stable and unstable helicopter platforms; however, the framework may be used to assess a broad range of aerial microsystems.

A COMPARATIVE FRAMEWORK FOR MANEUVERABILITY AND GUST TOLERANCE OF AERIAL MICROSYSTEMS

by

Renee Campbell

Thesis submitted to the Faculty of the Graduate School of the
University of Maryland, College Park in partial fulfillment
of the requirements for the degree of
Masters of Science
2012

Advisory Committee:
Professor J. Sean Humbert, Chair/Advisor
Professor Roberto Celi
Professor Robert M. Sanner

Acknowledgments

First, I owe my gratitude to Dr. Sean Humbert. Thank you for the engaging research problems, the mentorship, the excellent courses, and the resources to make my education possible. I am also grateful to Dr. Robert Sanner for the challenging and enlightening controls courses. I'd also like to acknowledge Dr. Sarah Harris from my undergraduate years for serving as an all-around mentor and role model.

I am immensely thankful for my family's support: To my father, who gave me daily math lessons as a girl; to my mother, for her example of hard work and persistence; to both parents, for the financial sacrifices they made to ensure I had a strong educational foundation and also for their spiritual example; to Jens, for his patience and companionship; and to my three older brothers (and the Seattle rain) for making sure I turned out tough.

I'd like to acknowledge the following colleagues who provided input and advice for this research: Vikram and Imraan for imparting helicopter dynamics intuition; Greg for aiding with Vicon and Labview development; Badri for helping sort out mote timer idiosyncrasies and helping with pre-review soldering marathons; Jared for sys id tips; and the legendary Joe for getting me started on hardware.

The AVL is comprised of deep thinkers and hard workers, comedians and athletes, unique personalities and very good friends—an all-around top-notch crew. The combination of collaboration and comradery is what makes the daily research grind engaging and progressive. Joe, Imraan, Greg, Badri, Mac, Nick, Doug, Lina, Hector: I can't imagine better company! *Coram Deo.*

Table of Contents

List of Tables

List of Figures

Nomenclature

$[a\ b]$	Flapping angles with respect to the hub plane
A	State space dynamics matrix
A_k	Amplitude of multisine signal (ch 3)
β	General flapping angle
$[\hat{b}_x\ \hat{b}_y\ \hat{b}_z]$	Body axis $\mathcal{B}$
B	State space control input matrix
c	Cosine
$[c\ d]$	Flybar angle with respect to the hub plane
C	State space output matrix
$C_{l\alpha}$	Airfoil lift curve slope
C_R, C_F	Flybar damping coefficients, rotating and fixed frames
$\delta_{[\cdot]}$	Control input
Δ	Perturbation
$\vec{d}$	Disturbances
D	State space control feed-through matrix (ch 1); Gust matrix (ch 6)
D_g	Gust matrix (ch 5)
$[\hat{e}_x\ \hat{e}_y\ \hat{e}_z]$	Inertial axis $\mathcal{G}$
$\mathcal{E}_c$	Reachability ellipsoid
$\mathcal{E}_d$	Disturbance sensitivity ellipsoid
$\vec{e}$	Control error
$\vec{f}$	Generic ODE
$\vec{F}$	Force vector
γ	Lock number (ch 2)
γ	$\mathcal{H}_\infty$ bound (ch 6)
g	Gravity, 9.81 m/s
G	System transfer function
I	Identity matrix
$I_{[\cdot]}$	Body axis inertia
κ_β	Flapping spring
K	Gain matrix
K_{sb}	Flybar inertia scaling factor
λ	Eigenvalues of A
$[L\ M\ N]$	Moments in body frame
M	Coprime factor (ch 5); Subspace basis vectors (ch 5)
$\vec{M}$	Moment vector
ν	Process noise
N	Coprime factor (ch 5)
Ω	Rotor rate
Ψ_c	Controllability operator

$[p\ q\ r]$	Body angular rates $\vec{\omega}^B$ in $\mathcal{B}$ coordinates
$[\phi\ \theta\ \psi]$	Euler angles
ϕ_k	Phase shift of multisine signal
π	Pi, 3.1416
P	Solution to Ricatti equation
Q	State weighting matrix for $\mathcal{H}_\infty$ gain selection
Ψ	Position of rotor in plane
ρ	density of air
ρ	Scale factor for disturbance sensitivity ellipsoids (ch 6)
$\vec{r}$	Reference input
R	Rotor radius
R	Covariance matrix
R	Input weighting matrix for $\mathcal{H}_\infty$ gain selection
R_{BG}	Transformation matrix from $\mathcal{G}$ to $\mathcal{B}$
s	Sine
σ	Singular values
$S(s)$	Sensitivity transfer function
τ_f	Flapping time constant
τ_{sb}	Stabilizer bar time constant
$\hat{\theta}$	Parameter estimates
Θ	Blade pitch angle
T	Thrust
$T(s)$	Tracking transfer function
$[u\ v\ w]$	Body velocities $\vec{v}_B$ in $\mathcal{B}$
v	Residuals
$\vec{u}$	System input
W	Vehicle weight
$\vec{x}$	System states
$[\dot{x}\ \dot{y}\ \dot{z}]$	Velocity states in $\mathcal{G}$
$[X\ Y\ Z]$	Forces in body frame
X_c, $\bar{X}_c$	Controllability gramian, Scaled gramian
X_d, $\bar{X}_d$	Disturbance sensitivity gramian, Scaled gramian
$\vec{y}$	System outputs
$\vec{y}_d$	System desired outputs

List of Abbreviations

CFD	Computation Fluid Dynamics
CG	Center of Gravity
CIFER	Comprehensive Identification from FrEquency Responses
CRB	Cramer Rao Lower Bound
DOF	Degrees of Freedom
FB	Flybar
GINA	Guidance and Inertial Navigation Assistant
GPS	Global Positioning System
IMU	Inertial Measurement Unit
LQR	Linear Quadratic Regulator
LQG	Linear Quadratic Gaussian
MAV	Micro Air Vehicle
MIMO	Multi Input Multi Output
NASA	National Aeronautics and Space Administration
NRMSE	Normalized Root Mean Square Error
ODE	Ordinary Differential Equation
PID	Proportional Integral Derivative
PWM	Pulse-Width Modulation
RC	Remote Control
RGA	Relative Gain Array
RHP	Right Hand Plane
SEP	Spherical Error Probable
SIDPAC	System Identification Programs for AirCraft
SISO	Single Input Single Output
SV	Singular Value
TPP	Tip Path Plane
UAV	Unmanned Air Vehicles
wFB	With Flybar

Chapter 1

Introduction

1.1 Motivation and Challenges

Over the past decade, autonomous vehicles have become reliable and sophisticated enough to deploy in military, industrial, and research settings. In military applications, ground-based wheeled robots are used for security, reconnaissance, and even explosives detection and disposal. Designs for fixed-wing Unmanned Air Vehicles (UAVs) are now compact enough to be launched by soldiers and deployed for high-altitude surveillance. Industrial applications also deploy autonomous robots in factories and warehouse distribution centers. For research purposes, Mars rovers are a fascinating example of how autonomous vehicles can be used to explore environments otherwise too hostile for humans.

But so far, the vehicles that are currently implemented have fundamental mobility limitations. As such, Micro Air Vehicles (MAVs) have become an increasingly popular area of research. MAVs have the potential for navigating low-altitude settings like urban street corridors, building interiors, and complex geographical features like caves. Unlike wheeled robots, they are not limited by obstacles on the ground. Furthermore, flapping winged and rotor configurations provide maneuverability advantages over fixed-wing UAVs. In addition to the applications already covered by UAVs and ground-based robots, MAVs can be used for search-and-rescue

operations, infrastructure inspection, wildlife tracking, and even film-making.

In order to perform reliably in any of these applications, a good MAV design needs to be both agile and resistant to gusty conditions. Even common indoor features such as fans, open windows, or air conditioning units can prove challenging to an MAV tracking a trajectory or station keeping. Many MAV designs are currently under development, including quadrotors, cyclcopters, ducted fans, and several helicopter configurations. The objective of this thesis is to develop a framework for comparing the maneuverability and gust tolerance characteristics inherent to a vehicle's bare airframe. A stable flybar helicopter and unstable flybarless helicopter are used to demonstrate the methods; however, the framework can be applied to assess the potential performance of many vehicle platforms.

1.2 Related Work

Limited work has been performed in the area of evaluating maneuverability and the effects of gust disturbances on MAVs. A study performed by Costello and Zarovy tested the ability of coaxial helicopters to maintain a position and track a trajectory in the presence of fan gusts [1]. The findings were quantified with the Spherical Error Probable (SEP). However, the study does not identify the properties of the vehicle that determine its inherent potential to perform in gusts. Additionally the performance metric was dependent on the spectral content and intensity of the experimental gusts.

Inherent maneuverability of fruit flies (*Drosophila melanogaster*) was assessed

by Faruque, who used reachability gramians to determine inputs that minimize the energy required to control the system [2]. This work was developed further by Szczublewski, who evaluated the gust tolerance of a close loop micro-quadrotor by extending the concept of reachability ellipsoids to disturbances [3]. While an unstable platform like a micro-quadrotor will inevitably require inner loop stabilization, the performance can be greatly influenced by the control designer. As such, evaluating the bare airframe of a vehicle is critical for understanding its potential. However, the familiar form for finding controllability gramians is limited to stable systems, and MAVs, due to their low mass and inertia, are often unstable. Zhou provides a method for calculating the gramians of unstable systems, which can be applied to this analysis [4].

In order to employ the theoretical framework presented here, linear state space models of the helicopters were required. System identification of full-scale helicopters was pioneered in the seventies by Molusis [5], who specifically noted the importance of rotor-fuselage coupling and the need for including higher order rotor dynamics in the model [6]. These early attempts at helicopter modeling used time domain output error methods. In the late eighties, frequency domain techniques were applied to helicopters and presented many advantages [7]. The broad range of frequencies exhibited in the helicopter dynamics include structural vibration caused by shafts, rotors and the powerplant; high-frequency rotor dynamics; and the fuselage dynamics. In frequency domain analysis, the specific range of frequencies relevant to a particular parameter can be specified. This field was pioneered by Tischler and Cauffman with the identification of the BO-105 helicopter [8] using the frequency

domain software CIFER.

Frequency domain analysis has subsequently been applied to identifying models for small-scale rotorcraft. Mettler used these methods to identify the dynamics the R50 helicopter, with 150 cm rotor radius and 44 kg dry weight [9], as well as the X-Cell .60 helicopter, which has a 4.5 kg dry weight [10]. Conroy then extended the techniques to the E-Sky Honeybee helicopter, with a 25.3-cm main rotor radius and 288 gram weight with sensors [11]. However, limited work has been preformed in developing models for unstable vehicles on the MAV scale. The time domain technique output error has been used to identify the dynamics of a 70 g micro-quadrotor [12]. The helicopters used in this work work weigh approximately 60 g.

1.3 Research Contributions

This research includes the following contributions to the field of aerial microsystems system identification, dynamics, and control:

- A framework for using reachability and disturbance sensitivity sets to assess the bare airframe characteristics of aerial microsystems.
- A method for performing system identification on a vehicle with highly-coupled dynamics and few known parameters.
- State space models for a flybar micro-helicopter and a flybarless micro-helicopter.
- An assessment of the influence of a Bell flybar on the dynamics, agility, and gust tolerance of a micro-helicopter.

- Static $\mathcal{H}_\infty$ controllers for micro-helicopters designed for station keeping in gusty conditions.

1.4 Overview

The following section gives an overview of the topics covered in each chapter.

Chapter 2: The basis for any vehicle development is understanding its physical dynamics and representing the dynamics with a model. A model gives insight into the inherent properties of the vehicle, as well as provides a mathematical basis for developing a controller. This chapter uses vehicle kinematics and dynamics to develop a linear, state space model structure for the helicopters. Rotor dynamics and flybar dynamics are also incorporated into the model.

Chapter 3: System identification is the method of numerically determining the linear coefficients of the model structure for the system. This chapter gives an overview of the options for system identification, as well as the challenges involved in performing system identification on micro-helicopters. The process used for identifying the models for the flybar and flybarless helicopters is presented, as well as the resulting linear models.

Chapter 4: We then look at the vehicles' dynamic characteristics by examining the modes of the system through the pole-zero diagrams and eigenvector plots. The influence of the flybar on vehicle dynamics, as revealed through

the modes of the system, is discussed. However, at this point, the effects of the flybar on the vehicle's ability to maneuver in gusts is still unclear.

Chapter 5: This chapter presents a method for comparing maneuverability and gust tolerance properties by looking at the reachability and disturbance sensitivity sets of their respective models. For linear models, these sets are defined by ellipsoids. By examining the length and direction of the principle axes of these ellipsoids, we can draw conclusions about the bare airframe's inherent characteristics.

Chapter 6: An H_∞ controller is especially suited for rejecting gust disturbances and optimizing the energy requirements of the actuators. An inner loop controller is designed for vehicle stabilization, and an outer loop controller is designed for station keeping. Using robust analysis tools, the tracking and disturbance sensitivity bandwidths of the vehicles are analyzed. The static H_∞ gains are implemented on the flybar and flybarless helicopters, and the ability of the two vehicles to hold a position in the presence of a gust is tested in the lab.

Chapter 7: The methods and findings of the research are discussed, as well as the future work required to continue developing and implementing MAV designs.

1.4.1 Scope

There are two major limitations to the scope of this project. First, only the rigid body dynamics directly coupled to the cyclic inputs of the vehicle are considered. This includes the attitude states ϕ and θ, the rotational rate states p and q, and the translational velocity states u and v. The interactions between these states are complex and, by themselves, provide for an interesting study of gust tolerance and maneuverability. The model for heave and yaw states (ψ, r, w) are assumed to be decoupled from these states. The height and heading of the vehicle is controlled via PID gains for all data collection and tests presented in the thesis. The second limitation is that all control is implemented off-board using Vicon. The helicopters have the sensing and processing capability of implementing on-board control; however, this step is deferred for future work.

1.5 Helicopter Platforms

A helicopter platform was selected for this research for several reasons. Compared to fixed-wing platforms, helicopters are inherently very maneuverable—they have the ability to ascend and descend vertically; to hover; and to fly in forward, backward or sideways directions. Unlike flapping wing platforms, which are still in a development phase, Remote Control (RC) model helicopters have been commercially available for three decades, and their designs are easily adapted for research settings. Compared to other rotary-wing platforms currently being researched, including meso- and micro-scale cyclocopters and quadrotors, helicopters have compa-

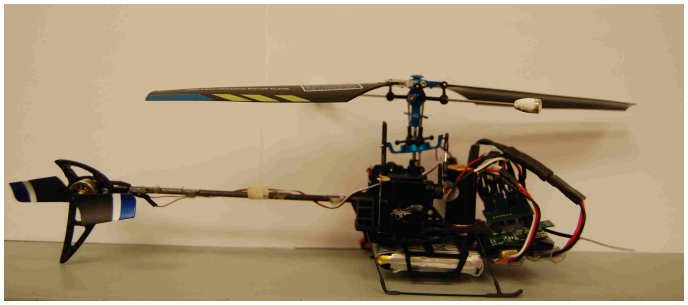

(a) Flybar helicopter.

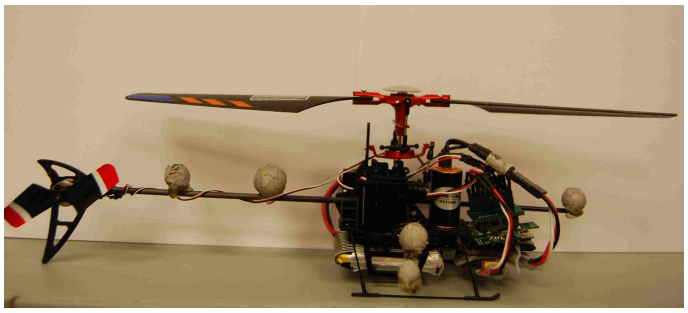

(b) Flybarless helicopter.

Figure 1.1: A flybar helicopter and flybarless helicopter were the chosen platforms for this research. Each helicopter weighs ≈66 g with their on-board battery and have a rotor radius of 11 cm.

rable maneuverability with the added advantage of a simpler design concept. Both a helicopter stabilized with a flybar and a helicopter stabilized solely with a controller (flybarless) helicopter are used. The helicopters are pictured in Fig. 1.1.

1.5.1 Physical Description

For the flybar platform, the Walkera model CB100 was selected, and for the flybarless platform, a Walker V100D01 was selected. Besides the addition of the flybar, the two platforms are nearly identical. The helicopters weigh approximately 66 g with a battery and have 11 cm rotor radius. A SolidWorks of the basic airframe

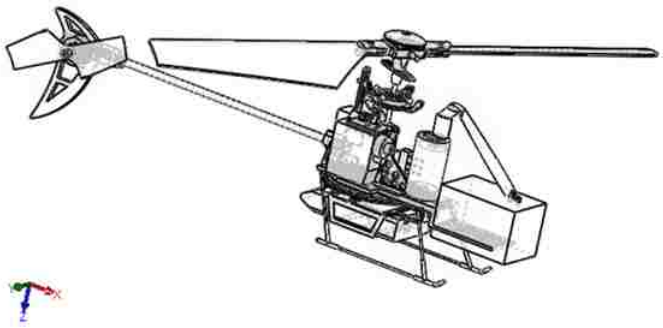

Figure 1.2: A SolidWorks model was used to calculate the moments of inertia of the helicopters. (CAD credit: Julia Ashkanazy)

Physical Parameters	
Mass and Inertia Properties	$I_{xx} = 11.24$ g-cm^{-2} $I_{yy} = 35.82$ g-cm^{-2} $I_{zz} = 33.71$ g-cm^{-2} $m = 66$ g with battery c.g. = behind main motor, close to base.
Rotor Dimensions	$R_{main} = 11$ cm $c_{main} = 1.9$ cm $R_{tail} = 2.4$ cm $c_{tail} = 0.75$ cm
Hover Rotor Rates	$\Omega_{main} = 3,100$ rpm $\Omega_{tail} = 14,000$ rpm

Table 1.1: Helicopter Physical Parameters

was used to determine the helicopters' inertial properties. The physical properties of the vehicle are presented in Table 1.1 and the SolidWorks model is shown in Fig. 1.2.

The flybar on the flybar helicopter acts as a physical stability augmentation device. Flybars have traditionally been used to stabilize small helicopters, especially

Figure 1.3: Flybars are used to mechanically stabilize helicopters.

before on-board electronic controllers were widely used. With the flybar, the micro-helicopter used for this research is stable enough to fly open loop. Without the flybar, a controller is required to keep the helicopter stable. The flybar consists of a rod positioned at an approximately 45° angle to the rotors and has a 1-g weight secured on each end. The mechanics of the flybar are further discussed in Chapter 2 and analysis of the flybar helicopter compared to the flybarless helicopter is presented throughout the thesis. A close-up of the flybar mechanism is shown in Fig. 1.3.

1.5.2 Control Inputs

The helicopters have four control inputs. One input controls the main motor speed, which in turn adjusts the main rotor rate and the resulting thrust magnitude. Likewise, the tail rotor thrust is adjusted by an input dictating the speed of the tail rotor motor. Two inputs control servos that adjust the pitch of the rotor blades, which in term tilts the thrust vector to induce a forward, backward, or sideways motion. This mechanism is explored in detail in Section 2.4.1.

It is important to note here that helicopters, full-scale or model-sized, generally adjust thrust magnitude through collective pitching of the rotor blades. The motor rate—and thus the rotation rate of the rotors—is then kept constant. At the time of this research, collective pitch control was not available in this model size. For future work, the recently released Walkera Genius model with collective pitch should be used. Collective pitch quickens the response of the helicopter and eliminates non-linearities associated with the motor dynamics.

1.5.3 On-Board Sensing and Processing

The Walkera helicopter models come with a shelf electronics package which includes gyroscopes, accelerometers and a processor with a pre-implemented controller. The pilot can adjust the gains of the controller by tuning knobs on the package.

To implement custom control on the helicopters, the shelf electronics were replaced with a custom avionics package developed by the University of California, Berkeley. The Guidance and Inertial Navigation Assistant (GINA) mote is equipped with a Texas Instruments MSP430F2618 16-bit microcontroller. The board also has two Kionix KXSD9-1026 accelerometers, which measure the attitude of the vehicle with respect to the gravity vector, and a InvenSenseTM ITG3200 gyroscope, which measures pitch, roll, and yaw rates. The board's communication protocol is a 2.4 GHz Atmel AT86RF230 radio which is capable of both sending and receiving data. The basestation for communicating with the Mote from a control station is a USB

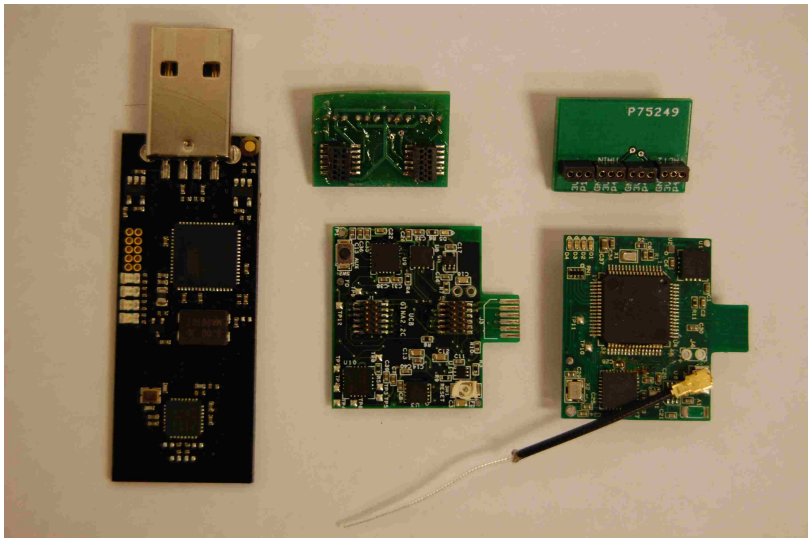

Figure 1.4: The GINA Mote, designed by University of California, Berkeley, was used to receive commands from the ground station and control input signals.

Atmel RZ600. A custom breakout board was designed to interface the Mote with the helicopter servos and actuators. The mote and breakout board are pictured in Fig. 1.4. For the purpose of this research, all attitude and rate measurements were performed off-board with the Vicon system, described in Section 1.6.2. However, in the future, the mote's accelerometers and gyroscopes can be used for this task, and the entire control can be implemented on-board.

In order to interface the mote with the helicopter, the signals of the shelf

Figure 1.5: The PWM signal for each control input is listed in Table **??**.

Control	Period T (ms)	Pulse Width t_0(ms)	Duty Cycle (%)
Lateral and Longitudinal Servo Input			
Servo extends up	17.0	1.25	7.35
Servo neutral	17.0	1.5	8.82
Servo extends down	17.0	1.75	10.3
Main Motor Input			
Full speed	17.0	0.9	11.8
Off	17.0	2.0	5.3
Tail Motor Input			
Full speed	0.500	0.0005	0.1
Off	0.500	0.4550	91

Table 1.2: PWM Signals for Servos and Motor Controllers

electronics had to be tested and replicated. All actuators, which include the longitudinal and lateral servos and the motors' speed controllers, are controlled with pulse-width modulation (PWM) from the processor. The PWM period and duty cycle for each control is listed in Table 1.2 and illustrated in Fig. **??**. The mote firmware was programmed to replicate these signals. Because the signal period for the tail motor speed controller was a different length than the other controls, two timers on the microcontroller were designated to the PWM signals. (For other lab vehicles, just one timer is designated to the PWMs.) Timer A was designated for signals requiring a 17 ms period length and Timer B was designated for the 500 μs period length. It should be noted that Timer B is also used to control the loop timing—if future modifications are made to the firmware, the designation of these timers should be considered carefully.

1.6 Laboratory Equipment

A set of Saitek joysticks were used to pilot the helicopter. The joysticks interfaced with a program and user interface developed in Labview, which communicated the signals to the mote on the helicopter. The Labview program has several other functions, including automatic signal generation, state feedback, and data recording. A Vicon camera system tracked the position and orientation of the vehicle for the system identification data collection and model-based control implementation. More detail on the program and equipment is provided in the following sections.

1.6.1 Labview Program

The Labview program, developed in version 8.6, has the following functionalities:

- **Mote Initialization** Before any control commands are sent to the mote, Labview initializes the communication. Initialization settings for the mote—which include onboard feedback gains, filter thresholds, and the type of communciation (uni- or bi-directional)—are also communicated at this point. Note, these mote settings cannot be changed without restarting the program.

- **Joystick Control** The absolute nominal functionality of the program is to read joystick commands and communicate them to the mote. The basic commands include the main motor speed, tail rotor speed, and the cyclic inputs. Additionally, several knobs on the joystick can be used to activate different

types of control schemes or automated inputs. Manual commands can also be communicated to the mote using slide-bars on the user interface.

- **Automatic Signal Generation** Several options for automated signals include impulse, step, chirp, and multisinusoidal inputs. The signals can be generated while the pilot is holding the helicopter in the desired trim condition, which is generally hover.

- **Filtering** Any data collected by the Labview program (i.e., from Vicon) can be conditioned in real-time with a low-pass filter. This is especially useful when noisier measurements, like yaw rates, are used for feedback.

- **Feedback Gains** Several types of control schemes are included in the Labview program. These include heading lock (ensuring the helicopter is always facing forward), height control (maintaining a commanded altitude), and position control (maintaining a commanded position). The heading lock and height control gains, both of which were determined through empirical PID gain tuning, were kept fixed for all experiments presented in this thesis. However, the position control gains - which include both outer-loop and inner-loop feedback - are where the control designs presented in Chapter 6 are realized.

- **Uni- or Bi-Directional Communication with Mote** The mote is capable of both sending and receiving data. Since all experiments performed for this thesis used Vicon measurements, not on-board sensing, receiving mote data was not necessary. However, for future work, data such as time stamps, control

commands, and accelerometer and gyroscope measurements can be recorded. At this point, implementing bi-directonal communication presents significant time-delays in the mote processing.

- **Vicon Data Interpretation** Vicon tracks the position and orientation of the vehicle. The Labview program differentiates this data to determine vehicle translational and rotational rates and performs transforms to convert the data between the inertial and body frames.

- **State Visualization** The user interface includes several real-time plots to visualize the body orientation and rates of the vehicle, as well as its position in the room.

- **Data Recording** Any data collected by Vicon—including timestamps, the control inputs to the mote, data communicated from the mote (using bi-directional communication), and Vicon data—can be recorded in a text file.

1.6.2 Vicon Cameras

The Vicon motion caption system is a set of eight cameras that track retro-reflective markers at up to a 350 Hz rate. Through triangulation, the system is able to measure the position and orientation of a vehicle that is outfitted with the markers. For system identification, the Vicon system provides measurements of the vehicle's response to an input with far more accuracy than on-board sensors. Vicon can also be used in the first phases of controller development. Lastly, because Vicon can provide the vehicle's coordinate position in the room, it can be used for

(a) Vicon cameras.

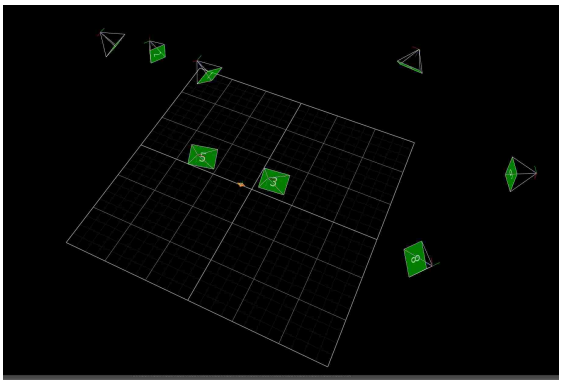

(b) Software view of room.

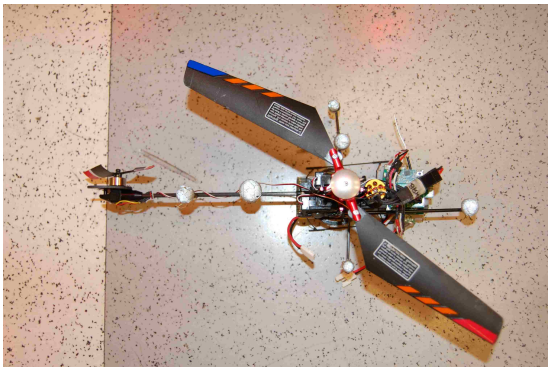

(c) Reflective markers affixed to helicopter.

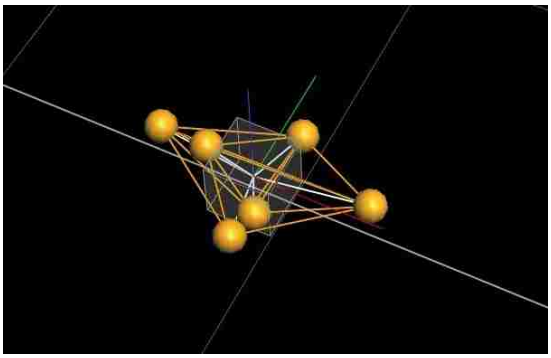

(d) Vicon rigid body model.

Figure 1.6: The Vicon motion capturing system tracks the 6DOF motion of the helicopter's rigid body.

position hold feedback or trajectory tracking. Outside of a Vicon system, IMU dead-reckoning, GPS, and visual-based algorithms can be used to this end, but during the testing phase, Vicon provides far more accurate measurements. The camera system, along with the program view of the helicopter rigid body, is pictured in Fig. 1.6.

1.7 State Space Representation

In general, theoretical principles will be presented as needed within their respective, relevant chapters. However, the linear state space model is central to the work performed throughout the thesis, and a brief overview is given here.

A state space model provides a structure from representing a collection of linearized first- and second- order ordinary differential equations (ODEs). A large theoretical framework has been established in the aerospace and controls communities for analyzing systems based on their state space structure. Furthermore, several model-based controllers have been successfully implemented on meso-scale helicopters utilizing state space models. As such, the state space structure was selected for formulating the micro-helicopter model.

The familiar state space form is

$$\dot{\vec{x}} = A\vec{x} + B\vec{u} \tag{1.1}$$

$$\vec{y} = C\vec{x} + D\vec{u} \tag{1.2}$$

where $\vec{x}$ is the vehicle states, $\vec{u}$ is the vehicle inputs, $\vec{y}$ is measurable information as a function of the states, A is the dynamics matrix, B is the controls matrix, C is the observer matrix, and D is the feed-through matrix.

The states $\vec{x}$ describe the vehicle's position (x, y, z), orientation (ϕ, θ, ψ), rotational rates (p, q, r), and translational states (u, v, w) at an instant in time. For this rotorcraft model, additional states are included to describe flapping angles (a, b) and flybar angles (c, d). Also, because we are primarily concerned with the vehicle's ability to hold hover, the states (z, w, ψ, r) are excluded from the model. The output

vector $\vec{y}$ are all states that can be measured by either on-board or off-board sensing. For experiments performed in this thesis, the outputs are those states which were measurable by Vicon and exclude the vehicle flapping and flybar states. The inputs $\vec{u}$ are lateral and longitudinal inputs $(\delta_{lat}, \delta_{lon})$ induced by servo inputs to the swashplate. Inputs for the main rotor rate and tail rotor rate $(\delta_{main}, \delta_{tail})$ are excluded from the models developed in this thesis; however, they are mentioned occasionally in descriptions of the helicopter dynamics. In summary, the state space vectors for the flybar model are

$$\vec{x} = [\phi\ \theta\ p\ q\ a\ b\ c\ d\ u\ v\ x\ y]^{\mathrm{T}} \tag{1.3}$$

$$\vec{y} = [\phi\ \theta\ p\ q\ u\ v\ x\ y]^{\mathrm{T}} \tag{1.4}$$

$$\vec{u} = [\delta_{lat}\ \delta_{lon}]^{\mathrm{T}}. \tag{1.5}$$

The flybarless helicopter model utilizes the same vectors, but excludes the flybar states $[c\ d]^{\mathrm{T}}$.

The dynamics matrix A includes aerodynamic stability derivatives and kinematic terms. The controls matrix B includes control derivative terms. Further definition of stability and control derivatives are given in Section 2.3.2. The stability and control derivatives are the "parameters" for which the system identification algorithm will systematically estimate values. The observer matrix C includes conversion terms from the vehicle states to the measured outputs - in this case, where the units measured in Vicon are the same as the states, the matrix is composed of ones and zeros. The feed-through matrix D is assumed zero for this work.

Chapter 2

Model Structure

2.1 Overview

The objective of system identification is to identify unknown parameters in a system model. In this thesis, the model takes the form of the state space equations shown in eqn (1.1), and the unknown parameters are the entries of the dynamics matrix A and control matrix B. The realization of a dynamics matrix is not unique, and there are several useful forms of A. However, system identification requires a model structure that adequately captures the vehicle modes without including unnecessary parameters. For MIMO systems, a practical way of formulating the structure is basing the parameters on physical relationships between the states. For the micro-helicopters, these relationships can be found from the rigid body equations of motion and the equations coupling the rotor dynamics, stabilizer bar dynamics, and the fuselage.

The following sections review derivations for linearized vehicle kinematics and rigid body equations of motion. The effects of rotor dynamics are discussed, and simplified flapping equations are derived. The rotor dynamics are then coupled to the rigid body dynamics, and the model is arranged into state space form for the flybarless helicopter. Stabilizer bar equations of motion are also presented and coupled to the flapping dynamics. A state space structure for the flybar helicopter,

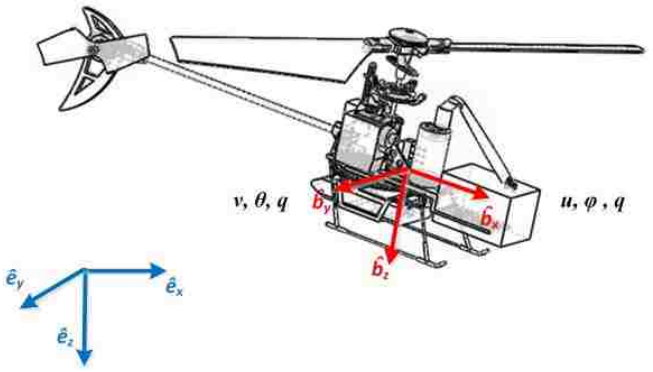

Figure 2.1: Diagram of inertial and body reference frames.

which incorporates the stabilizer bar dynamics, is presented.

2.2 Kinematics

Two coordinate frames are used to model the motion of the helicopter body. The body-fixed frame $\mathcal{B} = [\hat{b}_x\ \hat{b}_y\ \hat{b}_z]^{\mathrm{T}}$, with coordinate origin fixed at the vehicle's center of gravity (CG), is used to model the body dynamics associated with the forces and moments induced by aerodynamic affects and control inputs. The body-frame velocity states are $\vec{v}_B = u\hat{b}_x + v\hat{b}_y + w\hat{b}_z$ and the body-frame rotational rates are $\vec{\omega_B} = p\hat{b}_x + q\hat{b}_y + r\hat{b}_z$. The inertial frame $\mathcal{G} = [\hat{e}_x\ \hat{e}_y\ \hat{e}_z]$ is fixed on earth with its z-axis aligned with gravity such that $\vec{g} = g\hat{e}_z$. The inertial frame is used for modeling the effects of gravitational force on the helicopter body and for tracking the helicopter's position in the room. The inertial frame velocity states are $\vec{v}_G = \dot{x}\hat{e}_x + \dot{y}\hat{e}_y + \dot{z}\hat{e}_z$.

To relate the two coordinate frames, the attitude of the helicopter relative to the inertial frame is defined by Euler angles $[\phi\ \theta\ \psi]^{\mathrm{T}}$. A diagram of the relative reference frames is shown in Fig. 2.1. The standard aircraft rotation sequence for

transforming from the inertial frame to the body frame is to first rotate about the $\hat{e}_z$, then $\hat{e}_y$, and lastly $\hat{e}_x$ (a 3-2-1 rotation). Compounding the three rotation matrices results in the following transformation matrix (where c is shorthand for cosine and s for sine):

$$R_{BG} = \begin{bmatrix} \mathrm{c}\theta\mathrm{c}\psi & \mathrm{c}\theta\mathrm{s}\psi & -\mathrm{s}\theta \\ \mathrm{s}\phi\mathrm{s}\theta\mathrm{c}\psi - \mathrm{c}\phi\mathrm{s}\psi & \mathrm{s}\phi\mathrm{s}\theta\mathrm{s}\psi + \mathrm{c}\phi\mathrm{c}\psi & \mathrm{s}\phi\mathrm{c}\theta \\ \mathrm{c}\phi\mathrm{s}\theta\mathrm{c}\psi + \mathrm{s}\phi\mathrm{s}\psi & \mathrm{c}\phi\mathrm{s}\theta\mathrm{s}\psi - \mathrm{s}\phi\mathrm{c}\psi & \mathrm{c}\phi\mathrm{c}\theta \end{bmatrix}. \tag{2.1}$$

The body-frame position $\vec{r}_B$ of a vehicle located inertially at $\vec{r}_G = [x\ y\ z]^{\mathrm{T}}$ can be found by using this transformation:

$$\vec{r}_B = R_{BG}\vec{r}_G. \tag{2.2}$$

Likewise, the body-frame velocity $\vec{v}_B$ can also be found as a product of the transformation matrix and the inertial velocity $\vec{v}_G$,

$$\vec{v}_B = R_{BG}\vec{v}_G. \tag{2.3}$$

The gravity vector $\vec{g} = [0\ 0\ g]^{\mathrm{T}}$ can also be transformed into the body frame,

$$\vec{g}_B = R_{BG}\vec{g} = \begin{bmatrix} -g\mathrm{s}\theta \\ g\mathrm{c}\theta\mathrm{s}\phi \\ g\mathrm{c}\theta\mathrm{c}\phi \end{bmatrix}. \tag{2.4}$$

Because the rotation matrix exists in $SO(3)$, it can be shown that $R_{BG} = R_{GB}^{\mathrm{T}}$. Transforming from the body-frame back to the inertial frame uses this relationship:

$$\vec{v}_G = R_{BG}^{\mathrm{T}}\vec{v}_B = R_{GB}\vec{v}_B. \tag{2.5}$$

This is useful for tracking the vehicle in the inertial frame for outer-loop position-hold control where the vehicle inertial velocity v_G is regulated,

$$\vec{v}_G = \begin{bmatrix} \dot{x} \\ \dot{y} \\ \dot{z} \end{bmatrix} = R_{GB} \begin{bmatrix} u \\ v \\ w \end{bmatrix} . \tag{2.6}$$

The last step in developing the vehicle kinematics is to relate the body rotation rates $\vec{\omega}_B$ to the Euler angles. This is derived geometrically from the 3-2-1 transformation process. The relationship, derived in [13], is

$$\vec{\omega}_B = \begin{bmatrix} p \\ q \\ r \end{bmatrix} = \begin{bmatrix} 1 & 0 & -\mathrm{s}\theta \\ 0 & \mathrm{c}\phi & \mathrm{s}\phi\mathrm{c}\theta \\ 0 & -\mathrm{s}\phi & \mathrm{c}\theta\mathrm{c}\phi \end{bmatrix} \begin{bmatrix} \dot{\phi} \\ \dot{\theta} \\ \dot{\psi} \end{bmatrix} . \tag{2.7}$$

As an aside, the inverse of the transformation in eqn.(2.7) contains a $\tan\theta$, which is singular at $\theta = \pm\pi/2$. This singularity is one weakness of formulating the kinematics in terms of Euler angles. However, for modeling hover and trajectory tracking, this orientation would be outside of the helicopter's linear range of motion and, as such, irrelevant to the control objectives.

2.3 Rigid-Body Dynamics

The Newton-Euler equations of motion describe the six degrees of freedom (DOF) motion of the helicopter rigid body, represented in the inertial frame, for

fixed mass m and inertia I:

$$\vec{F} = m\frac{^{G}d\vec{v}_G}{dt} \tag{2.8}$$

$$\vec{M} = I\frac{^{G}d\vec{\omega}_G}{dt} \tag{2.9}$$

where $\vec{F}$ are the external forces applied to the body of the helicopter and $\vec{M}$ are the external moment applied about the CG.

For a 6DOF rotating body such as an aircraft, modeling the body in the fixed inertia frame is rather awkward. Since most of the forces and moments are aligned in directions parallel to the rotating body axes, it makes more sense to represent the forces and moments in this frame. The Reynold's Transport Theorem, a kinematic principle which relates moving reference frames, is used to express the forces and moments with respect to the body-fixed frame:

$$\vec{F} = m\dot{\vec{v}}_B + (\vec{\omega}_B \times m\vec{v}_G) \tag{2.10}$$

$$\vec{M} = I\dot{\vec{\omega}}_B + (\vec{\omega}_B \times I\vec{\omega}_B) \tag{2.11}$$

where $\vec{F} = X\hat{b}_x + Y\hat{b}_y + Z\hat{b}_z$ and $\vec{M} = L\hat{b}_x + M\hat{b}_y + N\hat{b}_z$. The inertia matrix, in body coordinates, is:

$$I = \begin{bmatrix} I_{xx} & 0 & -I_{xz} \\ 0 & I_{yy} & 0 \\ -I_{xz} & 0 & I_{zz} \end{bmatrix}. \tag{2.12}$$

The terms I_{xy} and I_{yz} are effectively zero, due to the vehicle's symmetry. The term I_{xz}, which is two orders of magnitude smaller than I_{xx}, was originally included in the model. However, during the system identification process, it was determined that

its effects on the dynamics were negligible. In the derivation of the model shown here, I_{xz} is neglected.

Expanding eqns (2.10–2.11) yields the following body-frame equations of motion:

$$X = m(\dot{u} - wq + vr) \tag{2.13}$$

$$Y = m(\dot{v} - ur + wp) \tag{2.14}$$

$$Z = m(\dot{w} - vp + uq) \tag{2.15}$$

$$L = qr(I_{yy} - I_{zz}) + I_{xx}\dot{p} \tag{2.16}$$

$$M = pr(I_{zz} - I_{xx}) + I_{yy}\dot{q} \tag{2.17}$$

$$N = pq(I_{xx} - I_{yy}) + I_{zz}\dot{r}. \tag{2.18}$$

These non-linear differential equations can be simulated in MATLAB using a function such as `ode45`. The next step in formulating a model suitable for system identification is to linearize the equations of motion.

2.3.1 Linearization

A set of non-linear vector equations $\vec{f}(\dot{\vec{x}}, \vec{x}, \vec{u}) = 0$ can be linearized using a multi-variable Taylor expansion of $\vec{f}$ about reference states x_0 and reference forcing inputs u_0 (or "system inputs"):

$$\vec{0} = E(\dot{\vec{x}} - \dot{\vec{x}}_0) + F(\vec{x} - \vec{x}_0) + G(\vec{u} - \vec{u}_0) + r(x, x_0, ...) \tag{2.19}$$

where

$$E = \left.\frac{\partial \vec{f}}{\partial \dot{\vec{x}}}\right|_{\dot{\vec{x}}_0, \vec{x}_0, \vec{u}_0}, \quad F = \left.\frac{\partial \vec{f}}{\partial \vec{x}}\right|_{\dot{\vec{x}}_0, \vec{x}_0, \vec{u}_0}, \quad G = \left.\frac{\partial \vec{f}}{\partial \vec{u}}\right|_{\dot{\vec{x}}_0, \vec{x}_0, \vec{u}_0} \tag{2.20}$$

and $r(x, x_0, ...)$ is a remainder that is assumed small enough to be neglected.

The terms $\Delta x = \vec{x} - \vec{x}_0$ and $\Delta u = \vec{u} - \vec{u}_0$ are perturbations away from the reference conditions. In terms of the perturbations, eqn (2.20) can be rewritten in the familiar state space form

$$\Delta\dot{\vec{x}} = A\Delta\vec{x} + B\Delta\vec{u} \tag{2.21}$$

where

$$A = -E^{-1}F, \quad B = -E^{-1}G. \tag{2.22}$$

The linearized versions of eqns (2.13–2.18) are:

$$\Delta\dot{u} = -w_0\Delta q + q_0\Delta w + v_0\Delta r + r_0\Delta v + \Delta X/m \tag{2.23}$$

$$\Delta\dot{v} = -u_0\Delta r + r_0\Delta u + w_0\Delta p + p_0\Delta w + \Delta Y/m \tag{2.24}$$

$$\Delta\dot{w} = -v_0\Delta p + p_0\Delta v + u_0\Delta q + q_0\Delta u + \Delta Z/m \tag{2.25}$$

$$\Delta\dot{p} = (-q_0\Delta r - r_0\Delta q)(I_{yy} - I_{zz})/I_{xx} + \Delta L/I_{xx} \tag{2.26}$$

$$\Delta\dot{q} = (-p_0\Delta r - r_0\Delta p)(I_{zz} - I_{xx})/I_{yy} + \Delta M/I_{yy} \tag{2.27}$$

$$\Delta\dot{r} = (-p_0\Delta q - q_0\Delta p)(I_{xx} - I_{yy})/I_{zz} + \Delta N/I_{zz}. \tag{2.28}$$

Note that terms associated with matrix G in eqn (2.22) are represented for now by the $\Delta\vec{F}$ and $\Delta\vec{M}$ terms, which will be expanded in the next section.

To simplify these equations further, we must assume a reference condition. Examples of reference conditions for vehicles, or vehicle "trim", include constant velocity in a rectilinear direction (i.e., a forward velocity of 1 m/s: $\vec{v}_{B_0} = [1\ 0\ 0]^{\mathrm{T}}$, $\vec{\omega}_{B_0} = [0\ 0\ 0]^{\mathrm{T}}$) and hover (i.e., $\vec{v}_{B_0} = \vec{\omega}_{B_0} = [0\ 0\ 0]^{\mathrm{T}}$). This model will later be used for testing the helicopter's ability to hold position in the presence of gust

disturbances, so the hover trim condition is assumed. For the hover trim condition, many of the terms in eqns (2.23–2.28) are zero. The equations simplify to the following relationships

$$\Delta\dot{u} = \Delta X/m \quad \Delta\dot{v} = \Delta Y/m \quad \Delta\dot{w} = \Delta Z/m \tag{2.29}$$

$$\Delta\dot{p} = \Delta L/I_{xx} \quad \Delta\dot{q} = \Delta M/I_{yy} \quad \Delta\dot{r} = \Delta N/I_{zz} \tag{2.30}$$

For linearized models where small perturbations from a trim condition are assumed, the small angle approximation is a useful mathematical tool that can be applied to the kinematic relationships. The small angle approximation states that for any angle $\angle\theta \ll 1$, $\sin\theta \approx 0$ and $\cos\theta \approx 1$. With the application of the approximation and recast into the linearized formulation, the kinematic relationships reduce to

$$\Delta\dot{x} = \Delta u, \quad \Delta\dot{y} = \Delta v, \quad \Delta\dot{z} = \Delta w \tag{2.31}$$

$$\Delta\dot{\phi} = \Delta p, \quad \Delta\dot{\theta} = \Delta q, \quad \Delta\dot{\psi} = \Delta r. \tag{2.32}$$

2.3.2 Stability Derivative Representation for Forces and Moments

The next step in developing the model is to expand the force and moment terms. Forces and moments are caused by aerodynamic effects, gravity, and control inputs. Discussion of aerodynamic stability derivatives and gravity force will be discussed here; however, the effects due to control inputs must be incorporated into a discussion of rotor dynamics and will be reserved for the next section.

Aerodynamic forces and moments are a result of often turbulent flows over the complex body and rotor geometries. They are typically determined through wind

tunnel tests or computational fluid dynamic (CFD) calculations. An example of an aerodynamic force relationship is, in the $\hat{b}_x$ direction,

$$X_{aero} = Q_u C_X A_C \tag{2.33}$$

where Q_u is the dynamic pressure, which is a function of u and the air density ρ, A_C is the capture area, and C_X is a non-dimensional force coefficient. Determining each aerodynamic force through first principles modeling would be an exceedingly involved task. Instead, we can assume that each force and moment is a function of the state variables. The resulting terms become parameters to be solved for in the system identification process. Using a Taylor series expansion (and ignoring higher order terms), the longitudinal force component can be expressed as

$$\Delta X = \frac{\partial X}{\partial u}\Delta u + \frac{\partial X}{\partial v}\Delta v + \frac{\partial X}{\partial p}\Delta p + \cdots \tag{2.34}$$

Each force $\Delta\vec{F}$ and moment $\Delta\vec{M}$ components can be expanded similarly.

The partial derivatives of the forces or moments with respect to the vehicle states are the stability derivatives. Each stability derivative also absorbs the mass m or inertia $I_{[\cdot]}$ terms from eqns (2.31–2.32) as well. An example of a stability derivative is the change in force X as a result of a change in forward velocity u,

$$\frac{\partial X}{\partial u}/m = X_u. \tag{2.35}$$

The stability derivative represents a simplified, linearized version of eqn (2.33). Generally, control derivatives are also included as part of the eqn (2.34) expansion. The control derivatives, for this model, will be included with the rotor dynamics,

which are discussed in the next section. The following stability derivatives were included in the final model: X_u, X_v, Y_u, Y_v, L_u, L_v, M_u, and M_v.

In addition to stability derivatives, gravity terms were also included in the model. Linearizing eqn (2.4) results in the following relationship:

$$\Delta X_{grav} = \Delta \dot{u}_{grav} m = -g\Delta\theta m \tag{2.36}$$

$$\Delta Y_{grav} = \Delta \dot{v}_{grav} m = g\Delta\phi m. \tag{2.37}$$

To simplify notation going forward, Δ symbols will be dropped from states. It can be assumed that all states $\vec{x}$ are perturbations more formally represented as $\Delta\vec{x}$.

2.4 Rotor Dynamics

For the micro-helicopters, all control forces and moments are derived from inputs to the helicopter's tail and main rotors. Because the effective plane of the rotor from which the force directions are derived (the "tip-path-plane") is generally not parallel with the hub plane, an accurate model should capture the rotor dynamics separately. The rotor dynamics can then be coupled to the rigid body dynamics. Fig. 2.2 illustrates the respective planes.

The importance of including rotor dynamics in full-scale rotorcraft system identification was observed during some of the very first experiments in the field [5]. A "quasi-steady" model would model the transient rotor dynamics as equivalent time delays and the steady state response as rigid body stability derivatives [14]. A "hybrid" model, on the other hand, models explicitly the rotor dynamics with

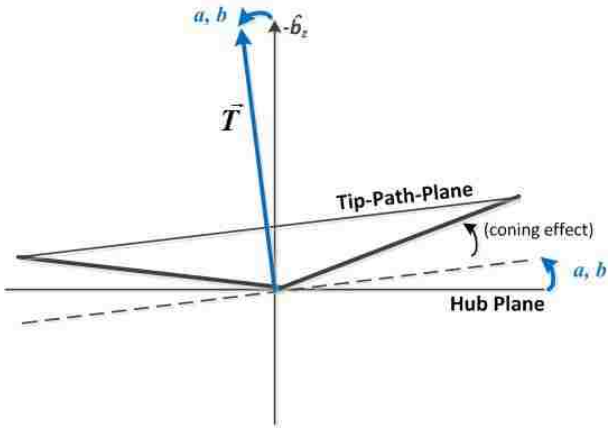

Figure 2.2: Flapping angle with respect to the hub plane.

additional states beyond those required for the 6DOF model. Mettler compares quasi-steady and hybrid models of the R-50 meso-scale helicopter and shows a large discrepancy between the two models [10]. On the other hand, Tischler shows good agreement when comparing quasi-steady and hybrid models for the full-scale UH-1H. The main contributing difference between the two vehicles is the magnitude of a value called the flapping stiffness, which will be explained in this section. The micro-scale helicopters modeled here are more similar to the Mettler helicopters and thus require a hybrid model.

The following section provides an overview of blade motion and presents simplified, first-order equations for modeling the rotor dynamics.

2.4.1 Blade Motion and Swashplate Mechanism

A rotor blade is, in essence, an airfoil. The main lift-generating velocity component on the rotor is derived from rotating about the rotor shaft. A trim rotor

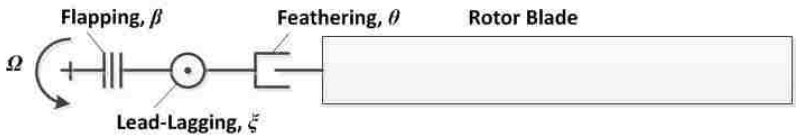

Figure 2.3: Besides rotating about the rotor shaft, the rotor blade has three additional degrees of freedom.

rate Ω_0 is required to generate enough thrust to balance the mass-gravity force on the helicopter so as to maintain hover. By rotating the rotors at a rate faster than Ω_0, the system generates enough force to overcome the gravity force and the vehicle ascends. The vehicle descends when the rotor rate Ω decreases below the hover rate Ω_0. The basic aerodynamics that describe the generation of thrust is based on blade element theory and is described in detail in [15]. The total thrust T_{main} generated by the micro-helicopter main rotor assembly (two blades) is given by

$$T_{main} = \frac{1}{3}\rho c R_{main}^3 \Omega^2 C_{l\alpha} \tag{2.38}$$

where ρ is the density of air, c is the chord length, R_{main} is the radius of the rotor, Ω is the rotor rate, and $C_{l\alpha}$ is the airfoil's lift curve slope. Because lift is generated by increasing the rotor speed Ω on the micro-helicopters, the control derivative δ_{main} for the main rotor input can be estimated by linearizing this equation. The thrust component is not considered in the model, so this equation is included solely for reference.

Besides rotating about the rotor shaft, a rotor blade has up to three additional degrees of freedom available depending on the assembly: lead-lagging, feathering, and flapping. The diagram in Fig. 2.3 is useful for visualizing these motions. The

lead-lagging motion is rotation ξ of the blade within the hub-plane. Feathering is rotation Θ of the blade about its length. Flapping is motion of the blade angle β normal to the hub plane. Note, the tail rotor, which is a very simple assembly and constructed of stiff material, experiences very little of any of this motion. (In the case of a full-scale rotorcraft, these effects may need to be included for the tail rotor as well.)

The cyclic inputs $(\delta_{lat}, \delta_{lon})$ increase the rotor blade's pitch angle from the nominal angle Θ_0. This is done through the swashplate mechanism, pictured for the flybarless helicopter in Fig. 2.4. A signal from the on-board control unit actuates a servo, which tilts the swashplate. There are two servos—one for lateral inputs and one for longitudinal inputs. A second plate, which rotates with rotor shaft, sits atop the swashplate. The secondary plate has two rods that activate the pitch angle of the rotors. When the swashplate tilts (either laterally or longitudinally or a combination of both), the rods will move up and down as they rotate about the shaft - causing, in turn, the pitch angle of the blades to increase and decrease as a function of their position Ψ within the plane. The pitch angle is represented by the formula

$$\Theta(\Psi) = \Theta_0 - A_1 \cos\Psi - B_1 \sin\Psi \tag{2.39}$$

where A_1 and B_1 are a function of the magnitude of the cyclic inputs

$$A_1 = A_{lat}\delta_{lat}, \quad B_1 = B_{lon}\delta_{lon}. \tag{2.40}$$

However, it is not the actual increase of angle of attack that induces lateral or longitudinal motion, but rather the flapping that occurs as a result of the angle of

Figure 2.4: The servos tilt the swashplate which, through mechanical arms, pitches the rotor blades.

attack. The physics that induce the flapping and the resulting, simplified equations of motion for the flapping dynamics will be presented in the following section.

2.4.2 Flapping Dynamics

Flapping dynamics are easily visualized by representing the blade as a rigid beam and balancing the forces and moments. Fig. 2.5 depicts the free-body diagram. The primary forces acting on the blade as it rotates about the shaft include: the aerodynamic force F_{aero}, the centrifugal force F_{cent}, the inertia force F_{inertia}, and the restoring moment produced by the flapping restraint. A more complete expression for the aerodynamic forces would include terms for vehicle angular and linear acceleration, as well as Coriolis acceleration, which are derived in detail in [16]. A simplified expression will be shown here by balancing forces at a radial distance y

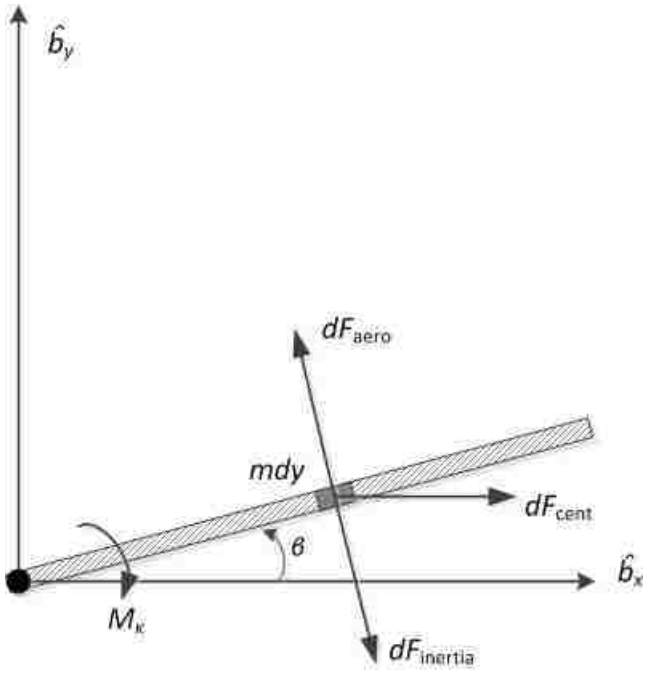

Figure 2.5: The flapping equations of motion are derived by balancing the aerodynamic, inertial, and centrifugal moments about the blade.

from the flapping hinge and for a mass per unit length m_r. The derivation is a summary of the derivation provided by Mettler [10].

The aerodynamic force is a sum of the lift F_{lift} and drag F_{drag} forces acting on the blade element:

$$dF_{\text{aero}} = dF_{\text{lift}} \cos\Phi + dF_{\text{drag}} \sin\Phi \tag{2.41}$$

where Φ is the angle between the hub plane and the net velocity component angle. The aerodynamic inflow is a result of several velocity components acting on the blade and will not be expanded upon here. Instead, we rely on a safe assumption that $\Phi \ll 1$. Eqn (2.41) reduces to

$$dF_{\text{aero}} = dF_{\text{lift}}. \tag{2.42}$$

The centrifugal force is given by the expression

$$dF_{\text{cent}} = m_r dy \Omega^2 y \beta \tag{2.43}$$

and the force due to the blade inertia is

$$dF_{\text{inertia}} = -m_r dy \ddot{\beta}. \tag{2.44}$$

The restoring moment from the flapping spring is

$$M_\kappa = -\kappa_\beta \beta. \tag{2.45}$$

We now balance the moments about the blade, such that

$$\sum M_{\text{blade}} = y(F_{\text{aero}} + F_{\text{cent}} + F_{\text{inertia}}) + M_\kappa = 0. \tag{2.46}$$

The full expression for balancing moments, then, is

$$\int_0^{R_{\text{main}}} y(dF_{\text{lift}})dy - \int_0^{R_{\text{main}}} y(m_r \Omega^2 y \beta)dy + \int_0^{R_{\text{main}}} y(m_r y \ddot{\beta})dy - \kappa_\beta \beta = 0. \tag{2.47}$$

Rearranging this equation yields

$$\int_0^{R_{\text{main}}} y(dF_{\text{lift}})dy - \int_0^{R_{\text{main}}} m y^2 dy \left[\ddot{\beta} + \omega^2 \beta\right] - \kappa_\beta = 0. \tag{2.48}$$

By definition, $I_{\text{blade}} = \int_0^{R_{\text{main}}} m y^2 dy$. Also, at this point, we redefine the flapping derivative with respect to angular blade position, rather than time,

$$\ddot{\beta} = \Omega^2 \frac{\partial^2 \beta}{\partial \Psi^2} = \Omega^2 \beta''. \tag{2.49}$$

Rearranging the equation into standard mass-spring-damper form, results in the following expression,

$$\beta'' + \left(1 + \frac{\kappa_\beta}{I_\beta \Omega^2}\right)\beta = \frac{1}{I_\beta \Omega^2} \int_0^{R_{\text{main}}} y(dF_{\text{lift}})dy \tag{2.50}$$

The forcing term in this differential equation is the lift on the blade. This lift force is dependent on the blade's angle of attack. It is seen here that an increase in that angle of attack by a cyclic input ($\delta_{lat}, \delta_{lon}$) induces the flapping motion. The plane created by the flap is called the tip-path-plane (TPP). As the TPP is tilted with respect to the hub plane, the thrust vector also tilts, inducing a moment on the helicopter that allows it to rotate and translate.

It is also interesting to note here that the flap does not necessarily occur at the same angular position Ψ as the forcing (cyclic) input. An examination of eqn (2.50) shows that the natural frequency of the flap, normalized by the rotor rate, is

$$\lambda_\beta = \frac{\omega_\beta}{\Omega} = \sqrt{1 + \frac{\kappa_\beta}{I_\beta \Omega^2}}. \tag{2.51}$$

For a teetering rotor with no flapping restraint, $\kappa_\beta \approx 0$, the natural frequency λ is equal to the rotor rate Ω. As this is a second-order system, the maximum deflection will occur at a 90-degree phase shift from where the rotor was excited. So if a lateral input is provided at a position $\Psi = 180°$, the flap will occur at $\Psi = 270°$, which will tilt the force vector in the $\hat{b}_y$ direction. Because the micro-helicopter's rotor systems do not have hinges, the flapping spring constant κ_β is dependent on the material properties of the rotor, as well as how tightly it is secured to the rotor hub. Mechanically, the system is designed with a small phase offset on the swashplate. The system identified model will capture these effects.

This model, based on simplified equations of motion derived by Mettler, assumes the following general solution for the flapping motion:

$$\beta(\Psi) = \beta_0 - a(t)\cos\Psi - b(t)\sin\Psi. \tag{2.52}$$

(Note: In more formal realizations, the notation β_{1c} is generally used for a and β_{1s} is generally used for b.) Combining this solution with the equation for rotor pitch angle, eqn (2.39), and the physics involved in defining aerodynamic lift [15], the following simplified equations of motion are derived:

$$\frac{16}{\gamma\Omega}\dot{a} = -a - \frac{16}{\gamma\Omega}q + \frac{1}{\Omega}p + \frac{8}{\gamma\Omega^2}\frac{\kappa_\beta}{I_\beta}b - B_1 \tag{2.53}$$

$$\frac{16}{\gamma\Omega}\dot{b} = -b - \frac{16}{\gamma\Omega}p + \frac{1}{\Omega}q + \frac{8}{\gamma\Omega^2}\frac{\kappa_\beta}{I_\beta}a - A_1, \tag{2.54}$$

where the lock number γ is defined as

$$\gamma = \frac{\rho c C_{l\alpha} R^4}{I_\beta}. \tag{2.55}$$

The lock number is the ratio between aerodynamic lift and inertia forces on the blade.

For the purpose of the state space model, a flapping constant τ_f is defined as

$$\tau_f = \frac{16}{\gamma\Omega}. \tag{2.56}$$

The coefficients for the other states are assigned as stability derivatives. The final, simplified equations incorporated into the model are

$$\tau_f\dot{a} = -a - \tau_f q + A_b b + A_{lon}\delta_{lon} \tag{2.57}$$

$$\tau_f\dot{b} = -b - \tau_f p + B_a a + B_{lat}\delta_{lat}. \tag{2.58}$$

Additional control derivatives A_{lat} and B_{lon} are also included to capture additional dynamics.

2.4.3 Coupling Rotor and Rigid Body Dynamics

The thrust force $\vec{T}_P$ acts normal to the tip-path-plane. With a TPP coordinate axis $\mathcal{P} = [\hat{p}_x\ \hat{p}_y\ \hat{p}_z]$, the thrust vector $\vec{T}_P = -T\hat{p}_z$. To transform from the TPP to the body frame, one first rotates about $\hat{p}_x$, then $\hat{p}_y$, and lastly $\hat{p}_z$. (The rotation about $\hat{p}_z$ is by $0°$, so the rotation matrix reduces to the identity matrix.) The compound rotation matrix is

$$R_{BP} = \begin{bmatrix} ca & 0 & sa \\ sa\ cb & cb & -ca\ sb \\ -cb\ sa & sb & ca\ cb \end{bmatrix}. \tag{2.59}$$

Transformed into the body frame, the thrust vector becomes

$$\vec{T} = R_{BP}\vec{T}_P = \begin{bmatrix} -\sin a \\ \sin b \cos a \\ -\cos a \cos b \end{bmatrix} T \approx \begin{bmatrix} -Ta \\ Tb \\ -T \end{bmatrix}. \tag{2.60}$$

The moments produced by the thrust and blade flapping act at a distance h from the vehicle CG. Additionally, the flapping spring exerts a moment that also torques the helicopter. Assuming the spring acts about the center of the rotor hub, the combined moments due to rotor flapping are

$$L_{flap} = (hT + \kappa_\beta)b, \quad M_{flap} = (hT + \kappa_\beta)a. \tag{2.61}$$

The stability derivatives that link the rotor dynamics to the rigid body are

$$L_b = (hT + \kappa_\beta)/I_{xx}, \quad M_a = (hT + \kappa_\beta)/I_{yy}. \tag{2.62}$$

The force components caused by the tilt of the TPP are

$$X_{flap} = Ta, \quad Y_{flap} = -Tb \tag{2.63}$$

and the resulting stability derivatives are

$$X_a = T/m, \quad Y_b = -T/m. \tag{2.64}$$

At hover, the thrust force remains approximately constant such that,

$$T = W = mg, \tag{2.65}$$

where W is the weight of the vehicle. This means $X_a \approx -Y_b \approx -g$.

2.4.4 State Space Model: Flybarless Helicopter

The state space model for a flybarless helicopter can be assembled by collecting the linearized rigid body and rotor dynamics together:

$$\begin{bmatrix} \dot{\phi} \\ \dot{\theta} \\ \dot{p} \\ \dot{q} \\ \dot{a} \\ \dot{b} \\ \dot{u} \\ \dot{v} \end{bmatrix} = \begin{bmatrix} 0 & 0 & 1 & 0 & 0 & 0 & 0 & 0 \\ 0 & 0 & 0 & 1 & 0 & 0 & 0 & 0 \\ 0 & 0 & 0 & 0 & 0 & L_b & L_u & L_v \\ 0 & 0 & 0 & 0 & M_a & 0 & M_u & M_v \\ 0 & 0 & 0 & -1 & -\frac{1}{\tau_f} & \frac{A_b}{\tau_f} & 0 & 0 \\ 0 & 0 & -1 & 0 & \frac{B_a}{\tau_f} & -\frac{1}{\tau_f} & 0 & 0 \\ 0 & -g & 0 & 0 & -g & 0 & X_u & 0 \\ g & 0 & 0 & 0 & 0 & g & 0 & Y_v \end{bmatrix} \begin{bmatrix} \phi \\ \theta \\ p \\ q \\ a \\ b \\ u \\ v \end{bmatrix} + \begin{bmatrix} 0 & 0 \\ 0 & 0 \\ 0 & 0 \\ 0 & 0 \\ A_{lat} & A_{lon} \\ B_{lat} & B_{lon} \\ 0 & 0 \\ 0 & 0 \end{bmatrix} \begin{bmatrix} \delta_{lat} \\ \delta_{lon} \end{bmatrix} \tag{2.66}$$

The analysis and controllers developed in this thesis are specifically designed for position hold. The heave and yaw dynamics are assumed decoupled from the

dynamics associated with the cyclic control. As such, the states $\psi, r, w,$ and z are excluded from the model.

2.5 Flybar Dynamics

Next, the dynamics of the stabilizer bar, or flybar, are developed and incorporated into the state space structure found in eqn (2.66).

The stabilizer bar on the Walkera CB100 consists of a rod with weights attached to the ends. This type of stabilizer bar is generally referred to as a Bell flybar. The flybar is positioned at an approximately 45° angle to the main rotors. A "see-saw" mechanism allows the flybar to rotate in a plane independent of the main rotors. The weights on the flybar ensure that it is not affected by aerodynamic forces, and the angular moment associated with the flybar's inertia makes its plane resistent to rotation. When the rotor plane is perturbed by either a wind gust or a pilot input, the flybar plane remains fairly stationary, rotating parallel to the x-y inertial plane. However, a sustained perturbation of the helicopter's fuselage results in a dramatic shift of the flybar plane to resume its position parallel to the hub plane.

The flybar is connected to the main rotors with a mechanical mixer arm that perturbs the blade pitch. If the flybar is rotating parallel to the hub plane, then it has no effect on the blade pitch. However, if the hub plane is perturbed with respect to the flybar (i.e., when the helicopter pitches or rolls), then the flybar induces an opposing cyclic pitch input. Thus, the flybar operates as a mechanical device that

feeds back the vehicle attitude with respect to its plane.

The flybar dynamic states are modelled similarly to the flapping dynamics, where c represents a tilt of the flybar in the lateral direction (inducing longitudinal feedback) and d represents a tilt in the longitudinal direction (inducing lateral feedback). A first order equation is used,

$$\beta_{sb}(\Psi) = c\cos\Psi + d\sin\Psi. \tag{2.67}$$

The gyroscopic equations of motion provided by Johnson [17] are used to model the flybar's motion:

$$\begin{bmatrix} I_{sb}s^2 + (C_R + C_F)s & 2\Omega_{sb}I_{sb}s + C_R\Omega_{sb} \\ -(2\Omega_{sb}I_{sb}s + C_R\Omega_{sb}) & I_{sb}s^2 + (C_R + C_F)s \end{bmatrix} \begin{bmatrix} c \\ d \end{bmatrix} = \begin{bmatrix} I_{sb}s & 2\Omega_{sb}I_{sb} \\ -2\Omega_{sb}I_{sb} & I_{sb}s \end{bmatrix} \begin{bmatrix} p \\ q \end{bmatrix} \tag{2.68}$$

where I_{sb} is the inertia of the flybar, C_R and C_F are the damping coefficients in the rotating and fixed coordinate frames respectively, and Ω_{sb} is the rotation rate of the flybar. Reducing the order of c and d to s and neglecting C_F results in the following relationship:

$$\begin{bmatrix} c \\ d \end{bmatrix} = \frac{2I_{sb}/C_R}{4\frac{I_{sb}}{C_R}s + 1} \begin{bmatrix} p \\ q \end{bmatrix}. \tag{2.69}$$

After taking the reverse Laplace transform and rearranging, the following equations were used for developing the model:

$$\tau_{sb}\dot{c} = c + \frac{1}{2}\tau_{sb}p \tag{2.70}$$

$$\tau_{sb}\dot{d} = d + \frac{1}{2}\tau_{sb}q \tag{2.71}$$

where

$$\tau_{sb} = 4\frac{I_{sb}}{C_R}. \tag{2.72}$$

The equations are coupled to the flapping dynamics with the derivatives A_c, A_d, B_c, and B_d. These derivatives represent the change in blade pitch Θ as a result of the flybar motion and should be opposite in sign of the control derivatives A_{lat}, A_{lon}, B_{lat}, and B_{lon}. The derivatives A_c and B_d represent the primary inputs. Because the bar is positioned at a 45° angle, the bar also contributes to off-axis flapping motion, which is captured with the A_d and B_c derivatives.

2.5.1 State Space Model: Flybar Helicopter

The state space model for the flybar helicopter was derived by incorporating the flybar equations of motion, eqn (2.70), into the state space structure for the flybarless helicopter, eqn (2.66),

$$\begin{bmatrix} \dot{\phi} \\ \dot{\theta} \\ \dot{p} \\ \dot{q} \\ \dot{a} \\ \dot{b} \\ \dot{c} \\ \dot{d} \\ \dot{u} \\ \dot{v} \end{bmatrix} = \begin{bmatrix} 0 & 0 & 1 & 0 & 0 & 0 & 0 & 0 & 0 & 0 \\ 0 & 0 & 0 & 1 & 0 & 0 & 0 & 0 & 0 & 0 \\ 0 & 0 & 0 & 0 & 0 & L_b & 0 & 0 & L_u & L_v \\ 0 & 0 & 0 & 0 & M_a & 0 & 0 & 0 & M_u & M_v \\ 0 & 0 & 0 & -1 & -\frac{1}{\tau_f} & \frac{A_b}{\tau_f} & A_c & A_d & 0 & 0 \\ 0 & 0 & -1 & 0 & \frac{B_a}{\tau_f} & -\frac{1}{\tau_f} & B_c & B_d & 0 & 0 \\ 0 & 0 & 0 & \frac{1}{2} & 0 & 0 & -\frac{1}{\tau_{sb}} & 0 & 0 & 0 \\ 0 & 0 & \frac{1}{2} & 0 & 0 & 0 & 0 & -\frac{1}{\tau_{sb}} & 0 & 0 \\ 0 & -g & 0 & 0 & -g & 0 & 0 & 0 & X_u & 0 \\ g & 0 & 0 & 0 & 0 & g & 0 & 0 & 0 & Y_v \end{bmatrix} \begin{bmatrix} \phi \\ \theta \\ p \\ q \\ a \\ b \\ c \\ d \\ u \\ v \end{bmatrix} + \begin{bmatrix} 0 & 0 \\ 0 & 0 \\ 0 & 0 \\ 0 & 0 \\ A_{lat} & A_{lon} \\ B_{lat} & B_{lon} \\ 0 & 0 \\ 0 & 0 \\ 0 & 0 \\ 0 & 0 \end{bmatrix} \begin{bmatrix} \delta_{lat} \\ \delta_{lon} \end{bmatrix} \tag{2.73}$$

.

2.6 Conclusions

Using the kinematic relationships and dynamic equations of motion, state space structures for both the flybar and flybarless helicopters were derived. These structures have several properties that will benefit the system identification process. A majority of the matrix has 0, 1, or g entries, minimizing the number of parameters that require identification. The stability and control derivatives that do require identification have physical meanings associated with them, which can guide the system identification process. The number of these derivatives was minimized to ensure that the system is not over-parametrized. The importance of these properties

will be seen clearly in the next chapter as the process of system identification is explored.

Chapter 3

System Identification

3.1 Overview

System identification is the process of determining a mathematical model for a system based on measured input and output data. The process involves first collecting data that represents the dynamic response of the vehicle. This is done by exciting the vehicle with control inputs over the frequency range of interest, and then measuring the translational and rotational rate responses. After the data is collected, a model is developed that simulates the output response to the same inputs as closely as possible. The mathematical model here takes the form of the linear state space models derived in Chapter 2, where the unknown stability and control derivatives are parameters to be estimated. The following section discusses the process of parameter estimation first, as understanding this process provides motivation for data collection methods. Data collection is discussed next, and then the final results of the system identification process are presented.

3.2 Parameter Estimation

The procedure for determining the unknown stability and control derivatives—or "parameters" $\hat{\theta}$—that best represent the behavior of the system is, in effect, a

data fitting process. The system identification process involves either "fixing" or "freeing" each entry of the A and B matrices. Fixed entries are typically entries with known values, such as zeros, ones, or the gravitational constant g. Free entries are the stability and control derivatives that need to be numerically solved. Over-parameterizing, or having too many free parameters, may result in non-convergence within the parameter identification algorithm. Not including enough parameters, however, may result in the exclusion of important vehicle modes. This is motivation for developing a physically relevant model, such as that developed in Chapter 2.

The quality of the identified model depends heavily on the designer's familiarity with the physics of the system, as well as "tricks" for nudging the parameter identification algorithm closer to an expected and reasonable solution. The process of developing these models involved re-running the estimation algorithm several times, adjusting different aspects of the model each time. Four major challenges were encountered during the process:

- **Highly Coupled Dynamics** Unlike aircraft, the lateral and longitudinal dynamics of the helicopters are highly coupled. For instance, a roll input to the helicopter will result in both a rolling and pitching motion. As such, it was difficult to break the model into decoupled sub-models (i.e., identify parameters associated with longitudinal and lateral dynamics separately, and then concatenate the matrices). This inherent property of the helicopters is central to the other challenges presented here. It is also motivation for using simultaneous, multi-sinusoidal inputs, as discussed later in this section.

- **Minimizing the Number of Free Parameters** Limiting the number of free parameters for each run of the parameter estimation algorithm was essential for the model to converge in a reasonable length of time. This technique can usually be employed by identifying decoupled dynamics separately—however, this was more difficult to do with the helicopters.

- **Initial Guesses for Parameters** The output error algorithm solves for the parameters by iteratively changing the initial parameter guess $\hat{\theta}_0$ by $\Delta\hat{\theta}$ until the convergence criteria is met. If the initial parameter is not close enough to the physical value, the algorithm may converge to different local minima—or it may not even converge at all. Because the micro-helicopters are on a scale significantly smaller than previously identified helicopters, using values from these previously developed models did not produce convergence. Instead, the model was built up in steps, starting with a low-order model, and identifying only a couple parameters at a time. With only a few parameters identified per run, it was possible to try different combinations of orders of magnitudes or signs for each parameter initial guess. Again, this was more challenging because the lateral and longitudinal dynamics could not be decoupled.

- **Physically Relevant Model Structure** Although the dynamics matrix A can take many forms, it was the experience here that having physically relevant parameters resulted in a more accurate model. Specifically, the final equations of motion chosen for the flybar dynamics were selected after experimenting with other forms. After updating the equations of motion to eqn

(2.70), the model results improved significantly and more similarities were apparent between the eigenstructures of the flybar and flybarless helicopter. While the previous models predicted the behavior of the system decently and was sufficient for model-based control, the finalized model provided more insight into the system characteristics.

The method taken here started with reduced order models and built them up systematically to full-state models for both the helicopters. Initial estimates for the parameters were refined at each stage.

1. The decoupled lateral and longitudinal dynamics were identified first. For lateral dynamics, this included τ_f, τ_{sb}, L_b, B_d, and B_{lat}; for longitudinal dynamics, it included τ_f, τ_{sb}, M_a, A_c, and A_{lon}. An example of the reduced order lateral dynamics model is

$$\begin{bmatrix} \dot{p} \\ \hat{\theta}_1 \dot{b} \\ \hat{\theta}_2 \dot{d} \end{bmatrix} = \begin{bmatrix} 0 & \hat{\theta}_3 & 0 \\ -\hat{\theta}_1 & -1 & \hat{\theta}_4 \\ \hat{\theta}_2 & 0 & -1 \end{bmatrix} \begin{bmatrix} p \\ b \\ d \end{bmatrix} + \begin{bmatrix} 0 \\ 1 \\ 0 \end{bmatrix} \hat{\theta}_5 \tag{3.1}$$

   where $\hat{\theta}_1 = \tau_f$, $\hat{\theta}_2 = \tau_{sb}$, $\hat{\theta}_3 = L_b$, $\hat{\theta}_4 = B_d$, and $\hat{\theta}_5 = B_{lat}$. These initial estimates were poor, since the dynamics are inherently very coupled.

2. Next, the lateral and longitudinal states were collected into a coupled model. Coupling parameters A_b, B_a, A_{lon}, and B_{lat} were identified. The time constants τ_f and τ_{sb}, which were identified separately for lateral and longitudinal states in Step 1, were equated—that is, the same τ_f was used for both a and b states.

3. The derivatives X_u and Y_v were isolated from the rest of the model and identified separately. The translational velocity states (u,v) are mostly dependent on the the attitude (θ,ϕ), so the model was isolated as follows,

$$\begin{bmatrix} \dot{u} \\ \dot{v} \end{bmatrix} = \begin{bmatrix} \hat{\theta}_1 & 0 \\ 0 & \hat{\theta}_2 \end{bmatrix} \begin{bmatrix} u \\ v \end{bmatrix} + \begin{bmatrix} 0 & -9.8 \\ 9.8 & 0 \end{bmatrix} \begin{bmatrix} \phi \\ \theta \end{bmatrix}. \tag{3.2}$$

where $\hat{\theta}_1 = X_u$ and $\hat{\theta}_2 = Y_v$. Because ϕ and θ were measured variables, they could be used effectively as inputs for identifying these stability derivatives.

4. Lastly, the aerodynamic stability derivatives M_u, M_v, L_u, L_v, X_v, and Y_u were identified.

Each step involved first solving for the new parameters with the parameters from the previous step fixed—then freeing all the parameters and allowing the whole model to iterate. Beyond just these steps, the process required several iterations of trying new parameter guesses and fixing/freeing different aspects of the dynamics. Whether or not an iteration offered improvement to the model was judged based on the Cramer-Rao bound of the parameter and the normalized root mean square error of the simulated results, which will be discussed next. Also, similarities in the flybar and flybarless helicopter models were expected, especially relating to aerodynamic derivatives (i.e., M_u and L_v) and the system eigenvalues. The iteration was judged based on improvements in these areas as well.

3.3 Output Error Method

Analysis of the input and output system can be performed in either the frequency or the time domain. Using a time domain method such as output error, the parameters are systematically varied to reduce the error between the model-simulated response to the test inputs and the actual measured response of the vehicle. The frequency domain method minimizes the error between the models analytical frequency responses and frequency responses obtained from the experimental input and output data. Rotorcraft system identification has traditionally been performed in the frequency domain, and as such, this was the first approach. However, the unstable, highly-coupled nature of the vehicles resulted in low coherence in the frequency domain. It was found that time domain methods had more flexibility in this respect and employing the output error method ultimately proved successful.

The output error method is an algorithm that systematically varies the model parameters to minimize the difference between the measured outputs of the system and the outputs obtained using the data set's input sequences in a model simulation. Fig. 3.1 provides a block diagram of the routine. SIDPAC (System Identification Programs for AirCraft), a software toolbox written for MATLAB written by Morelli [18], was used to implement output error for the micro-helicopters. SIDPAC is used ubiquitously for both industry and research laboratory system identification applications. Detailed descriptions for the output error algorithms are provided in [19], along with derivations and proofs for the optimization routines. The following

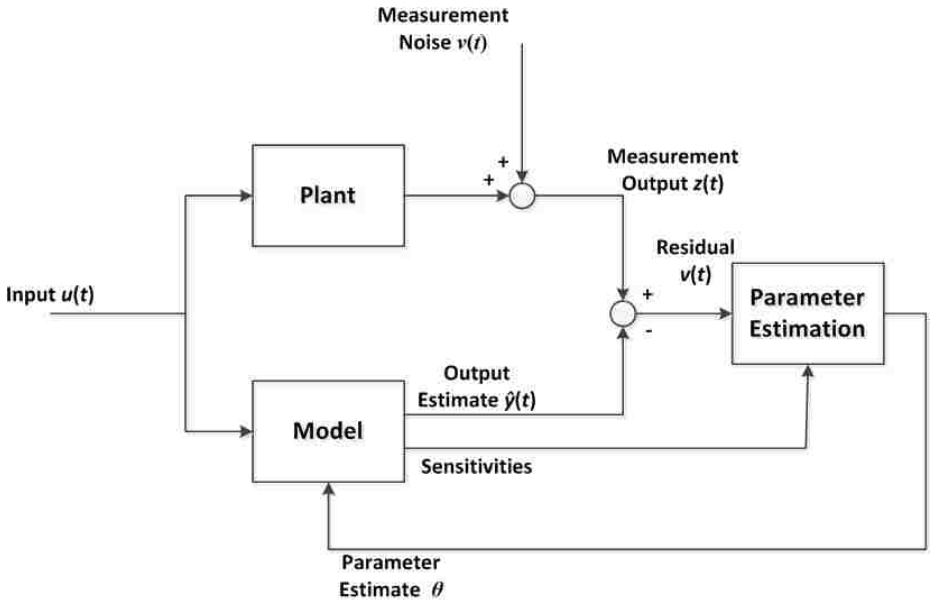

Figure 3.1: Block diagram of output error routine.

section summarizes the algorithm.

The model form assumed for the output error method is

$$\vec{y} = G\vec{u}. \tag{3.3}$$

The system G is the transfer function from the inputs $\vec{u}$ to the outputs $\vec{y}$ defined by the state space matrices,

$$G = C\left(sI - A\right)^{-1} B. \tag{3.4}$$

The unknown stability and control derivatives are the unknown parameters $\hat{\theta}$ that need to be identified. Additionally, it is assumed that the actual measured outputs of the system $\vec{z}$ is corrupted by zero-mean, white process noise $\vec{\nu}$ with covariance matrix R. Each measurement i is therefore represented as

$$\vec{z}(i) = \vec{y}(i) + \vec{\nu}(i); \quad \vec{\nu} \text{ is } \mathbb{N}(0, R); \quad i = 1, ..., N \tag{3.5}$$

Model parameter estimates are then found by minimizing the cost function

$$J(\vec{\theta})^1 = \frac{1}{2}\sum_{i=1}^{N}[\vec{z}(i) - \vec{y}(i)]\hat{R}^{-1}[\vec{z}(i) - \vec{y}(i)]^{\mathrm{T}} \tag{3.6}$$

where

$$\hat{R} = \frac{1}{N}\sum_{i=1}^{N}\vec{v}(i)\vec{v}(i)^{\mathrm{T}} \tag{3.7}$$

and $\vec{v}$ are the estimate residuals,

$$\vec{v}(i) = \vec{z}(i) - \vec{y}(i). \tag{3.8}$$

Optimization of the cost-function is performed using the Newton-Rhaphson, where the change in parameters is specified by the first and second-order gradients of the cost function. The expression for the updated parameters is

$$\hat{\theta} = \theta_0 + \Delta\hat{\theta} \tag{3.9}$$

$$\Delta\hat{\theta} = -M^{-1}_{\theta=\theta_0}\vec{g}_{\theta=\theta_0} \tag{3.10}$$

where

$$M_{\theta=\theta_0} = -E\left[\frac{\partial^2 \ln \mathbb{L}(Z_N|\theta)}{\partial\theta\partial\theta^{\mathrm{T}}}\right] \tag{3.11}$$

$$= \sum_{i=1}^{N} S^{\mathrm{T}}(i)\hat{R}^{-1}S(i) \tag{3.12}$$

$$\vec{g}_{\theta=\theta_0} = \sum_{i=1}^{N}[S^{\mathrm{T}}(i)\hat{R}^{-1}\vec{\nu}(i)]_{\theta=\theta_0} \tag{3.13}$$

and

$$S(i) = \frac{\partial\vec{y}}{\partial\theta}\ . \tag{3.14}$$

[1]The vector arrow will be dropped from θ henceforth for simplicity.

The Fisher information matrix M gives the probability of obtaining measured outputs Z_N given the parameter estimates $\hat{\theta}$; $\vec{g}$ is the cost gradient; and the sensitivity matrix S is the sensitivity of the model output to changes in the parameter estimate. The iterative solver alternates between solving for $\hat{R}$ in eqn (3.6) given a set of parameters $\hat{\theta}$, then fixing $\hat{R}$ in eqn (3.9) and solving for the updated parameters.

The solver is terminated after a set of convergence criteria are satisfied. The convergence criteria includes:

1. the change in cost function $J(\hat{\theta})$ remains minimal for a specified number of consecutive iterations.
2. the elements of the cost function gradient $J(\hat{\theta})$ are sufficiently close to zero.
3. the update in parameters $\Delta\hat{\theta}$ is sufficiently small.
4. the change in the covariance matrix $\hat{R}$ remains minimal for a specified number of iterations.

The final parameters $\hat{\theta}$ are substituted in for the stability and control derivatives to complete the state space models.

The output error algorithm is implemented with the `oe` function included in the SIDPAC toolbox. Inputs to the function include the input sequences used for data collection $\vec{u}\left(\vec{t}\right)$, the measured outputs of the system $\vec{z}\left(\vec{t}\right)$, the associated time vector $\vec{t}$, and a function representing the system model G. The `oe` function returns the estimates for the model parameters $\hat{\theta}$, the simulated system response $\vec{y}$, and the Cramer Rao lower bounds.

Two objective metrics were used for judging the quality of a simulated re-

sult: the Cramer Rao lower bounds (CRB) and the normalized root means square error (NRMSE). The Cramer Rao lower bounds is the variance of the estimated parameters $\hat{\theta}$ as related to the Fisher information matrix,

$$\mathrm{Cov}(\hat{\theta}) \geq M^{-1} \tag{3.15}$$

assuming ν is white noise. However, the residuals in this case are a result of model non-linearities or unmodeled dynamics, and we cannot assume they are white. A generalized Cramer Rao bound accounts for residual coloring,

$$\mathrm{Cov}(\hat{\theta}) \geq M^{-1} \left[\sum_{i=1}^{N} S^{\mathrm{T}}(i) R^{-1} \sum_{j=1}^{N} \mathcal{R}_{\nu\nu}(i-j) R^{-1} S(j) \right] M^{-1}, \tag{3.16}$$

where $\mathcal{R}_{\nu\nu}(i-j)$ is the output residual autocorrelation matrix. The CRB should be minimized. The NRMSE is defined as

$$NRMSE = 1 - \frac{\| \vec{z} - \vec{y} \|}{\| \vec{z} - \bar{\vec{z}} \|}. \tag{3.17}$$

A NRMSE of one represents a perfect fit. While no "rules-of-thumb" have been established for target CRB or NRMSE, improvements to these values were sought throughout the system identification process.

3.4 Data Collection

Successfully identifying a model depends heavily on well-executed data collection. In the case of full-scale aircraft, this process can prove quite difficult: the number of experiments is often limited by budget, outdoor testing conditions may include gusts that disturb the vehicle and obscure the response, there may be certain

states of the vehicle that are difficult to measure, and the data may be corrupted by sensor noise. However, in the case of the micro-helicopters, data collection was performed in a laboratory environment without any disturbances (i.e., air conditioners or building drafts). Vicon provided accurate, minimal-noise measurements of almost all the vehicle states. And because of the light-weight, robust structure of the helicopters, little damage incurred when control was lost, giving some room to experiment with the types and amplitudes of input signals.

There are two main design considerations to the data collection process: 1) exciting the vehicle dynamics with appropriate inputs and 2) recording and processing the inputs and the vehicle response. These will be discussed in the following sections.

3.4.1 Vehicle Inputs: Simultaneous, Multi-Sinusoidal Signals

A well-designed input excites the vehicle dynamics over the range of frequencies expected to be most relevant. Common inputs include impulses, frequency sweeps (or "chirps"), and doublets. These inputs may be applied manually by a pilot or may take the form of a pre-generated signal applied through an automatic controller. Generally the inputs are applied to one input channel at a time.

Conventional inputs proved insufficient for the helicopter's highly-coupled dynamics—especially at the beginning of the process when initial parameter guesses were still unrefined. For instance, a lateral chirp input excites both pitch and roll responses. The system identification routine can only identify with high certainty the stabil-

ity derivatives relating to the lateral/pitching motion. However, the quality of the simulation is still dependent on the rolling motion. Until better initial guesses were realized for the longitudinal parameters, the output error algorithm had difficulty converging.

Instead, a method of simultaneous, orthogonal multi-sinusoidal inputs was used. These inputs excited both the lateral and longitudinal dynamics simultaneously, but at different, orthogonal frequencies. Since both longitudinal and lateral dynamics are excited, the output error routine has more information for iterating both longitudinal and lateral parameters. The orthogonality of the inputs ensures no collinearity in the data.

Multi-sinusoidal inputs are signals with wideband frequency content optimized to excite the vehicle over a minimal length of time and with optimized input amplitudes. The signal is constructed by summing several sine waves of varying frequencies together. The phase angle of each component is selected to shift the sinusoids relative to each other, which results in a reduction of the total amplitude of the signal. The following equation is used to construct a multi-sinusoidal signal:

$$\vec{u}_j(\vec{t}) = \sum_{k \in 1,2,\cdots,M} A_k \sin\left(\frac{2\pi k \vec{t}}{T} + \phi_k\right) \quad j = 1, 2, \cdots, m \tag{3.18}$$

where u_j is the signal applied to the jth control channel, k is the index for each frequency component, A is the amplitude of the individual signals, T is the total time length of the signal, t is the time vector, and ϕ is the phase angle of the sinusoidal components. The phase angles for each component are selected through an iterative

method that minimizes the relative peak factor (RPF) of the constructed signal,

$$\mathrm{RPF}(\vec{u}_j) = \frac{[\max(\vec{u}_j) - \min(\vec{u}_j)]/2}{\sqrt{2(\vec{u}_j^{\mathrm{T}}\vec{u}_j)/N}}. \tag{3.19}$$

If more than one channel is to be excited during the data collection, the frequencies of the sinusoidal components for each channel can be staggered to ensure that the input signals are orthogonal. Having orthogonal input signals is essential to ensuring that the output data is not collinear. Collinear data leaves ambiguity as to which parameters contribute to the various components of the output. The function `mkmsswp` in SIDPAC generates orthogonal, phase-optimized, multi-sinusoidal inputs.

For the system identification data collection runs, orthogonal, multi-sinusoidal inputs were generated for the lateral and longitudinal cyclic input channels. The signals were constructed with a frequency range from 0.1 to 4 Hz over a 10 second time interval. Both signals consisted of 40 uniformly distributed frequencies. The amplitude $A_k = 0.01$ was select for all k. This amplitude was strong enough to excite the dynamics visually, but not so strong as to perturb the helicopter outside its linear range of operation. The resulting signals are shown in Fig. 3.2.

The signals were pre-generated in Matlab and implemented in the Labview program used to control the helicopters. During a data collection run, minor stick inputs could still be applied to keep the helicopters from drifting too far from hover. Heading and height control were automated for the experiments for both helicopters. The multi-sinusoidal signals are added to the input commands after all pilot and feedback/stabilizing commands are applied. While a feedback control system may

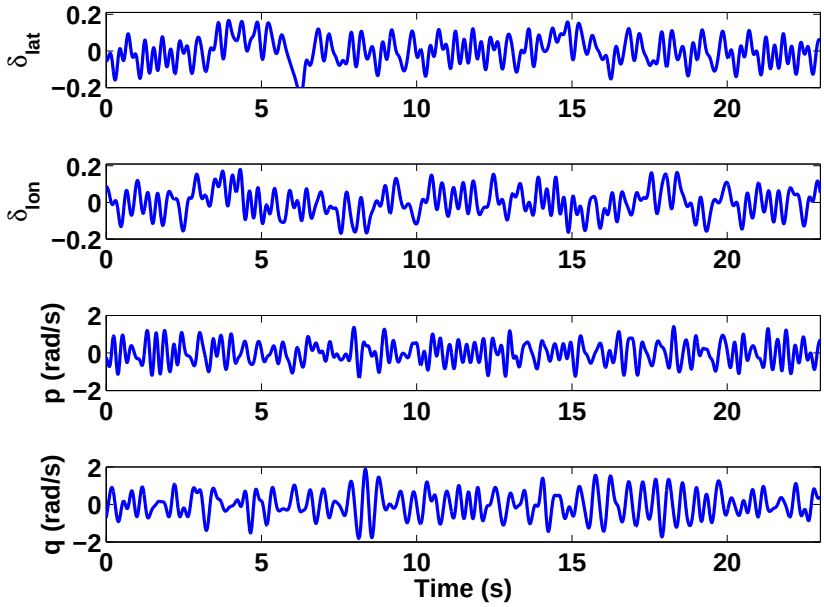

Figure 3.2: Shown here is a time sample of the lateral and longitudinal orthogonal signals used to excite the dynamics of the vehicle during data collection, along with the pitch and roll rate response measured by Vicon. Data for lateral and longitdunal velocities and attitudes (not shown) were also recorded.

cause non-orthogonality in the inputs, according to Klein and Morelli [19], only very high-gain feedback control systems will compromise the modeling results.

3.4.2 Recording Vehicle Inputs and Responses

Given the tools available in the lab, measuring the vehicle response was a fairly straight-forward process. The Labview program described in Section 1.6.1 has the capability of recording all inputs sent to the vehicle mote. Additionally, it can acquire data from Vicon. Vicon has the capability of measuring all states variables (ϕ,θ,p,q,u,v) except the flapping states (a,b) and the flybar states (c,d). The Vicon measurements are very low-noise and require little filtering.

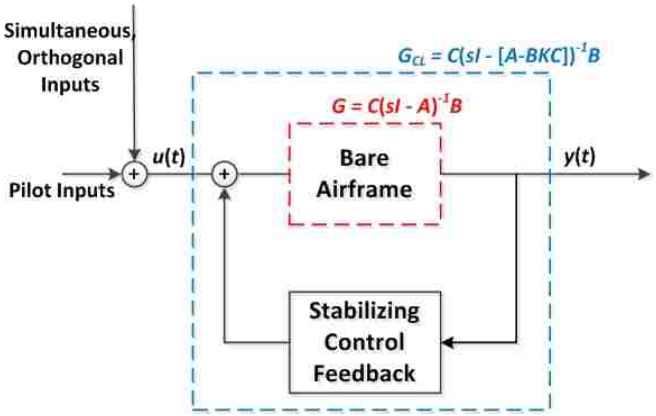

Figure 3.3: Block diagram for closed loop system identification.

In summary, the inputs measured during the data collection were

$$\vec{u} = [\delta_{lat}\ \delta_{lon}]^{\mathrm{T}} \tag{3.20}$$

and the outputs were

$$\vec{z} = [\phi\ \theta\ p\ q\ u\ v]. \tag{3.21}$$

An example of the measured response is provided in Fig. 3.2.

3.5 Closed-Loop Identification of Unstable System

Inner loop feedback was required to stabilize the flybarless helicopter for the data collection flights. Because simulating an unstable system with output error would cause non-convergence in the algorithm, the closed-loop system was identified first. The open loop system was then determined by subtracting the feedback gain from the dynamics matrix. A block diagram depicting the closed loop system is shown in Fig. 3.3. The feedback gain used to stabilize the helicopter was

$$K = \begin{bmatrix} .5 & 0 & 0 & 0 & 0 & 0 \\ 0 & .5 & 0 & 0 & 0 & 0 \end{bmatrix}. \tag{3.22}$$

The closed loop dynamics matrix A_{cl} is

$$A_{cl} = A - BKC. \tag{3.23}$$

The open loop dynamics matrix, then, is given by

$$A = A_{cl} + BKC. \tag{3.24}$$

The B and C matrix remain the same for both the closed loop and open loop systems.

3.6 Lumped Flybar Model

After models were finalized for the flybarless and flybar model, a reduced-order flybar model was also explored. The flybar states c and d were removed, and stability derivatives that effectively model attitude feedback were added: A_ϕ, A_θ, B_ϕ, and B_θ. An examination of eqn. (2.67) shows that attitude feedback occurs if the flybar damping $C_R = 0$. Essentially this means that the flybar is always rotating in a plane parallel to the inertial x-y plane.

The reduced order model took the form,

$$\begin{bmatrix} \dot{\phi} \\ \dot{\theta} \\ \dot{p} \\ \dot{q} \\ \dot{a} \\ \dot{b} \\ \dot{u} \\ \dot{v} \end{bmatrix} = \begin{bmatrix} 0 & 0 & 1 & 0 & 0 & 0 & 0 & 0 \\ 0 & 0 & 0 & 1 & 0 & 0 & 0 & 0 \\ 0 & 0 & 0 & 0 & 0 & L_b & L_u & L_v \\ 0 & 0 & 0 & 0 & M_a & 0 & M_u & M_v \\ A_\phi & A_\theta & 0 & -1 & -\frac{1}{\tau_f} & \frac{A_b}{\tau_f} & 0 & 0 \\ B_\phi & B_\theta & -1 & 0 & \frac{B_a}{\tau_f} & -\frac{1}{\tau_f} & 0 & 0 \\ 0 & -g & 0 & 0 & g & 0 & X_u & 0 \\ g & 0 & 0 & 0 & 0 & g & 0 & Y_v \end{bmatrix} \begin{bmatrix} \phi \\ \theta \\ p \\ q \\ a \\ b \\ u \\ v \end{bmatrix} + \begin{bmatrix} 0 & 0 \\ 0 & 0 \\ 0 & 0 \\ 0 & 0 \\ A_{lat} & A_{lon} \\ B_{lat} & B_{lon} \\ 0 & 0 \\ 0 & 0 \end{bmatrix} \begin{bmatrix} \delta_{lat} \\ \delta_{lon} \end{bmatrix} \tag{3.25}$$

.

For the system identification process, only the parameters having to do with the lumped flapping-flybar dynamics were free: τ_f, A_b, B_a, A_ϕ, A_θ, B_ϕ, and B_θ. Fixing τ_f, A_b, and B_a would have modeled pure attitude feedback; however, these flapping terms were also freed to allow more flexibility. The aerodynamic stability derivatives, L_b, M_a, and the control derivatives were fixed with the values found for the full-scale models.

3.7 Results

The output error algorithm was run for three sets of data, each approximately 20 seconds in length, for both the flybar helicopter and the flybarless helicopter. The same initial parameter guesses were used for each run. The resulting parameters were averaged and used for the final model. The averaged model stability and

control derivatives are listed in Table 3.1, along with the ranges of CRB for each parameter estimate. For each run, the simulated model output was plotted with the collected data to visually verify that the model accurately depicts the measured response. A set of verifications from each helicopter are shown in Fig. 3.4. The ranges of NRMSE, which is the measure of how well the simulations match the data, are provided in Table 3.2.

Overall, the Cramer-Rao lower bounds indicate that the parameters are estimated with reasonably high confidence. The CRBs tend to be higher for the aerodynamic derivatives (i.e., M_u and L_v); however, the agreement of these derivatives between the two models provides a cross-check for the estimates. One major exception is the estimate for L_b. This parameter was the most difficult to identify, as it changed most dramatically depending on how other parameters were fixed or the initial guesses given to the parameters. The final value determined for the parameter is in agreement with the flybar results, and provides the best NRMSE results, given the values of the other parameters in the model. Additionally, the value selected provides agreement between the flybar and flybarless eigenstructure, which will be explored in the next chapter.

The identified parameters for the lumped flapping-flybar model are shown in Table 3.3 and the NRMSE range is provided in Table 3.4. While the parameters were identified with high confidence (indicated by the low CRBs), the NRMSEs show degredation in the accuracy of the model. For this reason, the lumped flapping-flybar model is not examined further.

An additional measure was taken to verify the results for the flybar helicopter.

System identification of the flybar helicopter was originally attempted in the frequency domain using the program CIFER (Comprehensive Identification from FrEquency Responses) developed by NASA Ames [14]. CIFER converts frequency sweep input and output data from the time domain into the frequency domain. It then estimates the parameters based on matching the frequency responses of the state space model to the frequency responses of the collected data. While parameter estimation using this program proved difficult, due to the challenges inherent to the coupled dynamics, the frequency responses calculated from the frequency sweeps could still be compared to the frequency responses of the flybar model. These comparisons, provided in Fig. 3.5, show agreement between the model and data in the frequency domain.

3.8 Summary

In this chapter, the process of system identification, and the associated challenges, were explored. The model here was assembled in phases, starting with the decoupled flapping states and control derivatives and concluding with the identification of aerodynamic stability derivatives. The flybarless helicopter was not open loop stable and required a small feedback gain to stabilize for the data collection flights. The open loop system was calculated based on the identification of the closed loop system. The coupled nature of the helicopter dynamics increased the difficulty of identifying an accurate model. Using simultaneous multi-sinusoidal inputs enabled the output error algorithm to simultaneously iterate parameters responsible

	Flybarless		Flybar	
Parameter	$\hat{\theta}$	CRB %	$\hat{\theta}$	CRB %
A-Matrix				
L_b	930	170–190	957	54–120
M_a	310	18.4–34	302	17–23
A_b	-0.908	0.77–1.3	0.152	4.3–13
B_a	0.600	1.3–2.2	0.113	1.7–4.1
A_c, B_d	–	–	-0.788	0.11-0.12
A_d, -B_c	–	–	-0.484	0.79–2.5
L_u	-15.9	71–106	-23.5	47–48
L_v	-26.7	17–30	-27.2	6.7–56
M_u	7.42	16–29	12.0	7.9–38
M_v	-3.20	27–36	-5.731	14-17
X_u	-0.715	3.1–12.2	-0.459	1.7–6.1
X_v	0.366	3.8–15	0.228	1.5–8.3
Y_u	0	–	0	–
Y_v	-0.501	3.6–10	-0.935	0.70–3.9
τ_{sb}	–	–	0.301	3.1–9.1
τ_f	0.049	0.01	0.049	0.01
X_a,X_θ	-9.8	–	-9.8	–
Y_b,Y_ϕ	9.8	–	9.8	–
B-Matrix				
A_{lat}	2.29	2.0–3.9	5.16	2.5–2.6
A_{lon}	4.86	0.71–1.7	8.09	0.96–1.7
B_{lat}	5.41	3.5–4.8	6.85	0.82–1.9
B_{lon}	-2.76	11–19	-3.57	3.0–6.1

Table 3.1: Identified Stability and Control Derivatives

	Flybarless	Flybar
Measured State	NRMSE (%)	NRMSE (%)
ϕ	50.4–61.9	64.2–67.7
θ	51.7–60.4	59.4–60.4
p	39.1–45.8	55.9–63.2
q	61.7–65.7	58.9–64.2
u	51.4–60.9	46.8–73.0
v	57.5–65.9	56.0–85.4

Table 3.2: NRMSE of Time-Domain Verifications

	Flapping-Flybar Lumped	
Parameter	$\hat{\theta}$	CRB %
A_ϕ	-2.7	0.23–0.30
A_θ	-6.7	0.05–0.14
B_ϕ	-5.9	0.09–0.48
B_θ	1.5	1.0–1.9
A_b	0.15	6.8–11.2
B_a	0.038	1.1–4.3
τ_f	0.065	0.03–0.05

Table 3.3: Flapping-Flybar Lumped Model Estimated Parameters

Measured State	NRMSE (%)
ϕ	49.3–57.1
θ	44.3–51.3
p	51.7–59.3
q	51.4–59.9
u	23.9 – 44.0
v	28.1 – 52.0

Table 3.4: Flapping-Flybar Lumped Model NRMSE

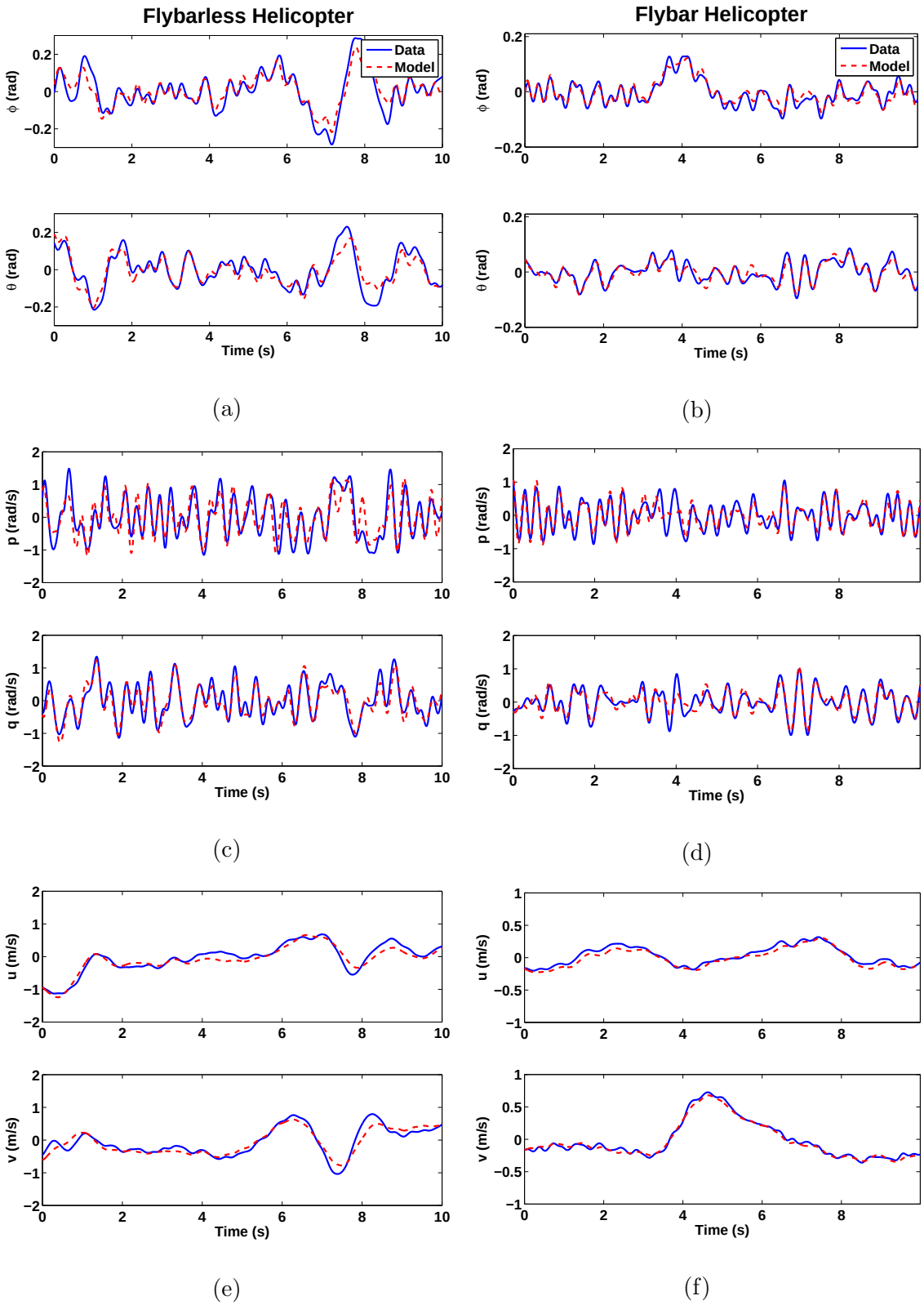

Figure 3.4: Model verifications for the flybarless helicopter are shown in subfigures (a),(c), and (e). Verifications for the flybar helicopter are shown in subfigures (b), (d), and (f).

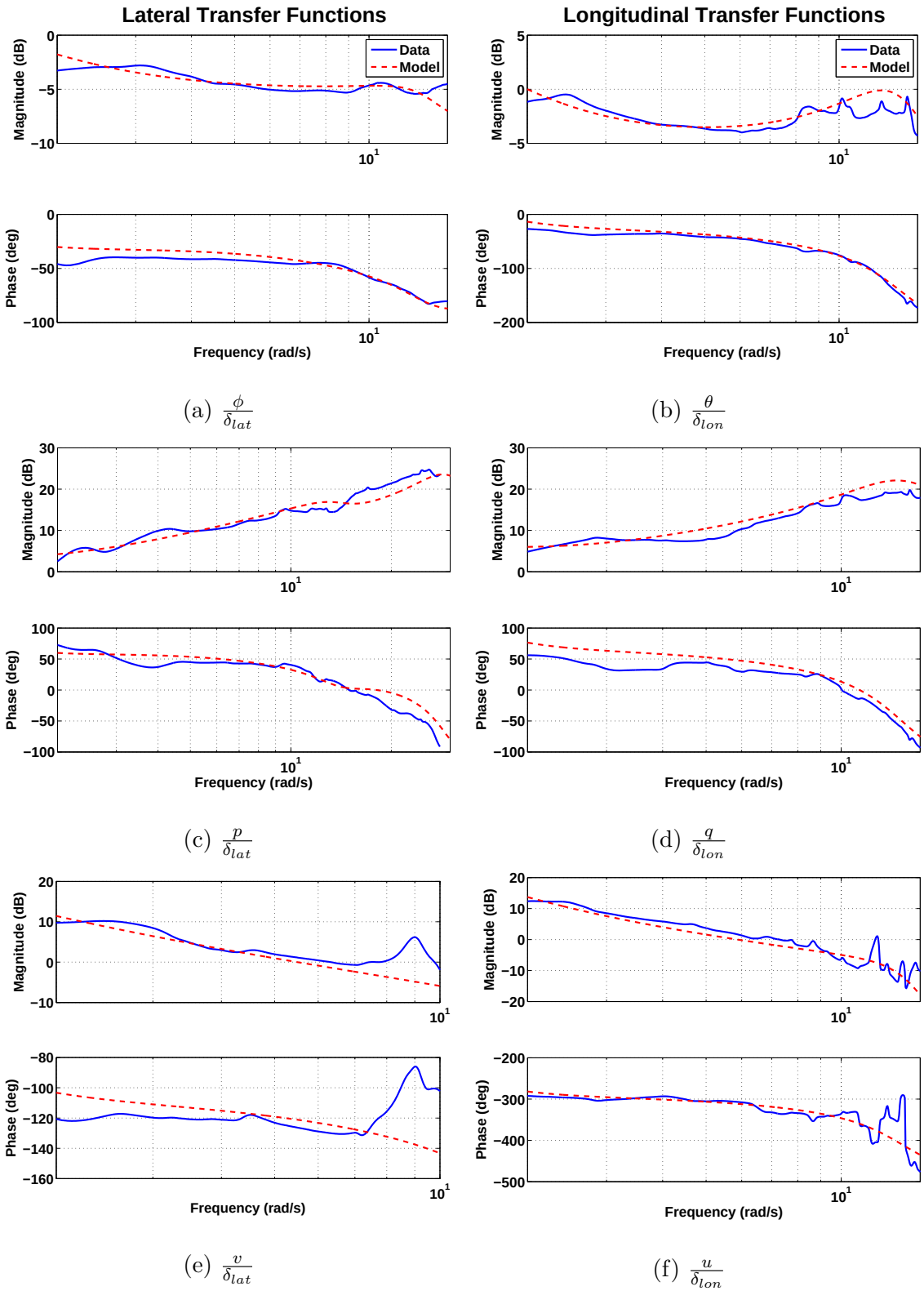

(a) $\frac{\phi}{\delta_{lat}}$ (b) $\frac{\theta}{\delta_{lon}}$

(c) $\frac{p}{\delta_{lat}}$ (d) $\frac{q}{\delta_{lon}}$

(e) $\frac{v}{\delta_{lat}}$ (f) $\frac{u}{\delta_{lon}}$

Figure 3.5: Transfer function verifications for the flybar helicopter. Lateral:(a),(c), and (e). Longitudinal: (b), (d), and (f).

for the lateral and longitudinal inputs without creating collinearity in the data. The final models identified for the flybar and flybarless system show good agreement in the time-domain with the collected output data. The flybar model was also verified with frequency-domain data. Additionally, a lumped flybar-flapping model was identified, but proved inferior to the full-state flybar model.

Chapter 4

Modal Analysis

4.1 Overview

Because the models found in Chapter 3 are based off a physical understanding of the system, conjectures can be made about the system based on the magnitudes and signs of the stability derivatives. For instance, because $L_b > M_a$, one could assert that the rolling dynamics are much quicker than the pitching dynamics—and this assertion can be supported by the relative inertias, $I_{xx} < I_{yy}$. However, these observations are limited and can be obscured by the coupling of states throughout the matrix.

Linear system theory offers several tools for analyzing and understanding a system beyond making simple observations from the state matrix. The eigenstructure of a system reveals the strength and direction of the vehicle's natural motion. In this chapter, comparisons are made between the eigenstructures of the flybar and flybarless helicopters. The influence of the flybar on the modal directions and damping is also assessed. With this analysis, conclusions can be made about how the flybar impacts the handling of the system.

4.2 Eigenstructure Analysis

The response of a linear system can be expressed as a linear combination of its modes [20, 21]. By this definition, if the vehicle is perturbed in the direction of a mode, its response will continue in that exact direction. The directions of the system modes are determined by the eigenvectors $\vec{v}$ of the state space matrix A. The strength of this response is determined by the eigenvalues λ of A. An eigenvalue with an imaginary component indicates that the the mode is oscillatory, whereas a real eigenvalue indicates a mode that is fully damped. A mode with a positive real eigenvalue is unstable. The eigenvalues and eigenvectors are determined from the equation set,

$$\det[\lambda I - A] = 0 \tag{4.1}$$

$$A\vec{v} = \lambda\vec{v}. \tag{4.2}$$

The eigenvalues of the system, synonymous with the system poles, are plotted in Fig. 4.1. In addition to system poles, the flybar also has a zero pair, which is also plotted. The effects of the zero pair will be discussed later in the chapter. The flybarless helicopter has four eigenvalue pairs: two fast pairs that are heavily damped, one slow pair which is lightly damped and stable, and another slow pair which is unstable. The flybar helicopter shows a similar trend, except the heavily damped modes are closer to the imaginary axis and the two slow pairs are both stable. The flybar helicopter also has an additional, almost critically-damped, pair.

The eigenvectors, plotted in Fig. 4.2 and Fig. 4.3, provide insight into the directions of these modes. The flybarless helicopter's lightly damped modes are

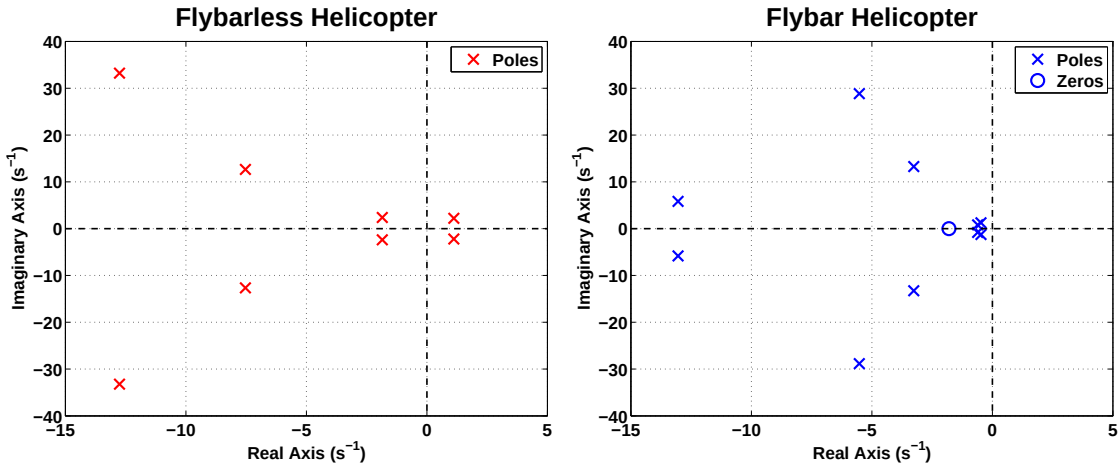

Figure 4.1: The helicopters share similar eigenvalue locations. The flybar helicopter has an extra, almost critically-damped, eigenvalue pair and a zero.

both in the rotational rate directions. The first mode is in the lateral direction and is dependent on the flapping states (not portrayed here, because the lengths were insignificant). The second mode is coupled between the lateral and longitudinal directions and, while dependent on the flapping states as well, shows coupling with all states (again, not portrayed). The unstable mode and the long-period mode are both dominated by translational velocity states, with strong contributions from the rotational states. The flybar helicopter, on the other hand, shows a decoupling of the dynamics. The first two modes are lateral and longitudinal flapping modes. The longitudinal mode has a stronger contribution from the p state, due to the smaller I_{xx} inertia. The short-period modes are dominated by decoupled translational dynamics. The critically-damped mode is coupled between the lateral-longitudinal rotational rates. A summary of the modes is provided in Table 4.1—the modes are numbered here for reference later in the chapter.

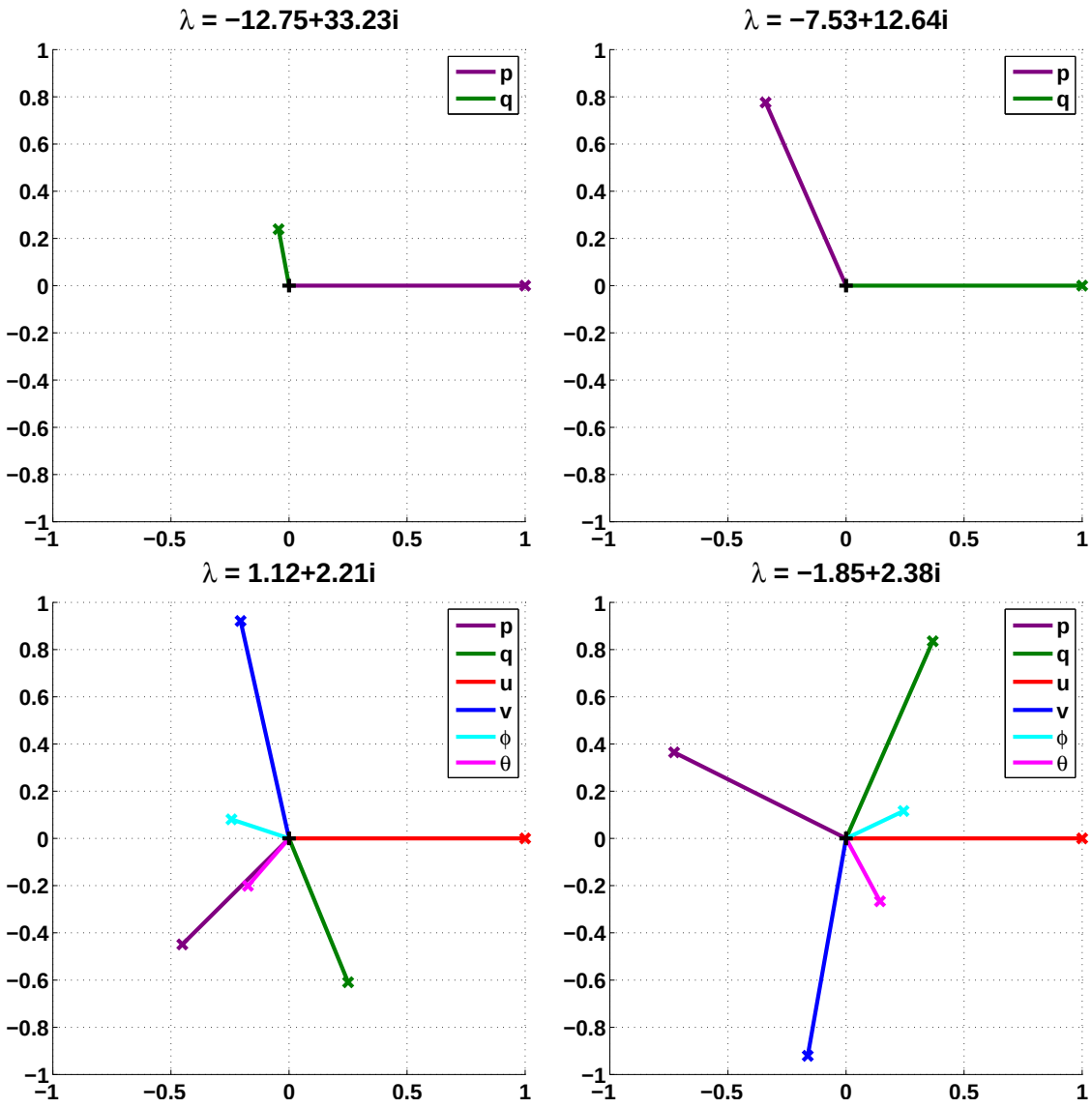

Figure 4.2: Eigenvectors for flybarless helicopter.

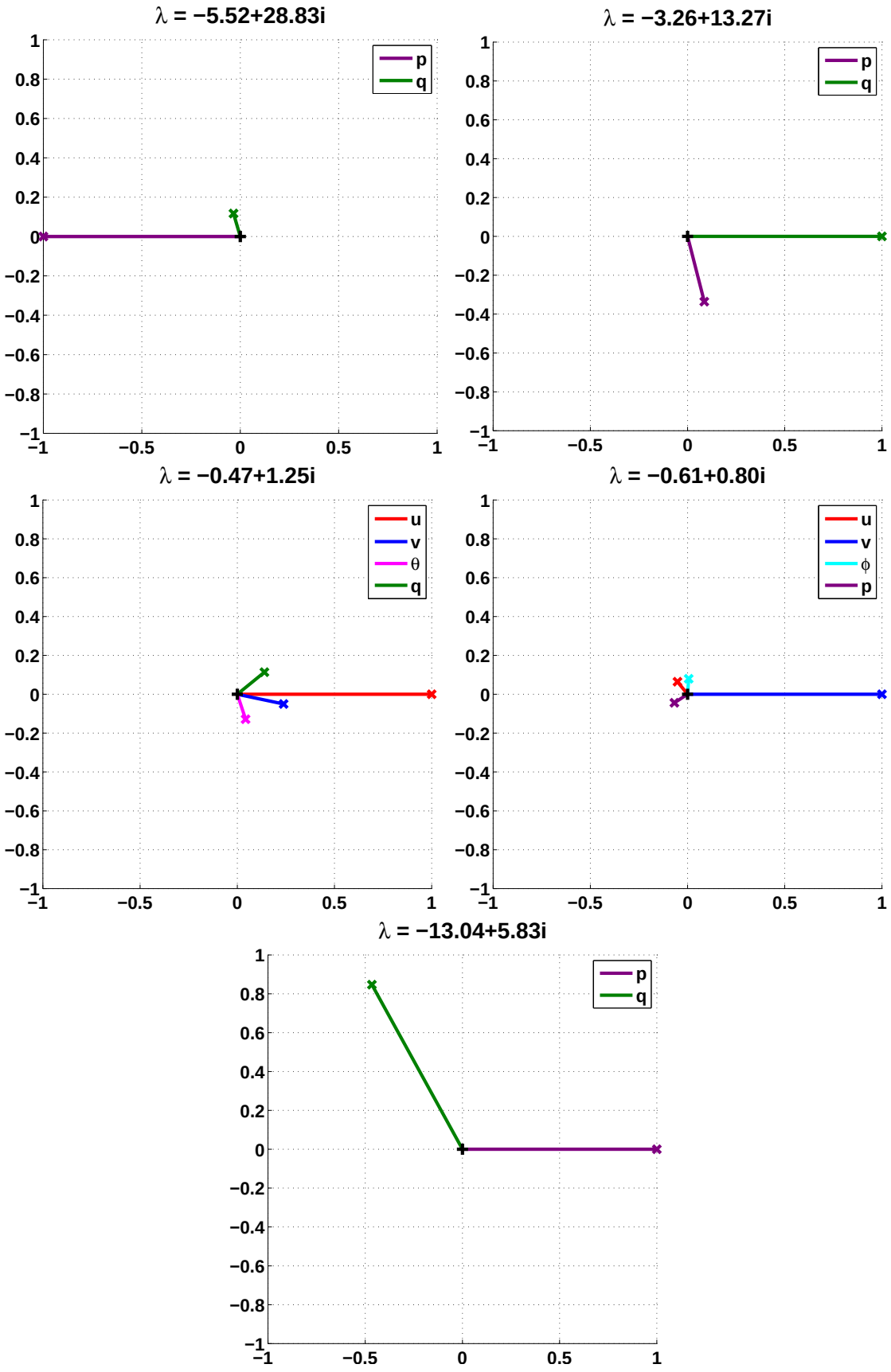

Figure 4.3: Eigenvectors for flybar helicopter.

Mode No.	Eigenvalue	Damping	Frequency (rad/s)	Direction	Eigenvector States
			Flybarless Helicopter		
1	$-12.8 \pm 33.2j$	0.36	35.6	lateral,	p (74%), q (18%)
2	$-7.53 \pm 12.6j$	0.51	14.7	coupled,	p (40%), q (47%)
3	$1.12 \pm 2.21j$	-0.45	2.48	coupled,	p (17%), q (17%), u (26%), v (25%)
4	$-1.85 \pm 2.38j$	0.61	3.02	coupled,	p (19%), q (21%), u (23%), v (22%)
			Flybar Helicopter		
1	$-5.52 \pm 28.8j$	0.19	29.4	lateral,	p (81%), q (10%)
2	$-3.26 \pm 13.3j$	0.24	13.7	longitudinal,	p (22%), q (63%)
3	$-0.47 \pm 1.25j$	0.35	1.33	longitudinal,	u (57%), v (14%), θ (7.6%), q (10%)
4	$-0.61 \pm 0.80j$	0.61	1.00	lateral,	u (6.2%), v (74%), ϕ (6.0%), p (6.0%)
5	$-13.0 \pm 5.83j$	0.91	14.3	coupled,	p (42%), q (41%)

Table 4.1: Summary of Helicopter Modes

4.2.1 Effects of Flybar Inertia on Eigenstructure

At this point in the analysis, some simple conclusions can be drawn about the effects of the flybar. Most significantly, the flybar stabilizes the system. Without the flybar, the helicopter is extremely difficult to fly due to the unstable third mode in the flybarless system. Additionally, the flybar decouples the modes of the system. This also provides handling improvements, as the pilot can assume a lateral input will produce a generally lateral response. Lastly, the flybarless helicopter appears to have added stiffening and damping in the flapping modes.

However, it is still difficult to determine whether these effects are due to the slight differences in the helicopter models. Specifically, the flybarless helicopter is equipped with a slightly heavier, stiffer main rotor. The rotor differences may affect both the aerodynamic and the flapping stability derivatives. The servos on the flybarless helicopter are also positioned closer together, decreasing the I_{xx} inertia.

To investigate this point further, the effects of decreasing the flybar inertia

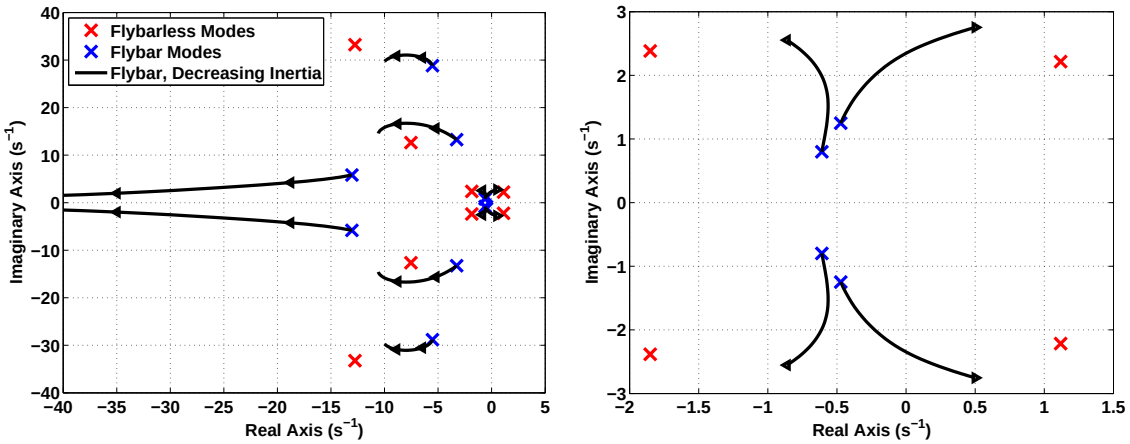

(a) All poles

(b) Zoomed view of long-period poles

Figure 4.4: Flybar inertia effects on pole locations.

were examined. From Section 2.5, we note that $\tau_{sb} \propto I_{sb}$:

$$\tau_{sb} = 4\frac{I_{sb}}{C_R}. \tag{4.3}$$

By decreasing the value of τ_{sb} in the state space matrix, the progression of the modes as the flybar inertia decreases can be modeled. For the following analysis, τ_{sb} [entries [7,7] and [8,8] in the A matrix] is multiplied by K_{sb}, where K_{sb} ranges from 0.01 to 1. A pole-zero diagram showing the movement of the modes as the inertia of the flybar decreases is provided in Fig. 4.4. While the diagram does not show perfect agreement between the reduced inertia flybar and the flybarless helicopter, the trend is apparent.

Next, the modes are decomposed into their natural frequencies and damping in Figs. 4.5 and 4.6 to show how these characteristics change with decreased flybar inertia. In each case, except mode 4 damping, the characteristics approach the values of the flybarless helicopter. Modes 1 and 2 only really increase in natural frequency

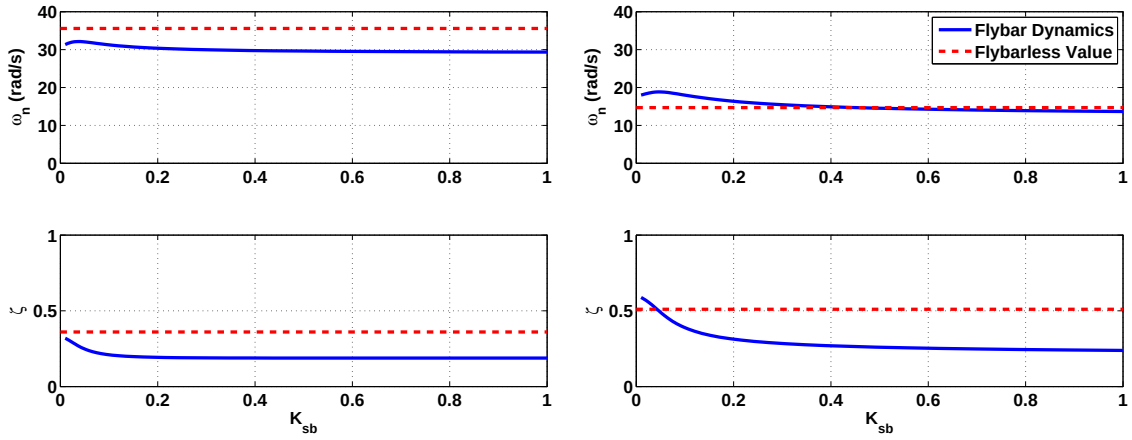

(a) (b)

Figure 4.5: Decreasing the flybar inertia has little effect on modes 1 and 2.

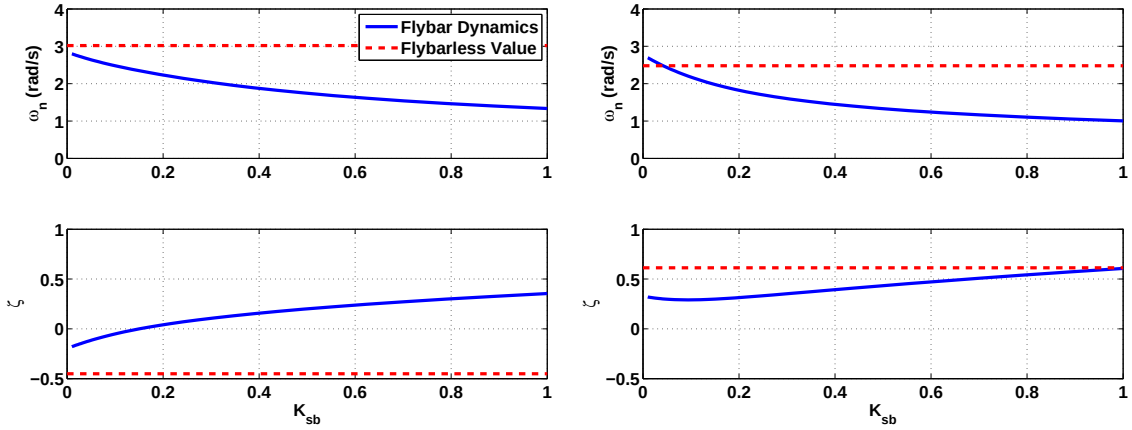

(a) (b)

Figure 4.6: Decreasing the flybar inertia increases the natural frequency and decreasing the damping of modes 3 and 4.

and damping at small values (< 0.2) of K_{sb}. Modes 3 and 4 show gradual increases in natural frequency and decrease in damping as K_{sb} decreases. The helicopter becomes unstable at $K_{sb} \approx 0.15$, which corresponds to a flybar length that is approximately

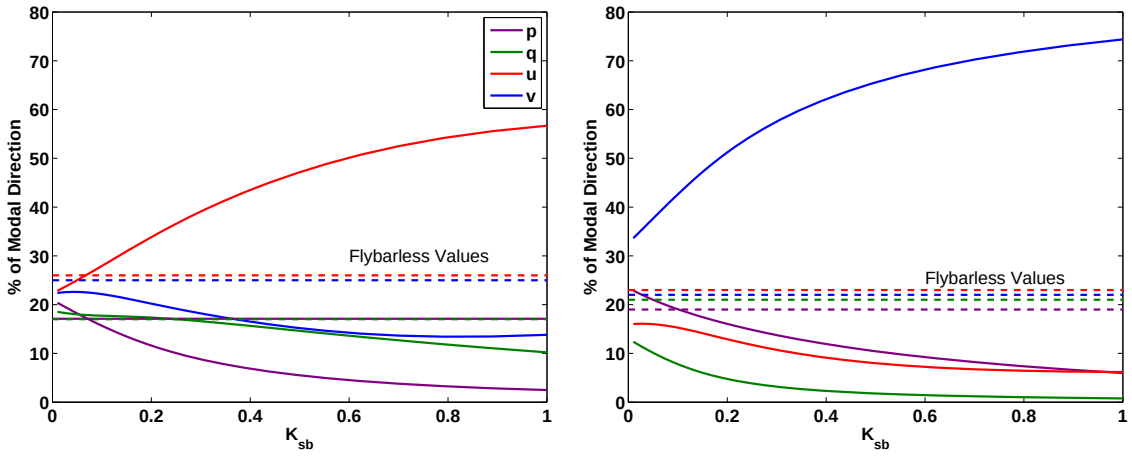

(a) (b)

Figure 4.7: Flybar inertia effects on modes.

40% of the full length.

The trend of the relative magnitudes of eigenvector directions for modes 3 and 4 are shown in Fig. 4.7. As expected, the flybar dynamics become more coupled as the flybar is shortened. This is in agreement with the values of the flybarless helicopter. With a full-inertia flybar, the helicopter has decoupled, moderately-damped, translational dynamics. With a reduced-inertia flybar—or flybarless—these modes are heavily coupled both between longitudinal-lateral states *and* between translational and rotational states. The differences between the directions of modes 1 and 2 are not affected by the flybar and may be attributed to physical differences between the vehicles.

The differences in the vehicle response are clearly seen in the simulated system response to a step input, shown in Fig. 4.8. Two step inputs are compared: one for the helicopter with a full-inertia flybar ($K_{sb} = 1$) and one for a helicopter with a

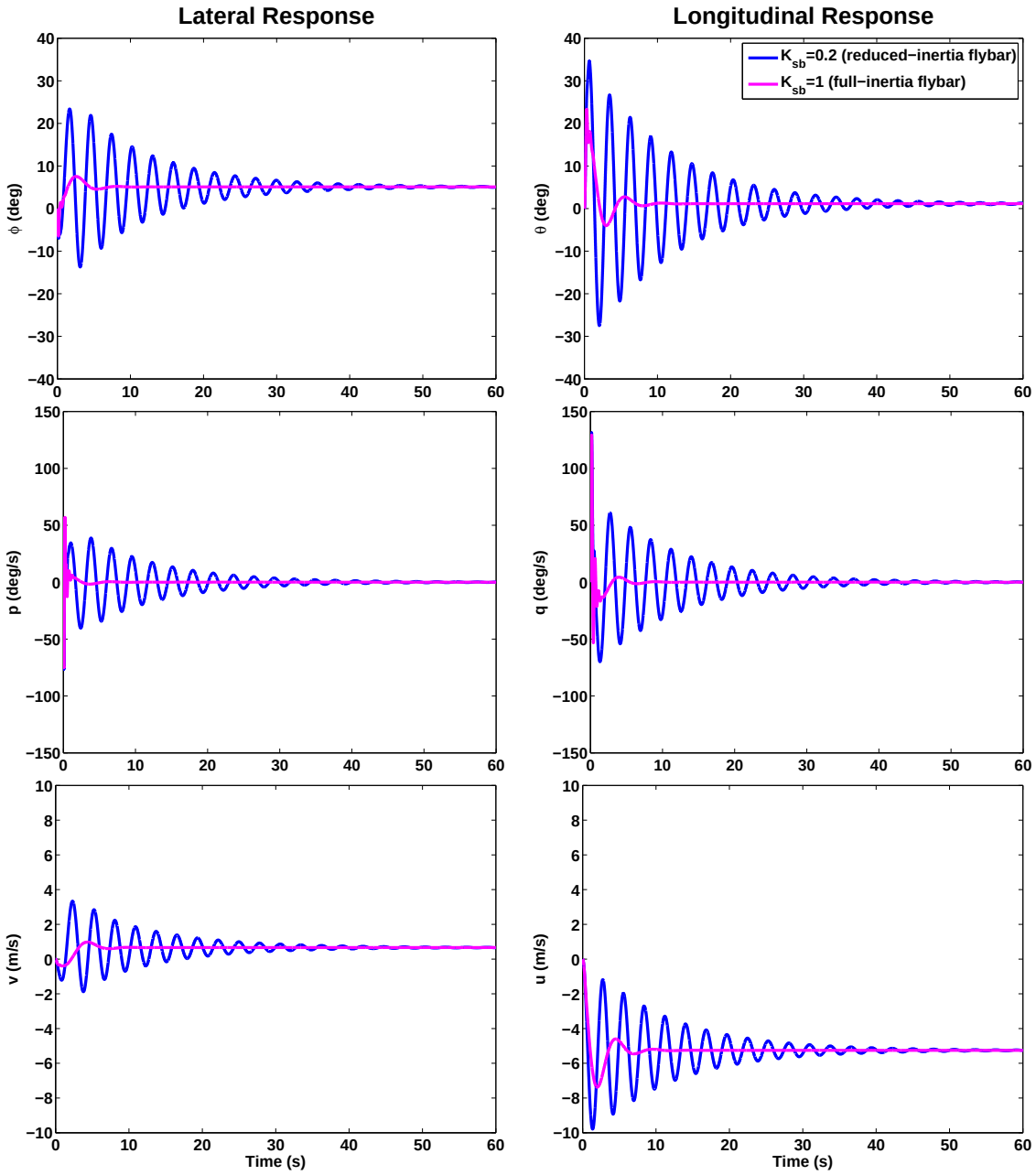

Figure 4.8: The step response shows how a reduced-inertia flybar helicopter has a more coupled response than the full-inertia flybar helicopter. Settling times are also longer for the reduced-inertia flybar.

reduced-inertia flybar ($K_{sb} = 0.2$). This scale of flybar was chosen because it is just larger than the size estimated to maintain stability. The step responses confirm the conclusion drawn from the eigenstructures. The flybar helicopter response is more damped and has less lateral response. The reduced-inertia flybar helicopter is less damped and displays a significant lateral response. The flybar step response has a settling time of approximately 10 seconds, which is low compared to the reduced-inertia flybar helicopter's settling time of approximately 40 seconds.

4.2.2 Effects of Zero on System Dynamics

Zeros are a result of competing dynamics within the system that cause an output of zero despite non-zero inputs [22]. As seen in Fig. 4.1, the flybar mechanism introduces a zero to the system. The zero is located at,

$$z_{sb} = -1.80 \approx \frac{1}{2\tau_{sb}}. \tag{4.4}$$

Because the zero is located close to the other eigenvalues of the system, it was examined whether the zero cancelled the system dynamics at those modes. For MIMO systems, this not a straight-forward observation because the direction of the zeros and poles are just as important as the locations.

For this analysis, the direction of the zeros and poles inputs and outputs are assumed to be unit vectors,

$$\vec{u}_z^H \vec{u}_z = 1; \quad \vec{u}_p^H \vec{u}_p = 1; \quad \vec{y}_z^H \vec{y}_z = 1; \quad \vec{y}_p^H \vec{y}_p = 1. \tag{4.5}$$

The system response to an input at a zero is magnitude zero, and the response at a

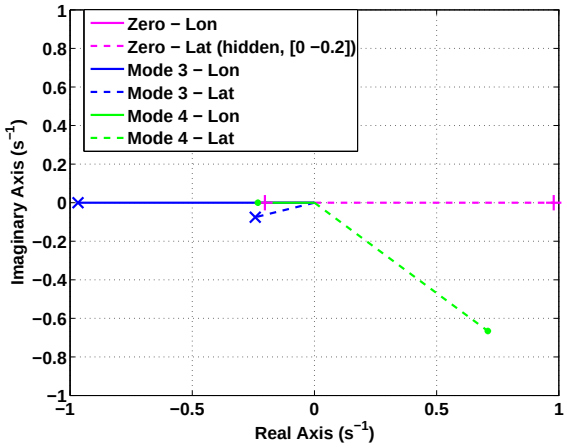

Figure 4.9: While the relative strengths of the zero and mode 4 inputs are similar, the mode 4 input is shifted by $\approx 45°$.

pole is infinite. These relationships are crudely expressed as

$$G(p)\vec{u}_p = \infty \cdot \vec{y}_p \tag{4.6}$$

$$G(z)\vec{u}_z = 0 \cdot \vec{y}_z. \tag{4.7}$$

The input and output directions for poles and zeros may be determined from the singular value decomposition of $G(s) = U\Sigma V^H$ evaluated at $p + \epsilon$ (for very small ϵ) and z. The direction of the pole input is the first column of V, and the direction of the pole output is the first column of Σ. Likewise, the direction of the zero input is the last column of V, and the direction of the zero output is the last column of Σ.

For this particular analysis, the input direction of the poles close to the zero (modes 3 and 4) are compared to the input direction of the zero. A plot of the directions is provided in Fig. 4.9. While the lateral and longitudinal strengths of mode 4 and the zero are similar, the longitudinal input is shifted by a significant phase. As such, it is assumed that the zero does not have a significant effect on

the dynamics of the system. A minimum realization of the system, calculated in Matlab, confirms that no dynamics are cancelled.

An additional observation about the pole is that its location is inversely proportional to τ_{sb}. As the inertia of the flybar decreases, the pole tends toward $-\infty$.

4.3 Conclusions

By looking at the eigenstructures of the flybar and flybarless systems, conclusions can be drawn about the differences in their natural motion. The flybar helicopter is stable and a relatively decoupled system. The flybarless helicopter has an unstable mode and shows high coupling across all of its states. The relationship of the natural frequency and damping of the long-period modes to the flybar inertia can be determined by multiplying the stabilizer bar time constant τ_{sb} by a factor K_{sb}. The natural frequency of the long-period modes increase and the damping decreases as the flybar inertia term diminishes. The helicopter becomes unstable with a flybar approximately 40% of the full length ($K_{sb} \approx 0.15$). Additionally, the progressive increase in coupling between the states was also shown as the flybar inertia term decreased. A simulated step response for the flybar and a reduced-inertia flybar shows how the decreased inertia creates a more coupled, less damped system.

This analysis offers insight into the handling of the helicopters and the effects of adding a flybar. However, a control system can be designed to improve the handling qualities of the flybarless helicopter as needed. To understand the advantages and disadvantages of using a flybar for stabilization, the maneuverability and gust

tolerance of the bare airframe need to be analyzed. The next chapter explores these characteristics.

Chapter 5

Bare Airframe Manueverability and Gust Tolerance

5.1 Overview

In the previous chapter, we gained an understanding for the natural motion of the vehicles and how this relates to control design and pilot handling. The flybar helicopter showed a stable, decoupled response at low frequencies, while the flybarless helicopter was unstable and highly coupled. However, it is difficult to determine from this information the inherent characteristics of the vehicle's bare airframe. Specifically, we are interested in the MAV's potential to maneuver quickly through confined spaces and to stay course when faced with gust disturbances.

This chapter presents a method for comparing the maneuverability and gust tolerance of the flybar and flybarless helicopter using reachability and disturbance sensitivity sets. Conclusions about the maneuverability of a vehicle can be drawn by examining the reachable set of the vehicle for a bounded, unit norm input. For linear models, the reachable set is defined by an ellipsoid whose structure is determined from the controllabilty gramian. Analogously, a disturbance sensitivity ellipsoid can also be calculated to determine the space a vehicle may be perturbed to when subjected to a bounded gust disturbance. Previously, reachability ellipsoids were used to optimize kinematic inputs for a fruit fly (*Drosophila melanogaster*) linear model [2]. Disturbance sensitivity ellipsoids in combination with reachability

ellipsoids were used to assess properties of a closed-loop microquadrotor [3]. This research extends these tools to compare the limits of the bare airframes of the flybar and flybarless helicopter platforms. A bare airframe comparison is important because it reveals the characteristics inherent to the vehicle which would otherwise be obscured by the gain selection of the controller designer.

This chapter first reviews the theoretical background for reachability and presents a method for calculating reachability ellipsoids of unstable linear models. The relationship between reachability and maneuverability is also discussed. The theory is then extended to disturbance sensitivity ellipsoids. The ellipsoids of the flybar and flybarless helicopters are then compared, and conclusions are drawn about the effects of the flybar on the system's maneuverability. Based on the size and direction of the disturbance sensitivity ellipsoids with respect to the reachability ellipsoids, conclusions are also made about the relative gust tolerance of the two vehicles.

5.2 Background Theory

A central problem to control theory is knowing what final states are achievable given the system's initial state x_0 and an appropriate input $u(t)$. The reachable set of the vehicle is those states x_1 which may be achieved. The following section reviews theory for defining the reachable set and presents a method for calculating the controllability gramian for an unstable model. The theory applies to a model of

the form

$$\dot{x}(t) = Ax(t) + Bu(t) \tag{5.1}$$

with vector dimensions $u(t) \in \mathbb{R}^p$ and $x(t) \in \mathbb{R}^n$. (Note, vector arrows will be dropped in this section for simplicity.)

5.2.1 Reachability Gramian

To determine the reachable states, we start with the dynamic response $x(t)$ of the system in eqn (5.1) for an initial condition $x_0 = x(t_0)$ and $t \geq t_0$ is

$$x(t) = e^{A(t-t_0)}x_0 + \int_{t_0}^{t} e^{A(t-\tau)}Bu(\tau)d\tau. \tag{5.2}$$

The system is said to be controllable if there exists a $u(t)$ such that $x(t_1) = x_1$ for any initial state x_0, final time $t_1 > 0$, and final state x_1 [23]. The input which achieves x_1 is given by

$$u(t) = -B^{\mathrm{T}}e^{A^{\mathrm{T}}(t_1-t)}W_c(t_1)^{-1}(e^{A(t_1-t)}x_0 - x_1) \tag{5.3}$$

where

$$W_c(t) = \int_0^t e^{A\tau}BB^{\mathrm{T}}e^{A^{\mathrm{T}}\tau}d\tau. \tag{5.4}$$

For a *stable* system, the controllability gramian is considered for $X_c = W_c(\infty)$,

$$X_c = \int_0^\infty e^{A\tau}BB^{\mathrm{T}}e^{A^{\mathrm{T}}\tau}d\tau \tag{5.5}$$

and is also the solution to the Lyapunov equation

$$AX_c + X_cA^{\mathrm{T}} = -BB^{\mathrm{T}}. \tag{5.6}$$

The system (A, B) is controllable if the controllability gramian is positive definite $(X_c > 0)$.

The controllability operator Ψ maps an input time history $u(t) \in \mathcal{L}_2^p[0, \infty)$ to a final state x. If the initial time is chosen at $t_0 = -\infty$ and the final time at $t_1 = 0$, then eqn (5.2) becomes

$$x(0) = e^{-A\infty}x_0 + \int_{-\infty}^{0} e^{-A\tau}Bu(\tau)d\tau \tag{5.7}$$

and the operator Ψ, which maps the input to final state x_0, is

$$\Psi = \int_{-\infty}^{0} e^{-A\tau}Bu(\tau)d\tau. \tag{5.8}$$

Thus, the reachable set is defined as

$$\{\Psi u : u \in \mathcal{L}_2^p[0, \infty) \text{ and } \|u(t)\| \leq 1\}. \tag{5.9}$$

By solving for the minimum energy input $\|u_{\text{opt}}\|$ to reach x_0, Dullerud and Paganini [23] show that the space reachable by a unit norm input is equivalent to an ellipsoid defined as

$$\mathcal{E}_c = \{X_c^{\frac{1}{2}}x_c : x_c \in \mathbb{R}^n \text{ and } \|u(t)\| \leq 1\}, \tag{5.10}$$

where

$$X_c = \Psi_c\Psi_c^*. \tag{5.11}$$

The lengths and directions of the principal axes of the ellipsoid $\mathcal{E}_c$ are determined from the eigenvalues of $X_c^{\frac{1}{2}}$ and the corresponding orthonormal eigenvectors. We can conclude here that the axes of the ellipsoid with longer lengths represent directions which require less energy to control the vehicle, and in that sense, are

directions which are easier for the vehicle to maneuver. By projecting the ellipsoid onto two-dimensional planes and examining the resulting ellipses, we can visualize the directions in which the vehicle is most maneuverable.

5.2.2 Generalized Gramian

For an unstable system, the integral in eqn (5.5) is unbounded. A generalized definition of the controllability gramian, provided by Zhou, et al [4] is used instead:

$$X_c = \frac{1}{2\pi}\int_{-\infty}^{\infty}(j\omega I - A)^{-1}BB'(-j\omega I - A')^{-1}d\omega. \tag{5.12}$$

The system is controllable for $X_c > 0$. The gramian for a stabilizable system (A, B) is the solution to the Lyapunov equation,

$$(A + BF)X_c + X_c(A + BF)' + BB' = 0 \tag{5.13}$$

where $F = -B'X$, and X is the stabilizing solution to the Riccati equation,

$$XA + A'X - XBB'X = 0. \tag{5.14}$$

The proof employs the co-prime factorization of the system,

$$(sI - A)^{-1}B = NM^{-1} \tag{5.15}$$

where M is inner ($M^*(s) = M^{-1}$) and the co-prime factorization formula defined in [24] is,

$$\begin{bmatrix} M \\ N \end{bmatrix} = \left[\begin{array}{c|c} A + BF & B \\ \hline F & I \\ I & 0 \end{array}\right] \tag{5.16}$$

By definition of the co-prime factor, $A + BF$ is stable. Substituting the co-prime factorization into the general definition of the gramian yields,

$$X_c = \frac{1}{2\pi}\int_{-\infty}^{\infty}(j\omega I - A)^{-1}BB'(-j\omega I - A')^{-1}d\omega \tag{5.17}$$

$$= \frac{1}{2\pi}\int_{-\infty}^{\infty}N(j\omega)N^*(j\omega)d\omega \tag{5.18}$$

$$= \frac{1}{2\pi}\int_{-\infty}^{\infty}(j\omega I - (A+BF))^{-1}BB'(-j\omega I - (A+BF)')^{-1}d\omega. \tag{5.19}$$

Thus, the Lyapunov equation in eqn (5.13) provides a solution for X_c. If A is stable, then $X = 0$; if A is antistable (i.e., $-A$ is stable), then $X_c = X^{-1} > 0$. For a system with only stable poles, eqn (5.13) reduces to the familiar Lyapunov form in eqn (5.6), and as shown in Zhou, the minimum energy interpretation is preserved in the generalized case.

5.2.3 Disturbance Sensitivity Gramian

Disturbances $\vec{d}$ acting on the system can be thought of similarly to control inputs,

$$\dot{\vec{x}} = A\vec{x} + \hat{D}_g\vec{d} \tag{5.20}$$

with $\vec{d} = [d_p\ d_q\ d_u\ d_v]^{\mathrm{T}}$, $\vec{d} \in [-1,\ 1]$. The unscaled disturbance input matrix may consist of the negated aerodynamic stability derivatives of A, as shown by Nelson

[13]. For the flybar helicopter, the matrix is,

$$\hat{D}_g = \begin{bmatrix} 0 & 0 & 0 & 0 \\ 0 & 0 & 0 & 0 \\ 0 & 0 & -L_u & -L_v \\ 0 & 0 & -M_u & -M_v \\ 0 & 1 & 0 & 0 \\ 1 & 0 & 0 & 0 \\ 0 & 0 & 0 & 0 \\ 0 & 0 & 0 & 0 \\ 0 & 0 & -X_u & -X_v \\ 0 & 0 & -Y_u & -Y_v. \end{bmatrix} \tag{5.21}$$

(Rows 7 and 8 are excluded for the flybarless gust matrix.) A set of tools similar to the reachability analysis can be applied to determine the directions in which the vehicle is most sensitive to gust inputs.

The disturbance gramian is defined as,

$$X_d = \frac{1}{2\pi} \int_{-\infty}^{\infty} (j\omega I - A)^{-1} D_g D_g' (-j\omega I - A')^{-1} d\omega. \tag{5.22}$$

The gramian for a stabilizable system (A, D_g) is the solution to the Lyaponav equation,

$$(A + D_g F) X_c + X_c (A + D_g F)' + D_g D_g' = 0 \tag{5.23}$$

where $F = -D_g' X$, and X is the stabilizing solution to the Riccati equation,

$$XA + A'X - X D_g D_g' X = 0. \tag{5.24}$$

The disturbance sensitivity ellipsoid is defined as,

$$\mathcal{E}_d = \{ X_d^{\frac{1}{2}} x_d : x_d \in \mathbb{R}^n \text{ and } \|d(t)\| \leq 1 \} \tag{5.25}$$

where the eigenvalues and eigenvectors of $X_d^{\frac{1}{2}}$ are the length and direction of the ellipsoid's axes. Like the reachability ellipsoid, directions with longer axes are significant in the sense that less disturbance energy is required to push the vehicle in

that direction. Thus, the size and direction of the disturbance sensitivity ellipsoid reveals the directions in which the vehicle is most sensitive to gusts. The system can tolerate a gust if the ellipsoid $\mathcal{E}_d$ is contained in $\mathcal{E}_c$.

5.2.4 Quantifying Ellipsoid Size

One measure of the size of an ellipsoid is the Frobenius norm of $X_c^{\frac{1}{2}}$,

$$\|X_c^{\frac{1}{2}}\|_{\mathrm{F}} = \sqrt{\mathrm{trace}\left[(X_c^{\frac{1}{2}})X_c^{\frac{1}{2}}\right]}. \tag{5.26}$$

This norm is physically interpreted as the summed squares (Euclidean norm) of the ellipsoid axes lengths. We are most interested in comparing the size of the ellipsoids of the rigid body states of the helicopters $(\phi, \theta, p, q, u, v)$ and excluding from the norm flybar and flapping states (a, b, c, d). The projection of the flybar reachability and disturbance hyperellipsoids onto the rigid-body state subspace (also hyperellipsoids) is given by

$$\bar{X}_c = MX_cM^{\mathrm{T}} \quad \text{and} \quad \bar{X}_d = MX_dM^{\mathrm{T}} \tag{5.27}$$

where M is composed of basis vectors for the subspace,

$$M = \begin{bmatrix} 1 & 0 & 0 & 0 & 0 & 0 & 0 & 0 & 0 & 0 \\ 0 & 1 & 0 & 0 & 0 & 0 & 0 & 0 & 0 & 0 \\ 0 & 0 & 1 & 0 & 0 & 0 & 0 & 0 & 0 & 0 \\ 0 & 0 & 0 & 1 & 0 & 0 & 0 & 0 & 0 & 0 \\ 0 & 0 & 0 & 0 & 0 & 0 & 0 & 0 & 1 & 0 \\ 0 & 0 & 0 & 0 & 0 & 0 & 0 & 0 & 0 & 1 \end{bmatrix}. \tag{5.28}$$

The Frobenius norm of the rigid body states is then defined as,

$$\|X_c^{\frac{1}{2}}\|_{\mathrm{F}} = \sqrt{\mathrm{trace}\left[(X_c^{\frac{1}{2}})X_c^{\frac{1}{2}}\right]} \quad \text{and} \quad \|X_d^{\frac{1}{2}}\|_{\mathrm{F}} = \sqrt{\mathrm{trace}\left[(X_d^{\frac{1}{2}})X_d^{\frac{1}{2}}\right]}. \tag{5.29}$$

(The matrix M is the same for the flybarless helicopter, except columns 7 and 8 are excluded.) Note that for an even comparison between vehicles, the Frobenius norm also needs to be scaled by the maximum expected value of the states. The scaling of the Frobenius norm is discussed in the next section.

5.2.5 Model Scaling

Before performing further model analysis, the model is scaled by the maximum inputs and outputs. For system identification, the inputs to the helicopter $\delta_{lat}, \delta_{lon} \in [-1,\ 1]$ reflected commands for the maximum excursion of the servos from trim. If we assumed that the helicopters could employ the full extents of their servos, the analysis in this chapter would reveal that the vehicles could travel at speeds up to 16 m/s or rotate at almost 40 rad/s. It is unreasonable to expect that the helicopters are operating in their linear region at these rates. In fact, experimental flights showed that the vehicle input magnitudes rarely exceeded ± 0.25 while maintaining control. For reachability analysis of the system, these inputs require scaling to the expected minimums and maximums. The vehicle outputs likewise require scaling for applying robust control tools.

For the purpose of scaling the model, the original state space system is represented as

$$\hat{y} = \hat{G}\hat{u} \tag{5.30}$$

$$\hat{G}(s) = \hat{C}(sI - A)^{-1}\hat{B} \tag{5.31}$$

where $\hat{B}$ and $\hat{C}$ are the original, unscaled matrices. Each input requires scaling

by the maximum expected deflection from trim $\hat{u}_{\max}$. The outputs are scaled by the maximum allowable control error $\hat{e}_{\max}$, since minimizing error is usually the objective of robust control. Control error is defined as

$$\vec{e} = \vec{y} - \vec{r} \tag{5.32}$$

where $\vec{r}$ is a reference input. The scaling matrices are diagonal matrices D_u and D_e, with $\hat{u}_{\max}$ and $\hat{e}_{\max}$ for each variable along the diagonals. Based on observations from several flights, the following maximums were chosen:

$$D_u = \text{diag}([0.3\ 0.3]) \tag{5.33}$$

$$D_e = \text{diag}([0.1\text{rad}\ 0.1\text{rad}\ 0.1\text{rad/s}\ 0.1\text{rad/s}\ 1\text{m/s}\ 1\text{m/s}\ ]). \tag{5.34}$$

The scaled variables then become

$$y = D_e^{-1}\hat{y}; \quad u = D_u^{-1}\hat{u}. \tag{5.35}$$

The scaled system G can be calculated by substituting into eqn (5.30),

$$D_e y = \hat{G} D_u u \tag{5.36}$$

$$G = D_e^{-1}\hat{G}D_u \tag{5.37}$$

$$G(s) = D_e^{-1}\hat{C}(sI - A)^{-1}\hat{B}D_u \tag{5.38}$$

$$= C(sI - A)^{-1}B \tag{5.39}$$

with $u \in [-1,\ 1]$ and control goal is to maintain $\|e(t)\| = \|y(t) - r(t)\| \leq 1$.

Because the states represented by the Frobenius norm in eqn (5.27) are on different scales with respect to each other, the Frobenius norm of the ellipsoids is

also scaled. The ellipsoid is scaled by the maximum expected values of the states,

$$D_x = \text{diag}([1.75\text{rad } 1.75\text{rad } 14\text{rad/s } 14\text{rad/s } 8\text{m/s } 8\text{m/s }]). \tag{5.40}$$

The projected, scaled ellipsoids are defined by,

$$\bar{X}_c = D_x^{-1} M X_c (D_x^{-1} M)^{\mathrm{T}} \tag{5.41}$$

$$= D_x^{-1} M X_c M^{\mathrm{T}} D_x^{-1} \tag{5.42}$$

and

$$\bar{X}_d = D_x^{-1} M X_d (D_x^{-1} M)^{\mathrm{T}} \tag{5.43}$$

$$= D_x^{-1} M X_d M^{\mathrm{T}} D_x^{-1}. \tag{5.44}$$

The scaled Frobenius norms of the ellipsoids are,

$$\|\bar{X}_c^{\frac{1}{2}}\|_{\mathrm{F}} = \sqrt{\text{trace}\left[(\bar{X}_c^{\frac{1}{2}})\bar{X}_c^{\frac{1}{2}}\right]} \tag{5.45}$$

and

$$\|\bar{X}_d^{\frac{1}{2}}\|_{\mathrm{F}} = \sqrt{\text{trace}\left[(\bar{X}_d^{\frac{1}{2}})\bar{X}_d^{\frac{1}{2}}\right]}. \tag{5.46}$$

5.3 Maneuverability: Reachability Ellipsoid Comparison

The projections of the reachability ellipsoids are shown in Fig. 5.1. Instead of examining the ellipsoids individually, holistic observations are made about the relative reachability of the vehicles:

- The flybarless helicopter ellipses are significantly larger than the flybar helicopter ellipses. This means that the flybarless helicopter has more reachable states and is, generally, a more maneuverable vehicle.

- The bottom three ellipsoids are the most important for drawing conclusions about directional reachability. The flybarless helicopter shows significantly more reachability in vehicle attitude—and consequently, in the translational velocity. From this we may conclude that the flybar restricts the magnitude of the helicopter's angular motion. The reachability of angular rate states are comparable between the two helicopter.

- Some of the ellipsoids are tilted. Physically, the tilt means that the vehicle has more reachability when both states are non-zero. An obvious application of this is for the pair (v, ϕ). The velocity v of the helicopter can be increased by tilting the rigid body by an angle $\Delta\phi$ past trim. The ellipsoid for pair (u, θ) is tilted the opposite direction, because forward velocity is dependent on a $-\Delta\theta$ of the rigid body. Other tilts are due to aerodynamics and are affected by the values of the aerodynamic stability derivatives (i.e., M_u in the case of the pair (q, u)).

To confirm the hypothesis that the flybar restricts the translational velocity states, ellipsoids for a reduced-inertia flybar helicopter were compared to the flybarless helicopter. The inertia scaling factor $K_{sb} = 0.2$ was chosen for the comparison, as this represents the approximate stability boundary. The ellipsoids are shown in Fig. 5.2. While the ellipsoids for the two helicopters show aerodynamic differences, the gap between the reachability of the translational states is reduced. The reduced-inertia flybar helicopter shows comparable reachability.

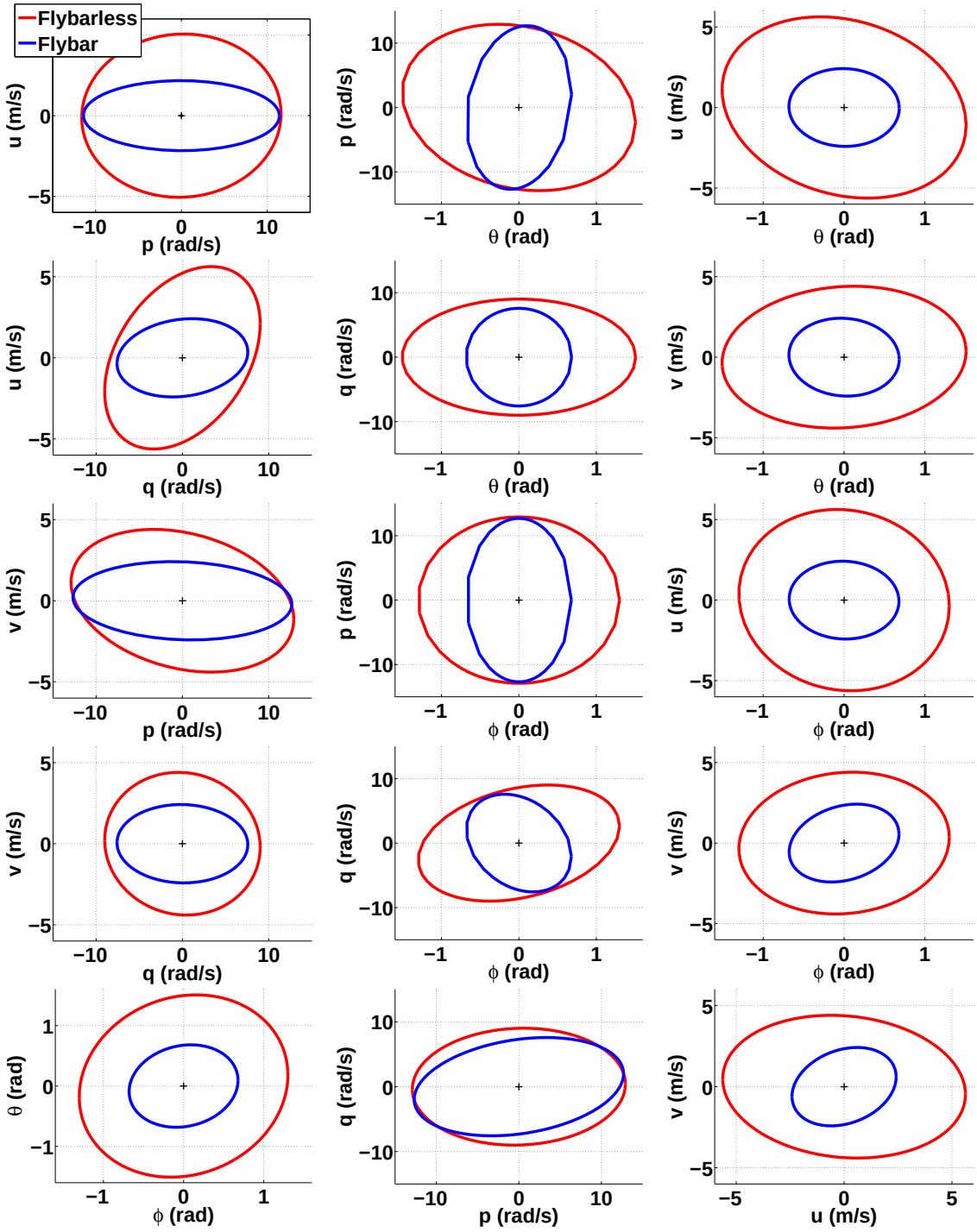

Figure 5.1: A comparison of the reachability ellipsoids shows that the flybarless helicopter has more reachable states than the flybar helicopter. The flybarless helicopter especially has an advantage in translational velocities.

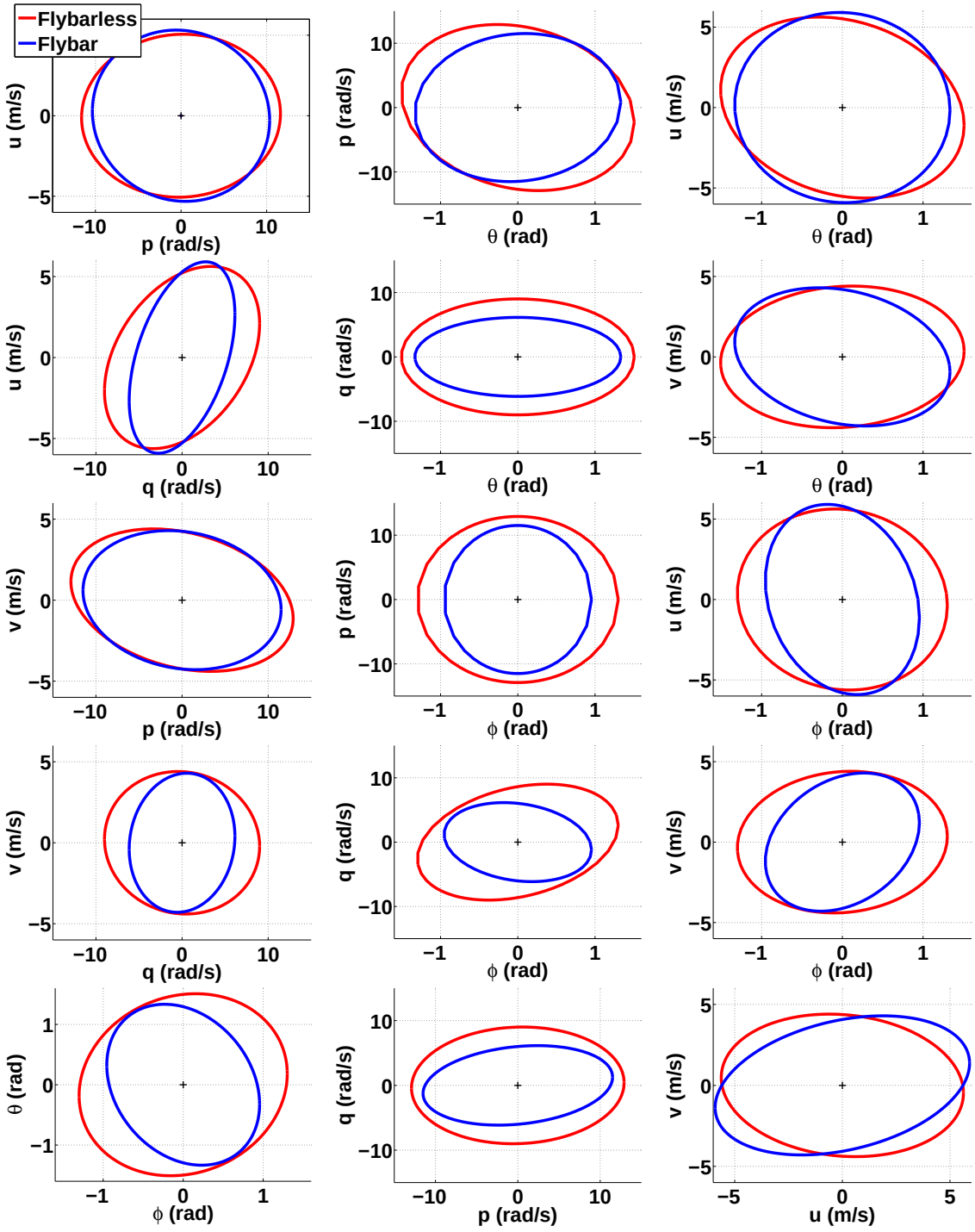

Figure 5.2: By setting $K_{sb} = 0.2$, the reachability of a reduced-inertia flybar can be compared to the flybarless helicopter. The reachability is comparable, even in the translational velocity states.

	Flybarless	Flybar $K_{sb} = 1$	Flybar $K_{sb} = 0.2$
$\|\bar{X}_c^{\frac{1}{2}}\|_{\mathrm{F}}$	1.65	1.14	1.45

Table 5.1: Frobenius Norms of Reachability Ellipsoids

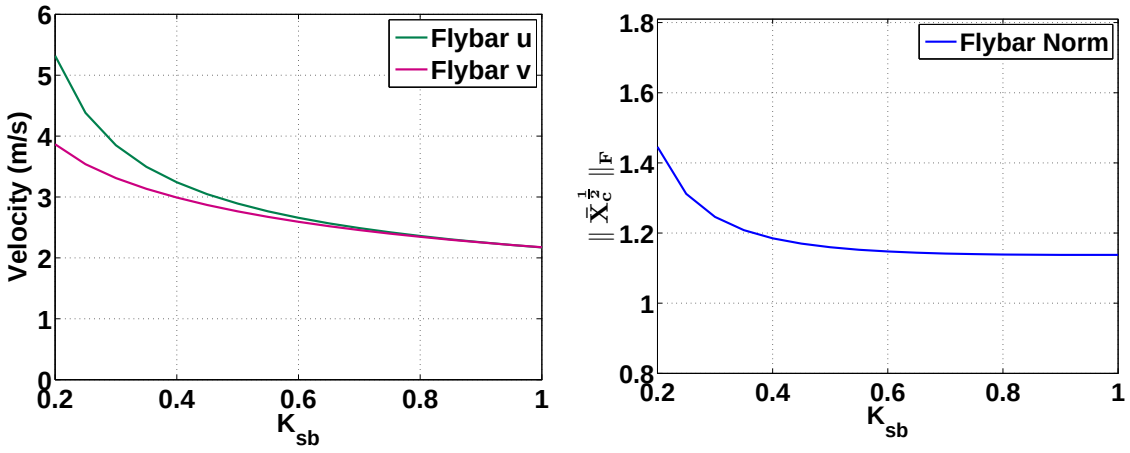

(a) (b)

Figure 5.3: Both a) the reachability of the translational states and b) the Frobenius norm of $X_c^{\frac{1}{2}}$ increase as the inertia (K_{sb}) decreases.

The Frobenius norms for the flybarless, flybar, and reduced-inertia flybar helicopters are shown in Table 5.1. The relative sizes of the ellipsoids are as expected: the flybarless helicopter has the largest norm and the full-inertia flybar the smallest.

Fig. 5.3 shows a) the dependency of translation state reachability on the flybar inertia and b) the increase in overall ellipsoid size as a function of the flybar inertia. Again, the analysis confirms that both values increase as the inertia decreases.

5.4 Gust Tolerance: Disturbance Sensitivity Ellipsoid Comparison

The disturbance sensitivity ellipsoids, similar to the reachability ellipsoids, show which directions the vehicles are most easily perturbed given a unit norm disturbance input. For disturbance sensitivity ellipsoids, though, a vehicle with shorter axes has an advantage, as this shows that the bare airframe is less sensitive to a gust disturbance. The disturbance sensitivity ellipsoids are shown in Fig. 5.4. The following observations are made:

- The flybar helicopter ellipses in the translational velocity and attitude directions show a slight advantage over the flybarless helicopter.
- The flybar actually has a larger ellipsoid in the rotational rate directions, showing that it is more susceptible to gusts in these directions.

From Fig. 5.4, it is not clear which advantages and disadvantages may be attributed to the stabilizer bar and which may be attributed to differences in the rotors, slight differences in the body inertias, or even model error. As in the previous section, disturbance sensitivity ellipsoids for the flybarless helicopter are compared to the reduced inertia flybar helicopter, $K_{sb} = 0.2$. The ellipsoids are shown in Fig. 5.5. The results show an increase in the size of the flybar disturbance sensitivity ellipsoids in the translational velocity and attitude directions. A significant difference is not seen in the rotational rate direction. From this, we can conclude that a flybar with larger inertia results in an airframe that is less sensitive to gust disturbances in the u and v directions. The flybar has little effect on the disturbance sensitivity in the p and q directions.

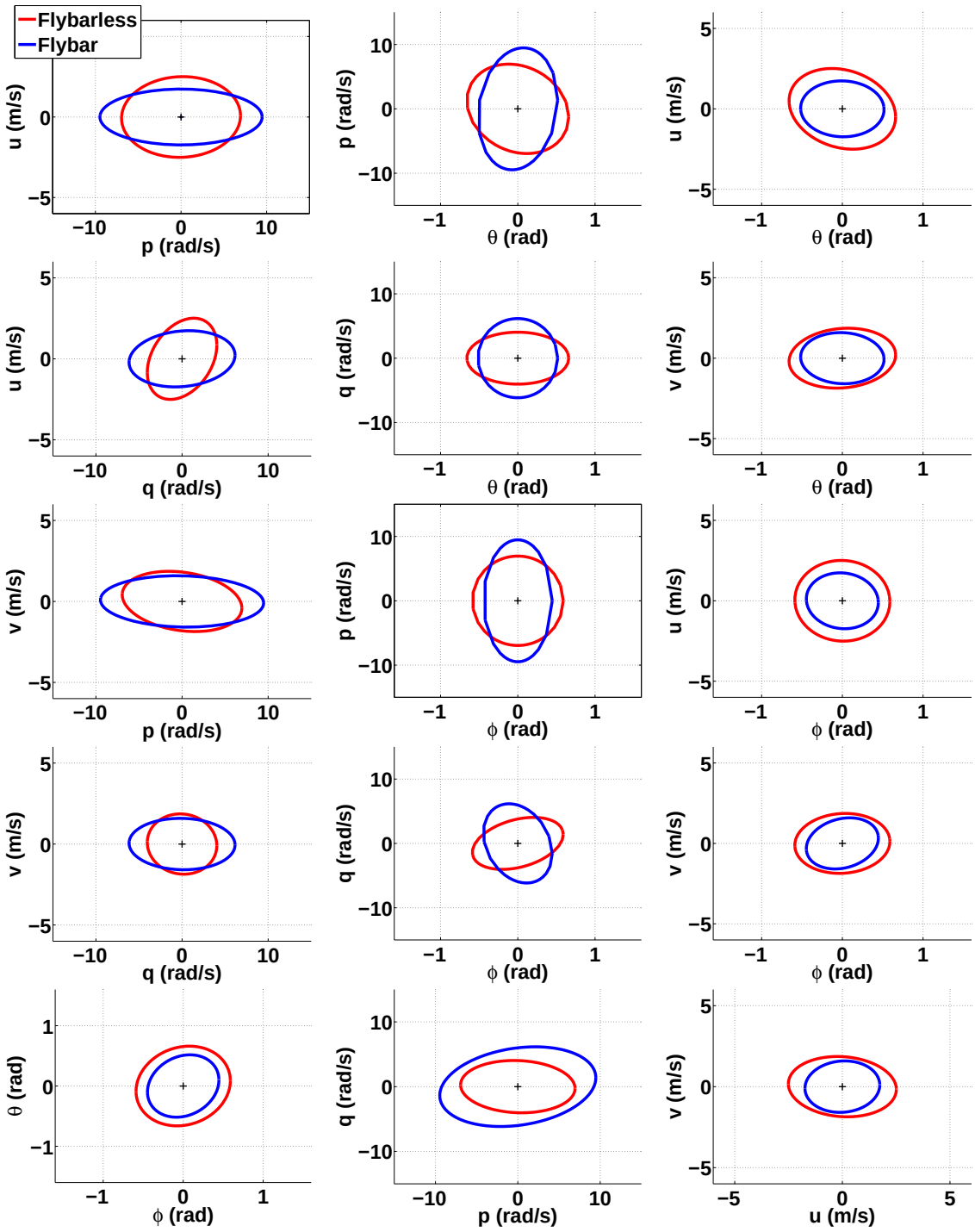

Figure 5.4: A comparison of the disturbance sensitivity ellipsoids shows that the flybar helicopter has a slight disturbance sensitivity advantage compared to the flybarless helicopter in the attitude and translational velocity directions. The flybarless helicopter has a more significant advantage in the rotational rate directions.

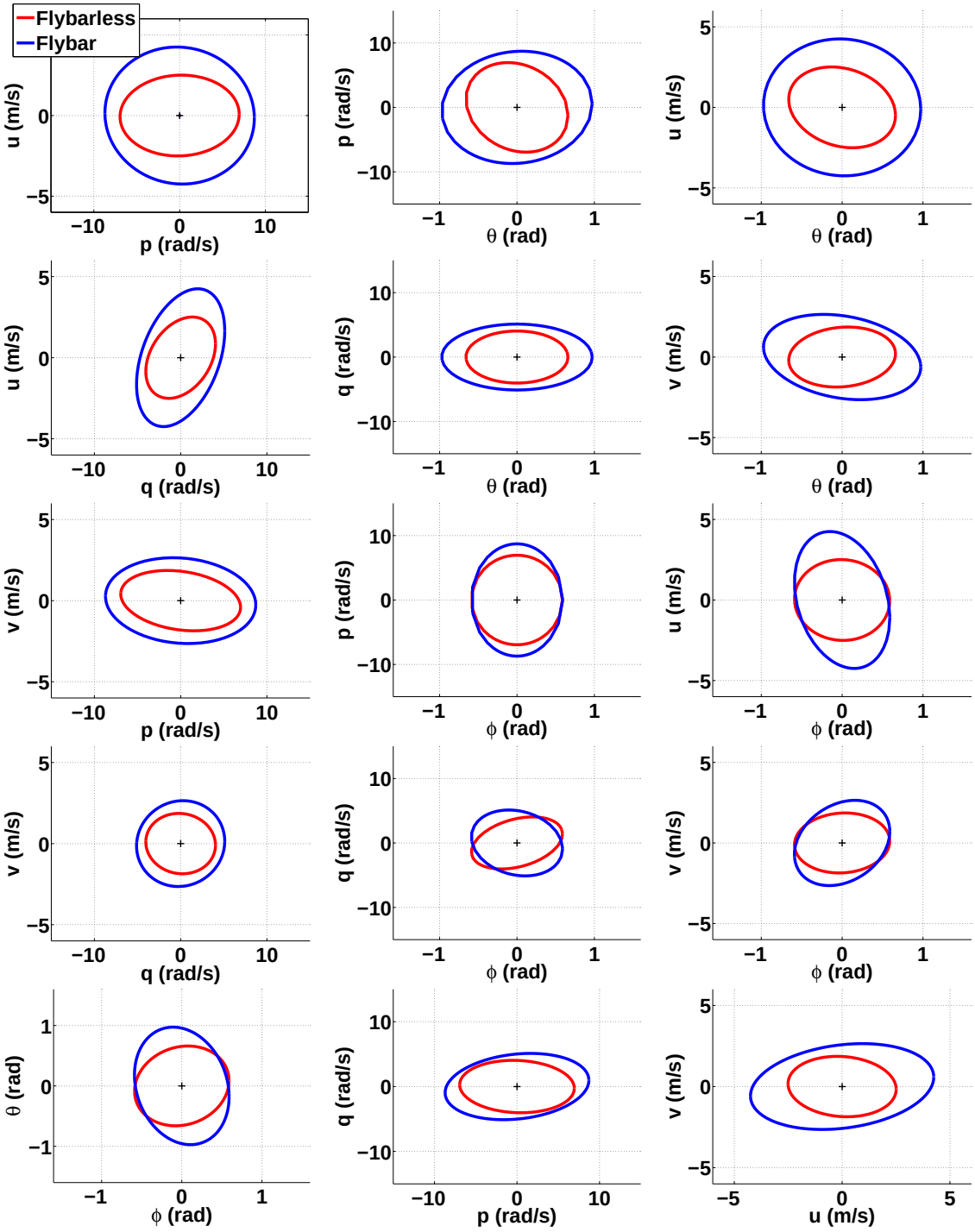

Figure 5.5: By setting $K_{sb} = 0.2$, the disturbance sensitivity of a reduced-inertia flybar can be compared to the flybarless helicopter. The disturbance sensitivity in the attitude and translational velocity directions increases significantly. Disturbance sensitivity in the rotational rate states have little change.

	Flybarless	Flybar $K_{sb} = 1$	Flybar $K_{sb} = 0.2$
$\|\bar{X}_d^{\frac{1}{2}}\|_{\mathrm{F}}$	0.86	0.94	1.15

Table 5.2: Frobenius Norms of Disturbance Sensitivity Ellipsoids

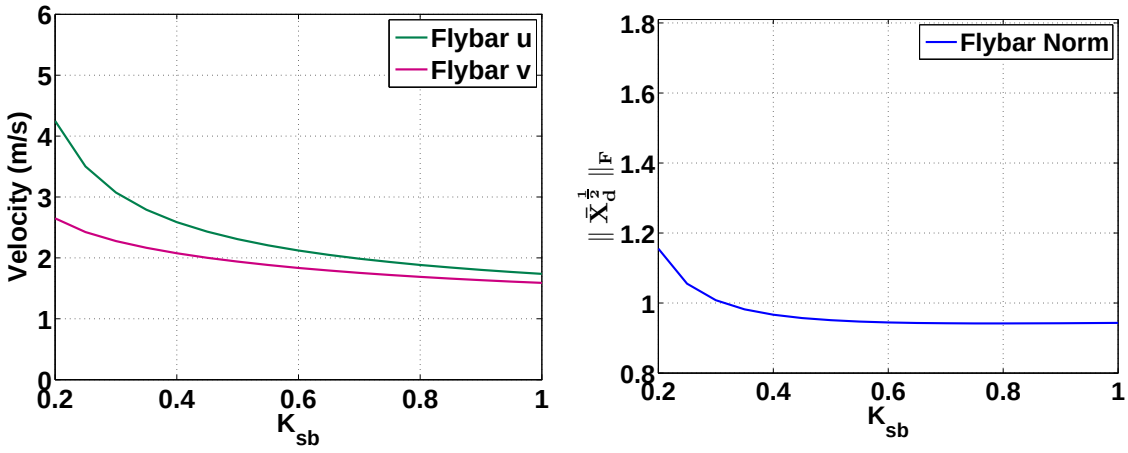

(a) (b)

Figure 5.6: Both a) the disturbance sensitivity of the translational states and b) the Frobenius norm of $X_d^{\frac{1}{2}}$ increase as the inertia (K_{sb}) decreases.

Fig. 5.6 shows a) the dependency of translation states' disturbance sensitivity on the flybar inertia and b) the increase in overall ellipsoid size as a function of the flybar inertia. The analysis confirms that both values increase as the inertia decreases, confirming that the flybar increases disturbance sensitivity in these directions.

The Frobenius norms for the flybarless, flybar, and reduced-inertia flybar helicopters are shown in Table 5.2. The flybarless helicopter has the smallest ellipsoid, showing that the advantage in the p and q directions outweigh the disadvantage

of not having the stabilization device. This advantage may be attributed to the flybarless helicopter's stiffer rotors. The norms do show, however, that the flybar improves the gust tolerance of the vehicle.

5.5 Scaled Disturbance Sensitivity Ellipsoids

At this point in the analysis, the flybarless helicopter shows maneuverability advantage in the u and v directions, while the flybar helicopter shows a gust tolerance advantage in these directions. The platforms have comparable maneuverability in the p and q directions, and the flybarless helicopter shows more gust tolerance in these directions. However, it is still unclear which helicopter has the largest gust rejection capability given the relative sizes and directions of the reachability and disturbance sensitivity ellipsoids. To determine the directions and intensity of gusts that each helicopter can reject with the δ_{lat} and δ_{lon} control inputs, the disturbance sensitivity ellipsoids are scaled to meet the boundary of the reachability ellipsoids. The matrix used to scale the disturbance sensitivity ellipsoid reveals the maximum intensity of a gust in a particular direction. The following section discusses two scaling methods for evaluating the gust rejection capabilities of the helicopters.

The scale of the disturbance input matrix D_g can be adjusted with a similar process to Section 5.2.5. The scaling matrix D_d has on its diagonal the maximum disturbance intensity ρ to be analyzed. The physical interpretation of the scale factor is that the helicopters can tolerate gusts of magnitude ρ (m/s or rad/s) in

any or all directions. The scaled disturbance matrix is

$$D_g = D_d^{-1}\hat{D}_g \tag{5.47}$$

$$D_u = \rho \begin{bmatrix} 1 & 0 & 0 & 0 \\ 0 & 1 & 0 & 0 \\ 0 & 0 & 1 & 0 \\ 0 & 0 & 0 & 1 \end{bmatrix} \tag{5.48}$$

Scaling $\hat{D}_g$ by $\rho > 1$ increases the size of the disturbance sensitivity ellipsoid. While each entry of the diagonal could be scaled differently, the analysis performed in this section assumes the scaling is always uniform, as represented by eqn (5.48).

The reachability and scaled disturbance sensitivity ellipsoids for the flybarless and flybar helicopter are shown in Figs. 5.7 and 5.8. The reachability ellipsoids for each vehicle are the same as those pictured in Fig. 5.1. The disturbance sensitivity ellipsoids assume a gust of unit norm in all directions $\vec{d} = [d_p \ d_q \ d_u \ d_v]^{\mathrm{T}}$ with a disturbance matrix scaled by ρ_0. While ρ_0 may be chosen separately for each entry of the diagonal (scaling the maximum gust for d_u and d_p differently, for instance), it was found that the dynamics of the system were changed approximately evenly for each disturbance. For simplicity, ρ_0 was uniform for each disturbance. For both vehicles, ρ_0 was scaled iteratively until the boundary of $\mathcal{E}_d$ met the boundary of $\mathcal{E}_c$. The scale factor ρ_0 is listed in Table 5.3, along with the scaled Frobenius norm. The flybarless helicopter has a larger ρ_0 and scaled Frobenius norm than the flybar helicopter. In this case, a larger scaled norm shows the platform is capable of rejecting a larger volume of disturbances.

While the flybarless helicopter has a larger disturbance sensitivity ellipsoid, it is interesting to note that the flybar helicopter's control directionality is more effi-

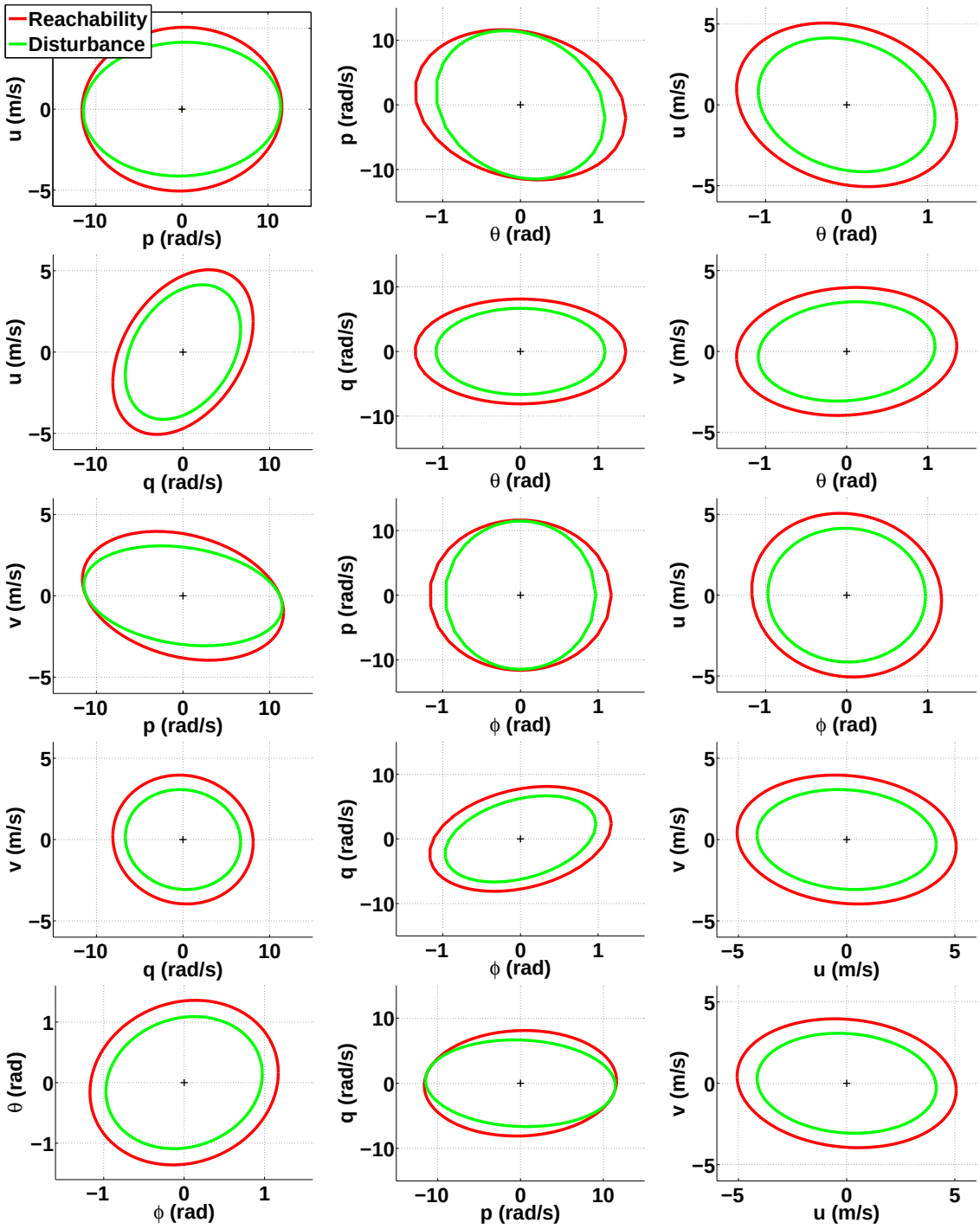

Figure 5.7: The disturbance matrix for the flybarless was scaled by $\rho_0 = 1.7$. The gust tolerance is mostly limited in the p direction.

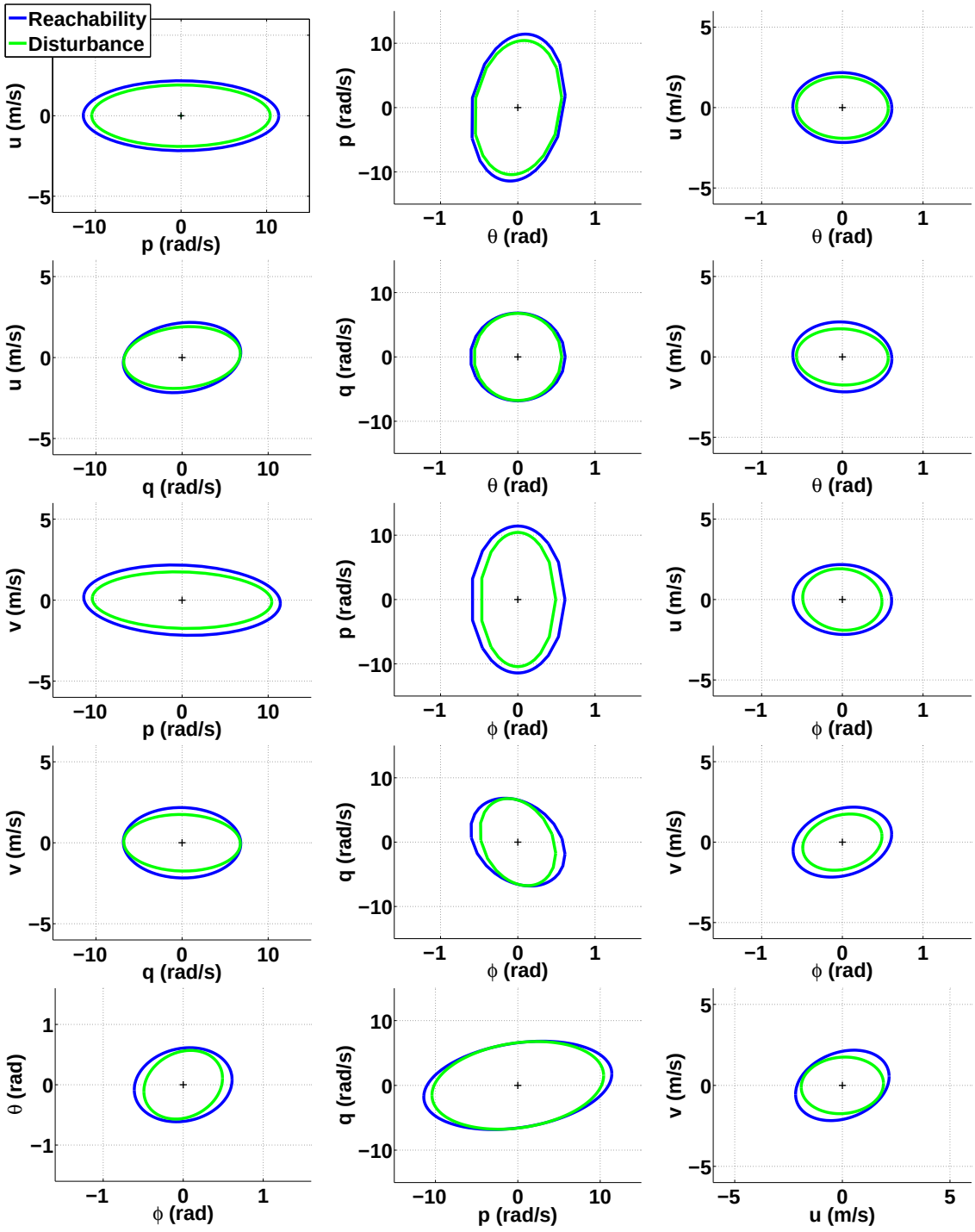

Figure 5.8: The disturbance matrix for the flybar helicopter was scaled by $\rho_0 = 1.1$. The directions of the disturbance sensitivity ellipsoids are well-aligned with the reachability ellipsoids.

	Flybarless	Flybar
ρ_0	1.7	1.1
$\|\rho_0 \bar{X}_d^{\frac{1}{2}}\|_{\mathrm{F}}$	1.46	1.04

Table 5.3: Disturbance Matrix Scale Factor ρ_0

cient. The disturbance Frobenius norm is 92% of the controllability norm; whereas for the flybarless helicopter, the disturbance norm is only 88% of the controllability norm. This can be seen visually from the ellipsoids as well—the directions of the disturbance sensitivity ellipsoids are aligned with the reachability ellipsoids better for the flybar helicopter. The size of the disturbance sensitivity ellipsoids for the flybarless helicopter is limited in the p direction. Scaling the entries of D_d individually may help optimize the size of the disturbance sensitivity ellipsoid for the flybarless helicopter.

To further understand the directional gust tolerance of the vehicle, scale factors ($\rho_p,\ \rho_q,\ \rho_u,\ \rho_v$) for individual directions were considered (i.e., $\vec{d} = [d_p\ 0\ 0\ 0]^{\mathrm{T}}$, $\vec{d} = [0\ d_q\ 0\ 0]^{\mathrm{T}}$, etc.). The resulting scale factors for the two helicopters are provided in Table 5.4 and show that the flybarless helicopter has an advantage in the longitudinal directions especially. Example ellipsoids scaled by ρ_u for $\vec{d} = [0\ 0\ d_u\ 0]^{\mathrm{T}}$ are shown in Figs. 5.10 and 5.9. The figures show the decoupling of the flybar dynamics. A disturbance in the u direction mainly results in a longitudinal response, wheras the flybarless helicopter response has more potential for being longitudinal and lateral.

	ρ_p (rad/s)	ρ_q (rad/s)	ρ_u (m/s)	ρ_v (m/s)
Flybarless	2.9	3.3	4.6	2.5
Flybar	2.0	1.8	1.8	1.9

Table 5.4: Directional Disturbance Scale Factors

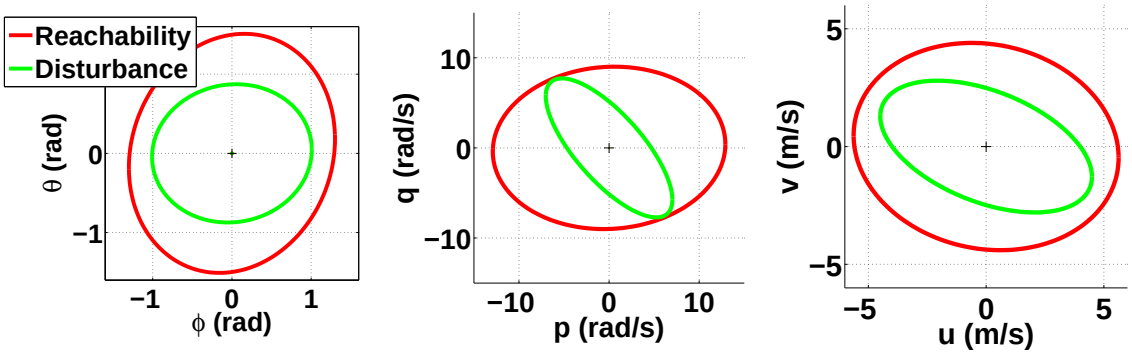

Figure 5.9: Limiting disturbances to the u direction, $\vec{d} = [0\ 0\ d_u\ 0]^{\mathrm{T}}$, shows the control is limited in the p and q directions.

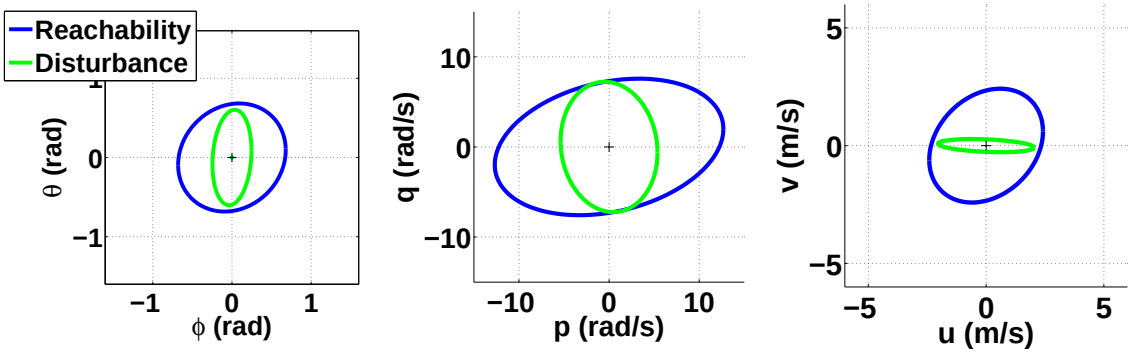

Figure 5.10: The flybar helicopter has less of an off-axis response to a directional disturbance.

5.6 Conclusions

This chapter explored the bare airframe maneuverability and gust tolerance properties of the flybar and flybarless helicopter. A method for determining the

	Flybarless	Flybar
$\|\bar{X}_c^{\frac{1}{2}}\|_{\mathrm{F}}$	1.65	1.14
$\|\bar{X}_d^{\frac{1}{2}}\|_{\mathrm{F}}$	0.86	0.94
ρ_0	1.7	1.1
$\|\rho_0\bar{X}_d^{\frac{1}{2}}\|_{\mathrm{F}}$	1.46	1.04

Table 5.5: Frobenius Norm Summary

controllability gramian for unstable systems was shown and applied to the flybarless helicopter. The eigenstructure of the controllability gramian determines the geometric properties of the reachability ellipsoid for a bounded unit norm input. The disturbance sensitivity ellipsoid can likewise be determined with this method by using the gust matrix D_g as the input matrix. The disturbance sensitivity ellipsoid defines the space to which a vehicle may be perturbed when subjected to a unit norm disturbance. The gust tolerance and maneuverability characteristics of the vehicles can be quantified with these ellipsoids.

By comparing the reachability ellipsoids, it was found that the flybarless helicopter has more reachable states in the u and v directions. The improvement in reachability is shown for the flybar helicopter as the inertia of the flybar is reduced. The flybarless helicopter also shows a gust tolerance advantage, indicated by having smaller disturbance sensitivity ellipsoids than the flybar helicopter. This advantage is likely due to the stiffer rotors. It was shown that the flybar does increase gust tolerance in the u and v directions, as expected, while its effect on the p and q directions is negligible.

A comparison of the disturbance sensitivity ellipsoid scalings of the two vehi-

cles shows that the flybarless helicopter can reject higher intensity gusts than the flybar helicopter, particularly in the longitudinal direction. The flybarless helicopter outperforms the flybar helicopter in terms of both maneuverability and gust tolerance. A summary of the ellipsoid Frobenius norms for the two vehicles is provided in Table 5.5.

Chapter 6

Robust Analysis and Control

6.1 Overview

With identified models for the helicopters, model-based control systems can now be developed that enable the helicopters to perform station-keeping. Without a model, the control designer is limited to the tedious task of guess-and-check gain tuning, or possibly developing an adaptive control law for the system. Having a model enables the designer to use any of the many linear, time-invariant controllers, including a Linear Quadratic Regulator (LQR), a Linear-Quadratic Gaussian (LQG) regulator, or, as discussed here, an $\mathcal{H}_\infty$ controller.

The following chapter gives an overview of $\mathcal{H}_\infty$ control, as well as the static $\mathcal{H}_\infty$ control law used here. Gains for an inner loop stabilizing controller and an outer loop station-keeping controller are selected and the implications of the feedback loops on disturbance rejection and tracking are discussed. Results from an experiment implementing the gains on the helicopters in the lab are then presented.

6.2 Static H-Infinity Model-Based Control

The $\mathcal{H}_\infty$ controller, first introduced by Zames [25], is specifically formulated to provide model robustness in the presence of disturbances. Solutions to the

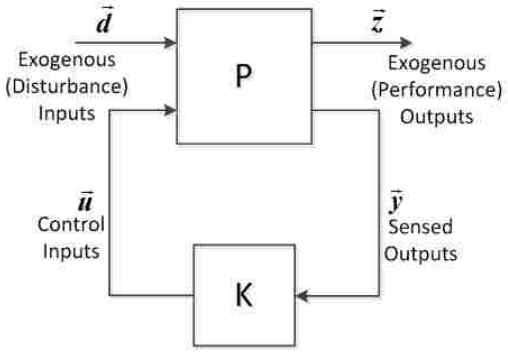

Figure 6.1: $\mathcal{H}_\infty$ Control Block Diagram.

$\mathcal{H}_\infty$ problem were rigorously derived by Doyle, et al [26] for linear, time-invariant systems. A general formulation of the controller is shown in Fig. 6.1, where $\vec{d}$ are exogenous inputs, $\vec{z}$ are the performance outputs, $\vec{u}$ are the inputs, and $\vec{y}$ are the system outputs used for feedback. Exogenous inputs are inputs to the system that the controller cannot directly manipulate—specifically disturbances like gusts. The objective of $\mathcal{H}_\infty$ control is to minimize the infinity norm of the transfer function from the performance output $\vec{z}$ to the disturbance $\vec{d}$. The algorithm is first solved for a stabilizing controller gain bounded by arbitrary γ. The gain γ is iteratively reduced until the algorithm no longer converges. The minimum bound is γ^*.

The $\mathcal{H}_\infty$ controller is a powerful tool, as it allows the control designer to balance trade-offs between noise attenuation, tracking performance, disturbance sensitivity, and control usage. Historically implemented as a dynamic controller, the designer can also weight the frequencies over which the individual objectives are most important. However, a dynamic controller requires significant computational power and is not practically implemented on the GINA mote. As such, a static

$\mathcal{H}_\infty$ controller designed by Gadewadikar is used for this design [27]. In addition to disturbance rejection, this static controller has the additional advantages of a) not requiring full-state feedback (only output feedback) and b) not requiring an initial stabilizing gain.

The model for the static $\mathcal{H}_\infty$ controller is as follows:

$$\dot{\vec{x}} = A\vec{x} + B\vec{u} + D\vec{d} \tag{6.1}$$

$$\vec{y} = C\vec{x} \tag{6.2}$$

$$\|\vec{z}\|^2 = \vec{x}^{\mathrm{T}} Q\vec{x} + \vec{u}^{\mathrm{T}} R\vec{u}, \tag{6.3}$$

where $Q > 0$ and $R > 0$, and the state matrices are scaled as presented in Section 1.2. Also, henceforth D will represent the gust matrix D_g, rather than the feedforward matrix. The Q and R matrices are weights in the cost function,

$$J(K, d) = \int_0^\infty (x^{\mathrm{T}} Q x + u^{\mathrm{T}} R u - \gamma^2 d^{\mathrm{T}} d) dt, \tag{6.4}$$

where K is the feedback gain such that

$$u = -Ky \tag{6.5}$$

$$= -KCx \tag{6.6}$$

The L_2 gain is bounded by γ if

$$\frac{\|\vec{z}(t)\|_2^2}{\|\vec{d}(t)\|_2^2} = \frac{\int_0^\infty \|\vec{z}(t)\|^2 dt}{\int_0^\infty \|\vec{d}(t)\|^2 dt} = \frac{\int_0^\infty (\vec{x}^{\mathrm{T}} Q\vec{x} + \vec{u}^{\mathrm{T}} R\vec{u}) dt}{\int_0^\infty (\vec{d}^{\mathrm{T}} \vec{d}) dt} \leq \gamma^2. \tag{6.7}$$

6.2.1 Solution Algorithm

According to the theorem presented in [28], an $\mathcal{H}_\infty$ gain can be synthesized if the following two necessary and sufficient conditions are met:

1. (A, B) is stabilizable and (A, C) is detectable

2. There exists matrices K and L such that

$$KC = R^{-1}(B^{\mathrm{T}}P + L) \text{ where } P > 0 \text{ is the solution to}$$

$$A^{\mathrm{T}}P + PA^{\mathrm{T}} + Q - PBR^{-1}B^{\mathrm{T}}P + \tfrac{1}{\gamma^2}PDD^{\mathrm{T}}P + L^{\mathrm{T}}R^{-1}L = 0$$

The following iterative algorithm solves the coupled matrix equations central to the static $\mathcal{H}_\infty$ framework:

Step 1: Initialize parameters.

- Select γ bound and Q and R weighting matrices.

- Initialize iteration counter $n = 0$ and parameter matrix L.

Step 2: For each nth iteration,

- Solve Ricatti equation for P_n:

$$P_nA + A^{\mathrm{T}}P_n + Q + \frac{1}{\gamma^2}P_nDD^{\mathrm{T}}P_n - P_nBR^{-1}B^{\mathrm{T}}P_n + L_n^{\mathrm{T}}R^{-1}L_n = 0 \quad (6.8)$$

- Evaluate gain K_{n+1} and update L_{n+1}

$$K_{n+1} = R^{-1}(B^{\mathrm{T}}P_n + L_n)C^{\mathrm{T}}(CC^{\mathrm{T}})^{-1} \quad (6.9)$$

$$L_{n+1} = RK_{n+1}C - B^{\mathrm{T}}P_n \quad (6.10)$$

Step 3: Check convergence,

If $\|K_{n+1} - K_n\| < \epsilon$ for $\epsilon \ll 1$, proceed to Step 4; otherwise update $n = n + 1$ and repeat Step 2.

Step 4: Terminate. Set $K = K_{n+1}$.

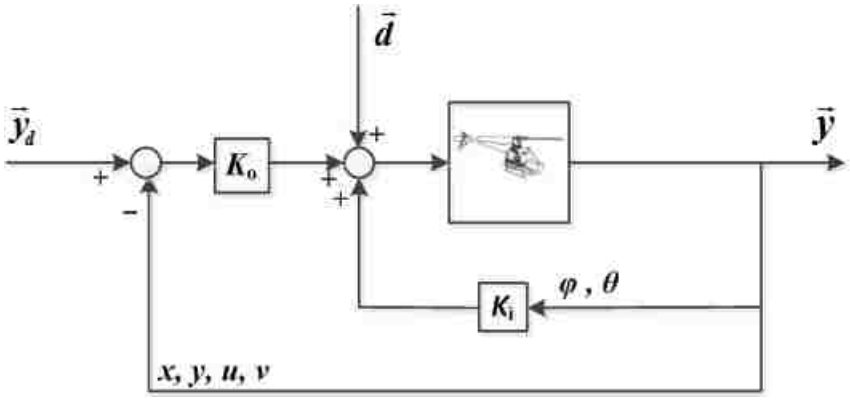

Figure 6.2: $\mathcal{H}_\infty$ The inner loop uses attitude feedback to stabilize the vehicle, and the outer loop uses position feedback to control station keeping.

6.3 Control Structure

The flybarless helicopter is controlled with two loops using a technique called cascaded control, shown in Fig. 6.2. The inner loop is designated for stabilization and typically has a high loop closure rate. On-board sensors like accelerometers and gyroscopes may be used to provide state information for feedback. The outer loop is designated for controlling the vehicle's position and typically operates at a slower rate. The vehicle velocity and position may be measured with either GPS or dead-reckoning based on IMU measurements. All state measurements are provided by Vicon, but the vehicles do have the capability of implementing on-board feedback with the GINA mote.

For the purpose of simulation and to assess the robustness of the model, a wind turbulence model for the gusts is presented. The controllers are first tested and tuned with a Matlab Simulink model, then implemented on the vehicles.

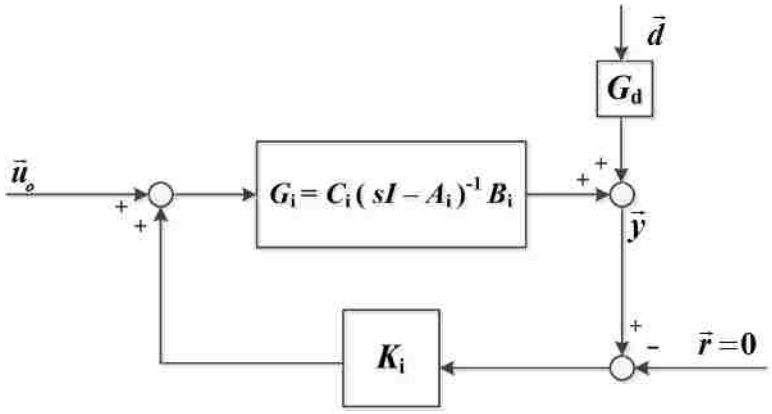

Figure 6.3: The inner loop controller regulates the attitude angles to zero.

6.3.1 Wind Turbulence Model

A Gauss-Markov shaping filter developed by Hall and Bryson [29] for wind disturbances along the $\hat{b}_x$ and $\hat{b}_y$ axes was used to model the gust disturbances for simulation. The disturbance model was also applied to the rotational disturbance directions:

$$\begin{bmatrix} \dot{d}_p \\ \dot{d}_q \\ \dot{d}_u \\ \dot{d}_v \end{bmatrix} = \begin{bmatrix} -1/\tau_c & 0 & 0 & 0 \\ 0 & -1/\tau_c & 0 & 0 \\ 0 & 0 & -1/\tau_c & 0 \\ 0 & 0 & 0 & -1/\tau_c \end{bmatrix} \begin{bmatrix} d_p \\ d_q \\ d_u \\ d_v \end{bmatrix} + \begin{bmatrix} b & 0 & 0 & 0 \\ 0 & b & 0 & 0 \\ 0 & 0 & b & 0 \\ 0 & 0 & 0 & b \end{bmatrix} \begin{bmatrix} q_p \\ q_q \\ q_u \\ q_v \end{bmatrix}. \quad (6.11)$$

The filter parameters were chosen as $\tau = 3.2$ sec and $b = 0.5$ [28].

6.3.2 Inner Loop Stabilization

The primary objective of the inner loop is to stabilize the attitude of the vehicle. The design is posed as a regulator problem, where the inputs $\vec{u}$ require manipulation to counteract the effects of the disturbances $\vec{d}$. A block diagram of the inner loop problem is shown in Fig 6.3. Because the inner loop is regulating the

attitude to zero, the closed loop A matrix takes the form $A_{\mathrm{i,CL}} = A - BK_{\mathrm{i}}C_{\mathrm{i}}$ where K_{i} is the gain selected through the $\mathcal{H}_\infty$ process and C_{i} selects outputs ϕ and θ,

$$C_{\mathrm{i}} = \begin{bmatrix} 1 & 0 & 0 & 0 & 0 & 0 & 0 & 0 \\ 0 & 1 & 0 & 0 & 0 & 0 & 0 & 0 \end{bmatrix}. \tag{6.12}$$

The Q and R matrices were initialized as follows,

$$Q^{-1} = \mathrm{diag}([0.25^2 \;\; 0.25^2 \;\; 6^2 \;\; 6^2 \;\; 0.5^2 \;\; 0.5^2 \;\; 10^2 \;\; 10^2]) \tag{6.13}$$

$$R^{-1} = \mathrm{diag}([0.5^2 \;\; 0.5^2]). \tag{6.14}$$

The resulting K matrix is

$$K_{\mathrm{i}} = \begin{bmatrix} 1.27 & 0.26 \\ -0.16 & 1.14 \end{bmatrix} \tag{6.15}$$

and $\gamma^* = 4.0$.

Three metrics are used to assess the inner loop system dynamics [30, 31]

- **Singular Value Plots** The singular value (SV) plots are constructed from the solution to the singular value decomposition $G = U\Sigma V$ at each frequency and essentially represent the MIMO equivalent of the SISO bode plot. Physically, the singular values represent the maximum response of the system at a given frequency—the response is usually not aligned with a specific channel, but rather represents a combination of the state outputs. To understand the directions, the U and V vectors would need to be examined at each frequency; however, this analysis does not go into that detail. The important thing to note about the SV plots is the frequency range over which the minimum and maximum singular values have a strong response to the inputs, $\underline{\sigma}(G)$, $\overline{\sigma}(G) > -3$dB.

- ***S* and *T* SV Plots** The frequency responses that represent how well the system tracks an input and how well it rejects disturbances are taken from the response equation,

$$y(s) = T(s)r(s) + S(s)d(s). \tag{6.16}$$

The following relationships can be derived from the block diagram,

$$T = GK(I - GK)^{-1} \tag{6.17}$$

$$S = (I + GK)^{-1}, \tag{6.18}$$

where T is the tracking response and S is the disturbance sensitivity response. For ideal reference tracking, $\underline{\sigma}(T) \approx \overline{\sigma}(T) \approx 1$. The bandwidth for measuring how well the system rejects disturbances is defined by $\overline{\sigma}(S) = -3$ dB (from below).

- **Relative Gain Array** The relative gain array (RGA) is a measure of the input-output interactions of a system. It is calculated from the formula,

$$\mathrm{RGA}(G) = G \times (G^{-1})^{\mathrm{T}}, \tag{6.19}$$

where $\times$ denotes element-by-element multiplication. For our purposes, we would ideally like the RGA to be an identity matrix. This would mean that the first input directly effects the first output, the second input directly effects the second output, etc. Any off-diagonal terms indicates coupling between inputs and outputs.

The SV plots presented here are all dependent on the scaling of the system.

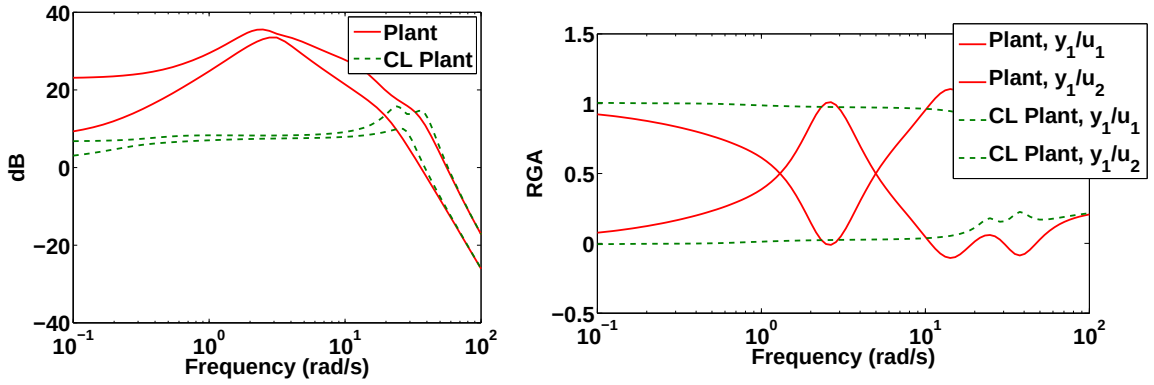

(a) (b)

Figure 6.4: The original plant and closed-loop plant show strong responses (a) up to $\approx$ 40 dB. The RGA plots (b) show how the input-output coupling is improved for the closed-loop system.

The singular value plots for both the original plant and the closed-loop system are shown in Fig. 6.4(a). The inputs to these plants will be the output commands from the outer loop station keeping controller. While the response for the closed loop system is not as strong, sufficient response is still available up to $\approx$ 40 dB. The RGA plots in Fig. 6.4(b) shows that the controller helps decouple the inputs and outputs—that is, a lateral input will more directly affect ϕ and a longitudinal input will more directly affect θ. This is an improvement on the handling of the system.

The tracking and disturbance sensitivity plots are shown in Fig. 6.5. The $\overline{\sigma}(S)$ indicates the closed-loop system has good disturbance rejection up to $\approx$ 18 rad/s. Tracking is best between 1 rad/s and 10 rad/s.

The singular values and RGAs for the flybar helicopter are plotted in Fig. 6.6. The flybar helicopter does not have quite as strong of a response to inputs as the original flybarless plant, and the bandwidth is slightly lower at $\approx$ 30 dB. The RGA

plot indicates that the system inputs and outputs are well-aligned.

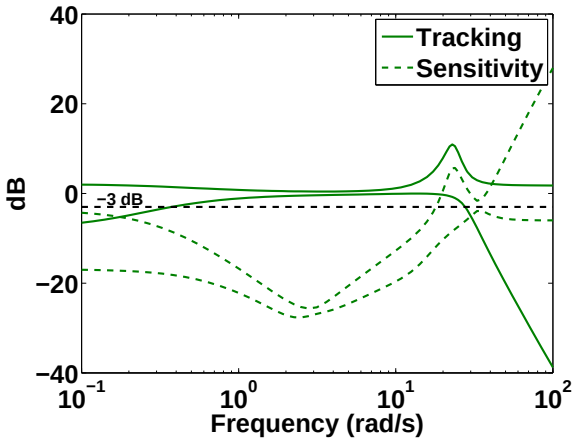

Figure 6.5: The flybarless close-loop system shows good disturbance rejection up to ≈ 18 rad/s. Tracking is best between 1 rad/s and 10 rad/s.

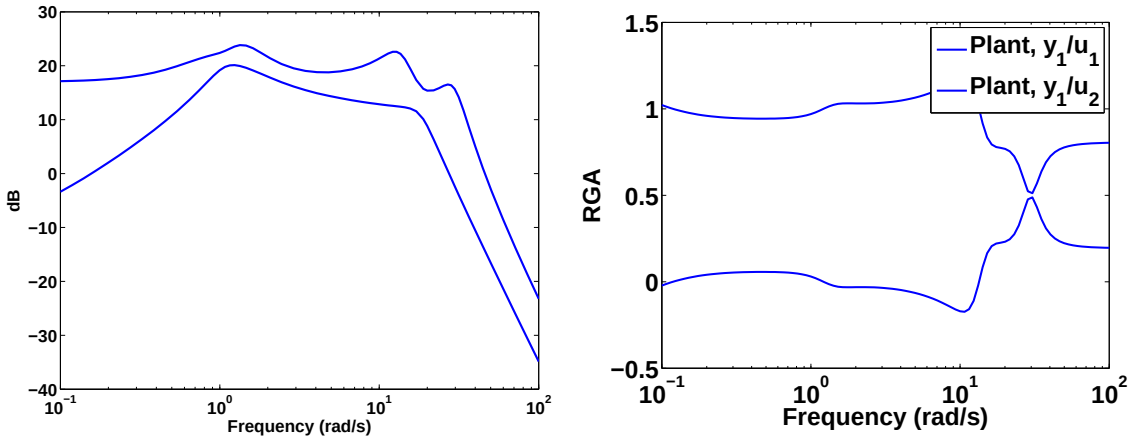

(a) (b)

Figure 6.6: Singular values and RGAs for flybar helicopter.

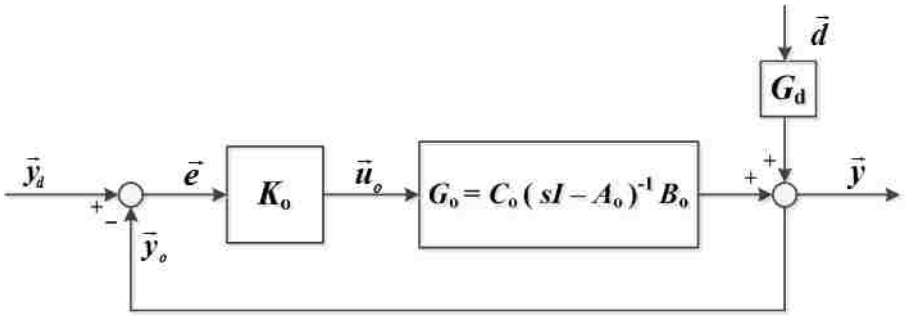

Figure 6.7: The outer loop controls the vehicle to a desired station keeping point.

6.3.3 Outer Loop Station Keeping

The outer loop regulates the error of the desired position in the inertial frame to the actual, $\vec{e} = \vec{y}_o - \vec{y}_d$. The outer loop controller is $\vec{u}_o = K_o\vec{e}$. A block diagram for the outer loop controller is shown in Fig. 6.7.

The outputs for the outer loop controller are $y_o = [x\ y\ u\ v]^{\mathrm{T}}$. Because the helicopter is operating about hover, we can assume $\dot{x} = u$ and $\dot{y} = v$. With this information, the x and y states can be incorporated into the system dynamics. The outer loop A matrix for the flybarless helicopter with states $\vec{x}_{\mathrm{o}} = [\vec{x_{\mathrm{i}}}\ x\ y]^{\mathrm{T}}$ is

$$A_o = \begin{bmatrix} A_{\mathrm{i,cl}} & 0 \\ E & 0 \end{bmatrix} \tag{6.20}$$

where

$$E = \begin{bmatrix} 0 & 0 & 0 & 0 & 0 & 0 & 1 & 0 \\ 0 & 0 & 0 & 0 & 0 & 0 & 0 & 1 \end{bmatrix}. \tag{6.21}$$

The flybar helicopter, without an inner loop, uses the original plant dynamics matrix A and an E matrix with additional zero columns for the c and d states. The B_o

matrices simply have zeros for the additional states,

$$B_o = \begin{bmatrix} B \\ 0 \end{bmatrix}. \tag{6.22}$$

The outer loop observer matrix C_o outputs the u, v, x, and y states,

$$C_o = \begin{bmatrix} 0 & 0 & 0 & 0 & 0 & 0 & 0 & 0 & 1 & 0 \\ 0 & 0 & 0 & 0 & 0 & 0 & 0 & 0 & 0 & 1 \\ 0 & 0 & 0 & 0 & 0 & 0 & 1 & 0 & 0 & 0 \\ 0 & 0 & 0 & 0 & 0 & 0 & 0 & 1 & 0 & 0 \end{bmatrix}, \tag{6.23}$$

for the flybarless helicopter. The flybar helicopter has additional columns of zeros for the c and d states.

For the flybarless helicopter, the following weighting matrices were used:

$$Q^{-1} = \text{diag}([0.35^2 \;\; 0.35^2 \;\; 11^2 \;\; 11^2 \;\; 0.5^2 \;\; 0.5^2 \;\; 2.5^2 \;\; 2.5^2 \;\; 2^2 \;\; 2^2]) \tag{6.24}$$

$$R^{-1} = \text{diag}([0.9^2 \; 0.9^2]). \tag{6.25}$$

The final bounding gain was $\gamma^* = 2$. The resulting close loop gain was

$$K_{\text{o,noFB}} = \begin{bmatrix} -0.08 & 0.47 & -0.14 & 0.40 \\ -0.48 & -0.05 & -0.44 & -0.26 \end{bmatrix}. \tag{6.26}$$

Likewise, the flybar helicopter had initial weight matrices,

$$Q^{-1} = \text{diag}([0.35^2 \;\; 0.35^2 \;\; 11^2 \;\; 11^2 \;\; 0.5^2 \;\; 0.5^2 \;\; 0.5^2 \;\; 0.5v \;\; 3^2 \;\; 3^2 \;\; 2^2 \;\; 2^2]) \tag{6.27}$$

$$R^{-1} = \text{diag}([0.9 \;\; 0.9]), \tag{6.28}$$

with final bounding gain $\gamma^* = 2$ and resulting close loop gain,

$$K_{\text{o,wFB}} = \begin{bmatrix} -0.13 & 0.58 & -0.17 & 0.45 \\ -0.49 & -0.19 & -0.49 & -0.26 \end{bmatrix}. \tag{6.29}$$

The flybar and flybarless outer loop controllers were simulated with Simulink to ensure that the performance is reasonable and that the input limits would not saturate. Both vehicles were subjected to a 1 m/s gust in both the u and v directions.

A plot of the vehicle trajectory and the control inputs are shown for the flybarless helicopter in Fig. 6.8 and for the flybar helicopter in Fig. 6.9. The flybarless helicopter position hold performance is slightly better than the flybar helicopter but requires significantly less overall control energy. This shows the flybarless helicopter can tolerate a higher overall gust intensity with the controller.

The tracking and disturbance sensitivity of the two helicopters are assessed with the SV plots shown in Fig. 6.10. Instead of looking at the S and T transfer functions, which would require taking the pseudo-inverse of the non-square system, approximations about the vehicle performance are made based on the singular values of the open loop transfer function, GK. At low frequencies, the singular values of the sensitivity transfer function can be approximated as $\overline{\sigma}(S) \approx 1/\underline{\sigma}(GK)$. The bandwidth can be approximated as the point where $\underline{\sigma}(GK)$ crosses 1. Also, for

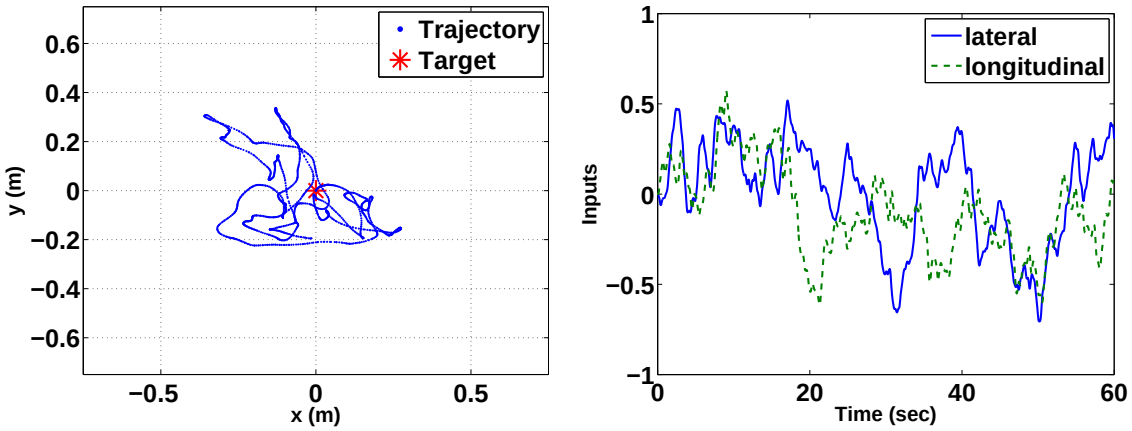

(a) (b)

Figure 6.8: A simulation of the controller shows that the flybarless helicopter has slightly better position hold compared to the flybar helicopter. The overall control energy for the flybarless helicopter is less than for the flybar helicopter. The control limits are not saturated.

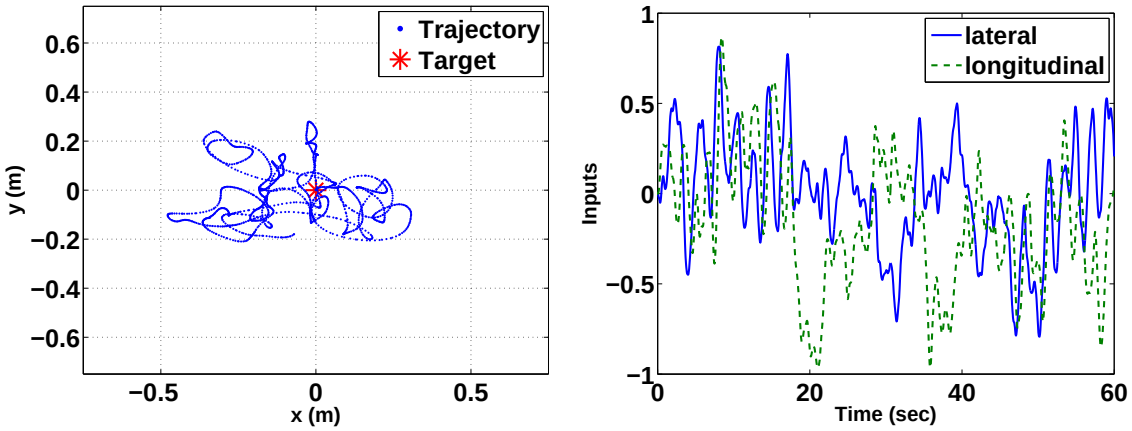

(a) (b)

Figure 6.9: While position hold for the flybar helicopter is comparable, the flybar helicopter requires more control energy and would not tolerate a much higher gust intensity. Control limits are not saturated here.

$GK \gg 1$, we can approximate $T \approx 1$. Therefore, at low frequencies, we require the minimum singular value of GK to be as large as possible to meet this objective. The bandwidth of the system is defined as $\underline{\sigma}(GK) = 1$. The bandwidth of the flybar system is ≈ 16.7 rad/s and of the flybarless system is ≈ 17.2 rad/s, which is relatively similar. The disadvantage of a higher gain, which boosts the bandwidth, is that the system may become more sensitive to sensor feedback noise (which is not an issue with Vicon measurements), model error, or control overuse. This effect could be mitigated if dynamic loop-shaping were applied to the feedback.

6.4 Gust Testing

The controllers for the two systems were tested in the laboratory using a box fan for gust generation, as pictured in Fig. 6.11. The box fan has 3 different gust

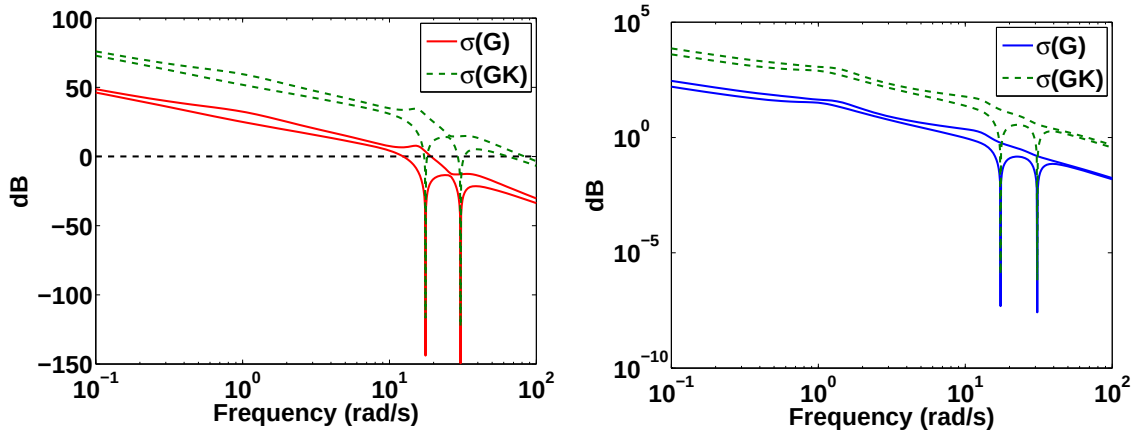

(a) (b)

Figure 6.10: The singular values of the open loop system GK shows good disturbance rejection up to $\approx$ 17 rad/s for the (a) flybarless and (b) flybar systems.

intensity settings (fan held approximately 4 ft from vehicle): 1) $0.5-1$ m/s, 2) $1-1.5$ m/s, and 3) $1.5-2.0$ m/s. Data was collected over a 15 second time interval for gusts in the lateral direction. An example of the vehicle trajectory to a fan setting #1 is shown in Fig. 6.12. The circle drawn is the 50% circle error probable (CEP), a metric used by Costello [1] for measuring vehicle performance in gust. The radius of the circle represents the space in which 50% of the trajectory points lie. A compilation of CEPs for the three fan settings for lateral gusts are shown in Fig. 6.13. The gains used for these tests were slightly modified from those presented above. The outer loop gains used for these tests were

$$K_{o,wFB} = \begin{bmatrix} -0.28 & 0.25 & -0.16 & 0.2 \\ -0.67 & -0.38 & -0.39 & -0.33 \end{bmatrix} \tag{6.30}$$

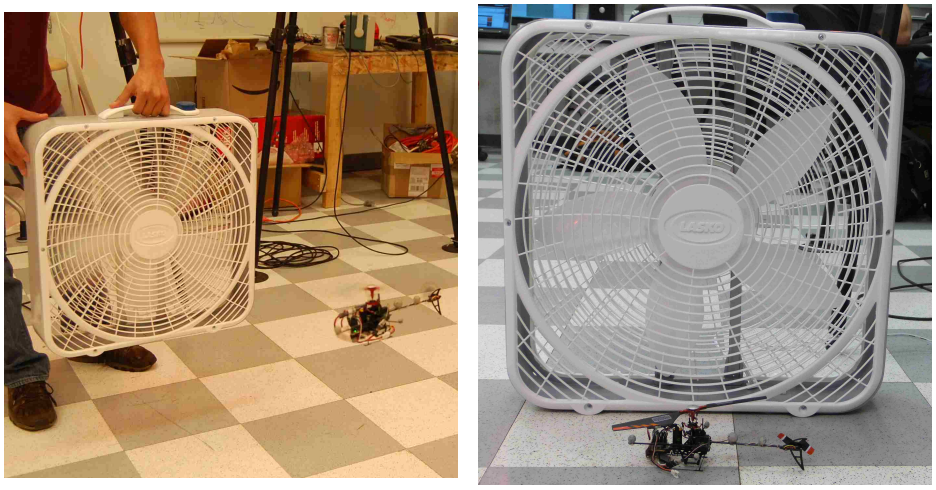

Figure 6.11: The helicopters were tested in the laboratory using a box fan. The gust velocity ranged from 0.5 m/s to 2.0 m/s.

and

$$K_{o,noFB} = \begin{bmatrix} -0.08 & 0.47 & -0.14 & 0.40 \\ -0.48 & -0.05 & -0.44 & -0.26 \end{bmatrix}. \tag{6.31}$$

The inner loop gain for the flybarless helicopter was

$$K_{i,noFB} = \begin{bmatrix} 1 & 0.2 \\ -0.2 & 1 \end{bmatrix}. \tag{6.32}$$

The results in this case show that the flybarless helicopter performs slightly better in the gusts than the flybar helicopter. Due to time constraints, longitudinal tests were not performed. Factors potentially affecting the helicopters' performances included the condition of the servos and speed controllers, which at this point, had been used for many flights.

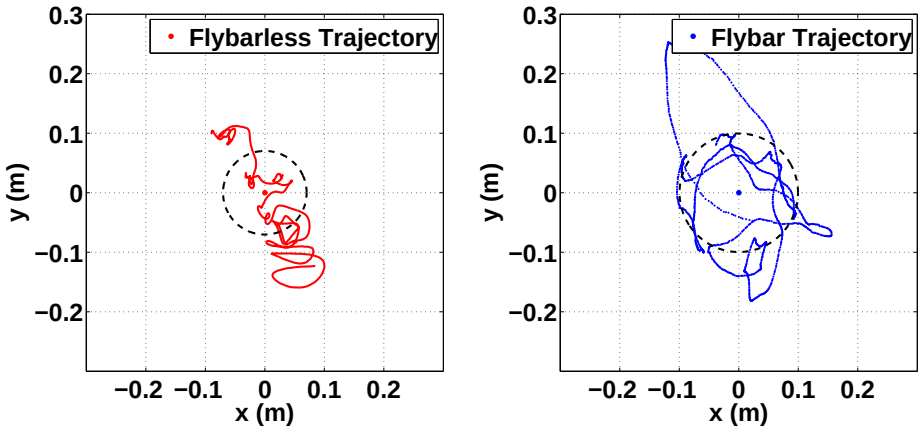

(a) Flybarless, Lateral (b) Flybar, Lateral

Figure 6.12: The 50% CEP represents the a circle encompassing 50% of the points. Here the CEP for the flybarless helicopter is slightly smaller than the flybar's.

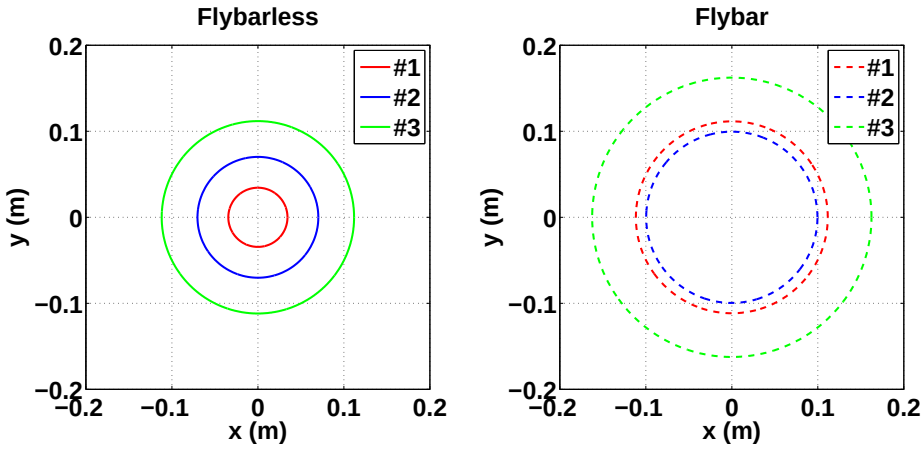

(a) (b)

Figure 6.13: The flybarless helicopter showed better performance when subjected to gust in the lateral direction.

6.5 Conclusions

The overarching objective of this chapter was to develop a model-based control law for the helicopters operating in gusty conditions. The $\mathcal{H}_\infty$ static controller was

chosen for gain selection. The static $\mathcal{H}_\infty$ controller has many advantages over other controller options, the most important being that it takes into account disturbance in its gain selection cost function. The controller was developed in two loops: an inner loop for stabilization and an outer loop for station keeping. The inner loop was only implemented on the flybarless helicopter. It was shown with singular value plots that the inner loop feedback improved the tracking and disturbance rejection of the helicopter, as well as its overall handling. Outer loop gains were then selected for both helicopters. The higher gains improve the disturbance rejection bandwidths of the system, but also subject the model to input saturation, noise feedback, and model error. For these experiments, input saturation was the primary concern. Simulations showed that the gains selected should not saturate the inputs. The controllers were then implemented in the laboratory setting with a box fan for a gust generator. The results showed that the flybarless helicopter performed better than the flybar helicopter.

Nn

Chapter 7

Summary and Future Work

7.1 Research Contributions

The following section explains the significance of each contribution to the field of aerial microsystems system identification, dynamics, and control:

- *A framework for using reachability and disturbance sensitivity sets to assess the bare airframe characteristics of aerial microsystems.* This framework may be used to compare the numerous MAVs currently under development. If linear models can be identified for the vehicles, the sets take the form of ellipsoids, and the performance properties of the bare airframes are easily visualized. Using the generalized gramian, the method can be applied to unstable platforms. This way, the analysis is not subject to any closed loop controllers.

- *A method for performing system identification on a vehicle with highly-coupled dynamics and few known parameters.* Simultaneous, orthogonal, multisinusoidal signals were originally implemented on hypersonic vehicles to quickly and efficiently excite dynamics in a minimal length of time. The application of this input signal to the micro-helicopters was pivotal for exciting both the longitudinal and lateral dynamics in a way that enabled the output error rou-

tine to converge efficiently. For vehicles with highly coupled dynamics, this method should be considered in the future as an alternative to chirp inputs.

- *State space models for a flybar micro-helicopter and a flybarless micro-helicopter.* The state space models developed for both vehicles were used to assess the dynamics and bare airframe characteristics of the vehicles. These models may be used in the future for implementing navigation algorithms and developing an MAV platform with useful functionalities.

- *An assessment of the influence of a Bell flybar on the dynamics, agility, and gust tolerance of a micro-helicopter.* The effects of reducing the inertia of the flybar were assessed progressively throughout the thesis. The research demonstrates that a mechanical stabilization device, while improving the open loop handling for a pilot, may significantly affect the overall potential performance of the vehicle.

- *Static $\mathcal{H}_\infty$ controllers for micro-helicopters designed for station keeping in gusty conditions.* The static $\mathcal{H}_\infty$ controllers were developed and tested in the lab with fan-generated gusts. These controllers may be used in the future in conjunction with navigation sensors to develop on-board station keeping capabilities.

7.2 Summary

The work of this thesis included system identification of micro-helicopters, including model structure development, data collection, and parameter estimation; comparison and analysis of the bare airframe properties, including comparing the natural motions of the vehicles, as well as the bare airframe gust tolerance and maneuverability properties; and developing model-based controllers to stabilize the helicopters for station-keeping in gusty conditions. The key methods and findings are as follows.

7.2.1 System Identification

Developing a model for a vehicle has two major motivations: understanding the physical characteristics of its dynamics and providing a framework for model-based control. For developing the model structure of the flybar and flybarless helicopters, kinematics and rigid-body equations of motion were first considered. Linearized force and moment contributions from control inputs, gravity, and aerodynamics were included as control and stability derivatives. The flapping dynamics of the rotors were then incorporated into the model. A flapping-flybar lumped model proved inadequate, so additional states were also added to model the flybar mechanism for the flybar helicopter. Because of the coupling between the lateral and longitudinal dynamics, exciting both directions simultaneously with orthogonal inputs to both swashplate servos provided the best data for iterating the parameter estimation routine. This was pivotal, as the model was not converging with more traditional

data collection techniques. Because the most common frequency domain parameter estimation techniques do not handle data from two primary inputs, the output error routine from the SIDPAC toolbox was used. The final model parameters for both the flybar and flybarless helicopters had acceptable Cramer-Rao lower bounds and normalized root mean square values.

7.2.2 Bare Airframe Characteristics

Analysis and comparison of the bare airframes was approached first through analysis of the vehicle's modes, and then through the perspective of reachability and disturbance sensitivity ellipsoids. Modal analysis included an examination of the pole locations for each helicopter, as well as the corresponding eigenvector directions. The change in modes was also examined for models where the flybar inertia term is reduced. The findings showed that the flybar decouples the rotational and translational dynamics at low frequencies. The flybar helicopter is a stable system, whereas the flybarless helicopter has a RHP eigenvalue pair.

A method for determining reachability and disturbance sensitivity ellipsoids for unstable systems was presented. This was particularly important for assessing the bare airframe properties of the unstable flybarless helicopter. A comparison of the reachability ellipsoids showed that the flybarless helicopter has an advantage over the flybar helicopter in the translational velocity states u and v. The reachability of the helicopters in the p and q direction were comparable. The results of the disturbance sensitivity ellipsoid analysis likewise showed that the flybarless helicopter had more

gust tolerance, especially with respect to the longitudinal directions.

7.2.3 Robust Analysis and Model-Based Control

Lastly, control laws were designed for the two helicopters and tested in the lab with a box-fan gust. A static $\mathcal{H}_\infty$ controller was selected for gain selection because it is especially suited for implementation on the mote and is designed to reject model disturbances. An inner-loop controller was designed for the flybarless helicopter. An examination of S and T singular values showed that this controller had good gust rejection properties up to ≈ 18 rad/s and good tracking between 1 rad/s and 10 rad/s. The RGA values show that the inner loop controller also helps decouple off-axis inputs and outputs.

An outer loop controller was also developed using static $\mathcal{H}_\infty$ gain selection. The outer loop controller was examined from the perspective of the singular values of the open loop transfer function GK. Both controllers showed good gust rejection and tracking properties up to ≈ 17 rad/s. The models were simulated with a gust input to ensure that actuator limits were not saturated with the control law.

Lastly, the controllers were tested in the lab with gusts ranging from 0.5 to 2 m/s. The results for these tests showed the flybarless helicopter performed better than the flybar helicopter.

7.3 Future Work

The development of robust Micro Air Vehicles capable of navigating and maneuvering through complex environments is an exciting prospect. The applicatons are numerous, ranging from military operations, planetary exploration, or search-and-rescue missions. The future work recommended here uses the current work as a springboard for accomplishing autonomous, robust micro-helicopter designs.

First, a full model of the vehicle needs to be developed, which would include heave and yaw dynamics. These dynamics are also affected by gust disturbances, and the extent of this should be quantified. The recommended vehicle for starting the updated model is the Walkera Genius, which is designed with collective pitch. Compared to the adjustable speed motors on the current helicopters, collective pitch will quicken the response of the heave dynamics. The Genius is also smaller than the current flybarless helicopter, weighing only 35 g. Additionally, a model should be examined for the forward velocity flight condition. This may be more difficult to develop given the space restrictions of the Vicon system. The current model should provide adequate initial conditions, so large data sets may not be required for the data collection maneuvers. A forward flight model would aid in developing algorithms for trajectory tracking.

Next the nagivation and maneuvering capabilities of the vehicle needs to be developed. A starting point for this would be to equip the vehicles with optic flow sensors. The sensors are both small and lightweight enough to fit several on the vehicle. Optic flow has the potential of providing information for station-keeping,

obstacle detection, and state estimation. With the optic flow sensors, the helicopters should easily be capable of navigating a corridor and hovering near an open window or under a ceiling fan.

Last, as more models are developed for MAV platforms, the gust tolerance and maneuverabilty advantages of each vehicle can be compared with a metric based on the ellipsoid analysis. To compliment this study, data should be collected on the frequency content, intensities, and directions of typical building or urban gusts. The vehicles can then be developed for the particular environments for which they are best suited. MAVs that are currently being modeled at the University of Maryland include helicopters, quadrotors, ducted fans, and cyclocopters.

Bibliography

[1] S. Zarovy, M. Costello, A. Mehta, A. Flynn, G. Gremillion, D. Miller, B. Ranganathan, J. Humbert, and P. Samuel, "Experimental study of gust effects on micro air vehicles," in *AIAA Conference on Atmospheric Flight Mechanics, AIAA-2010-7818. American Institute of Aeronautics and Astronautics*, 2010.

[2] I. Faruque, *Control-Oriented Reuced Order Modeling of Dipteran Flapping Flight*. PhD thesis, University of Maryland, College Park, 2011.

[3] D. Szczublewski, "Gust disturbance analysis of a micro quadrotor helicopter," Master's thesis, University of Maryland, College Park, 2012.

[4] K. Zhou, G. Salomon, and E. Wu, "Balanced realization and model reduction for unstable systems," *International Journal of Robust and Nonlinear Control*, vol. 9, no. 3, pp. 183–198, 1999.

[5] J. Molusis, "Helicopter stability derivative extraction from flight data using the bayesian approach to estimation," *Journal of the American Helicopter Society*, vol. 18, no. 2, pp. 12–23, 1973.

[6] G. Padfield and R. Duval, "Applications of system identification methods to the prediction of helicopter stability, control and handling characteristics," Tech. Rep. 82N23230, NASA Ames Research Center, April 1982.

[7] K. Fu and M. Marchand, "Helicopter system identification in the frequency domain," in *9th European Rotorcraft Forum*, 1983.

[8] M. Tischler and M. G. Cauffman, "Frequency-response method for rotorcraft system identification: Flight applications to bo 105 coupled rotor/fuselage dynamics," *Journal of the American Helicopter Society*, vol. 37, no. 3, pp. 3–17, 1992.

[9] B. Mettler, M. Tischler, and T. Kanade, "System identification of small-size unmanned helicopter dynamics," in *Annual Forum Proceedings- American Helicopter Society*, vol. 2, pp. 1706–1717, 1999.

[10] B. Mettler, *Identification Modeling and Characteristics of Miniature Rotorcraft*. McGraw-Hill, 1997.

[11] J. Conroy, J. Humbert, and D. Pines, "System identification of a rotary-wing micro air vehicle," *Journal of the American Helicopter Society*, vol. 56, no. 2, pp. 25001–25001, 2011.

[12] D. Miller, "Open loop system identification of a micro quadrotor helicopter from closed loop data," Master's thesis, University of Maryland, College Park, 2011.

[13] R. Nelson, *Flight stability and automatic control*. McGraw-Hill New York;, 1989.

[14] M. Tischler and R. Remple, *Aircraft and rotorcraft system identification*. 2006.

[15] J. Leishman, *Principles of helicopter aerodynamics*. Cambridge University Press, 2006.

[16] R. Chen, "Effects of primary rotor parameters on flapping dynamics," Tech. Rep. TP-1431, NASA, 1980.

[17] W. Johnson, *Helicopter theory*. Dover publications, 1994.

[18] E. Morelli, "System identification programs for aircraft (sidpac)," in *AIAA Atmospheric Flight Mechanics Conference*, 2002.

[19] V. Klein and E. Morelli, *Aircraft system identification: theory and practice*. American Institute of Aeronautics and Astronautics Reston, VA, USA, 2006.

[20] K. Ogata and Y. Yang, *Modern control engineering*, vol. 4. Prentice Hall Upper Saddle River, NJ, USA, 1990.

[21] C. Chen, *Linear system theory and design*. Oxford University Press, Inc., 1998.

[22] S. Skogestad and I. Postlethwaite, *Multivariable feedback control: analysis and design*, vol. 2. Wiley, 2007.

[23] G. Dullerud and F. Paganini, *A course in robust control theory*, vol. 6. Springer New York, 2000.

[24] K. Zhou, J. Doyle, and K. Glover, *Robust and optimal control*, vol. 40. Prentice Hall Upper Saddle River, NJ, 1996.

[25] G. Zames, "Feedback and optimal sensitivity: Model reference transformations, multiplicative seminorms, and approximate inverses," *Automatic Control, IEEE Transactions on*, vol. 26, no. 2, pp. 301–320, 1981.

[26] J. Doyle, K. Glover, P. Khargonekar, and B. Francis, "State solutions to standard h_2 and h_∞ control problems," *Automatic Control, IEEE Transactions on*, vol. 34, no. 8, pp. 831–847, 1989.

[27] J. Gadewadikar, F. L. Lewis, L. Xie, V. Kucera, and M. Abu-Khalaf, "Parameterization of all stabilizing static state-feedback gains: Application to output-feedback design," *Automatica*, vol. 43, no. 9, pp. 1597 – 1604, 2007.

[28] J. Gadewadikar, *H_∞ Output-Feedback Control: Application to Unmanned Aerial Vehicle*. PhD thesis, University of Texas, Arlington, 2007.

[29] W. Hall Jr and A. Bryson Jr, "Inclusion of rotor dynamics in controller design for helicopters," *Journal of Aircraft*, vol. 10, no. 4, 2012.

[30] M. Morari, "Design of resilient processing plantsiii: A general framework for the assessment of dynamic resilience," *Chemical Engineering Science*, vol. 38, no. 11, pp. 1881–1891, 1983.

[31] S. Skogestad and E. Wolff, "Controllability measures for disturbance rejection," *Modeling Identification and Control*, vol. 17, no. 3, pp. 167–182, 1996.